

PROCESSING CELLULOSE NANOCRYSTAL SUSPENSIONS FOR ALIGNED  
DEPOSITION

A THESIS SUBMITTED TO  
THE GRADUATE SCHOOL OF NATURAL AND APPLIED SCIENCES  
OF  
MIDDLE EAST TECHNICAL UNIVERSITY

BY

CEREN KOCAMAN

IN PARTIAL FULFILLMENT OF THE REQUIREMENTS  
FOR  
THE DEGREE OF MASTER OF SCIENCE  
IN  
CHEMICAL ENGINEERING

APRIL 2022



Approval of the thesis:

**PROCESSING CELLULOSE NANOCRYSTAL SUSPENSIONS FOR  
ALIGNED DEPOSITION**

submitted by **CEREN KOCAMAN** in partial fulfillment of the requirements for the degree of **Master of Science in Chemical Engineering Department, Middle East Technical University** by,

Prof. Dr. Halil Kalıpçılar  
Dean, Graduate School of **Natural and Applied Sciences**

\_\_\_\_\_

Prof. Dr. Pınar Çalık  
Head of Department, **Chemical Engineering**

\_\_\_\_\_

Assoc. Prof. Dr. Emre Büküşođlu  
Supervisor, **Chemical Engineering, METU**

\_\_\_\_\_

Assoc. Prof. Dr. Zeynep Çulfaz Emecen  
Co-supervisor, **Chemical Engineering, METU**

\_\_\_\_\_

**Examining Committee Members:**

Prof. Dr. Levent Yılmaz  
Chemical Engineering, METU

\_\_\_\_\_

Assoc. Prof. Dr. Emre Büküşođlu  
Chemical Engineering, METU

\_\_\_\_\_

Assoc. Prof. Dr. Zeynep Çulfaz Emecen  
Chemical Engineering, METU

\_\_\_\_\_

Prof. Dr. Yusuf Uludađ  
Chemical Engineering, METU

\_\_\_\_\_

Prof. Dr. Nihal Aydođan  
Chemical Engineering, Hacettepe University

\_\_\_\_\_

Date: 26.04.2022

**I hereby declare that all information in this document has been obtained and presented in accordance with academic rules and ethical conduct. I also declare that, as required by these rules and conduct, I have fully cited and referenced all material and results that are not original to this work.**

Name, Surname: Ceren Kocaman

Signature :

## ABSTRACT

### PROCESSING CELLULOSE NANOCRYSTAL SUSPENSIONS FOR ALIGNED DEPOSITION

Kocaman, Ceren

M.S., Department of Chemical Engineering

Supervisor: Assoc. Prof. Dr. Emre Büküşoğlu

Co-Supervisor: Assoc. Prof. Dr. Zeynep Çulfaz Emecen

April 2022, 83 pages

Precise control over membrane performance by tuning fabrication parameters is highly desirable. We developed ultrafiltration membranes by depositing cellulose nanocrystals (CNCs) of 180 nm length and 8 nm diameter on porous support via tangential flow filtration, then irreversibly coagulated the deposited layer permeating highly concentrated  $\text{AlCl}_3$  solution. At a high enough shear rate on the support surface, CNCs aligned in the flow direction, showing a nematic order. The shear rates for transition to the nematic phase determined from rheology analysis, polarized optical microscopy, and membrane performance were consistent with one another, at ca.  $10 \text{ s}^{-1}$ . Permeating an  $\text{AlCl}_3$  solution through the shear-aligned CNC deposit stabilized the CNC layer by screening repulsive electrostatic interactions, and the stable CNC layer was obtained. On changing the surface shear rate from 10 to  $50 \text{ s}^{-1}$ , the order parameter of CNCs increased from 0.17 to 0.7, and the rejection for Blue Dextran (5 kDa) increased from 82 to 92.7% and that for  $\beta$ -lactoglobulin (18 kDa) increased from 89.6 to 93.7%. By varying electrostatic interactions between nanocrystals during deposition, membrane performance was also tuned via changing ionic strength and pH

of CNC suspensions. Increasing NaCl concentration of CNC suspensions from 0 to 25 mM increased Blue Dextran (5 kDa) rejection from 92.7% to 97% at high tangential flowrate and from 82% to 97% at low tangential flowrate. For membranes fabricated at high tangential flowrate,  $\beta$ -lactoglobulin (18 kDa) rejections increased from 93.7% to 98% when NaCl concentration increased from 0 to 25 mM. Increasing pH of CNC suspensions also increased probe molecule rejections, implying a smaller overall interparticle distance between CNCs in the deposited layer. CNC membranes' pure water permeances were comparable to commercial membranes of similar separation properties. Polarized optical microscopy analyses showed that the alignment of CNCs and their aggregates, or tactoids, affect CNC deposits' morphology. In all cases, CNC membrane structures and performances were tuned by easy-to-apply parameters. Hence, a simple and scalable method for controlling the rejection properties of ultrafiltration membranes is developed, which uses aqueous CNC suspensions to form the selective layer.

**Keywords:** cellulose nanocrystals, ultrafiltration, tangential flow filtration, shear alignment, electrostatic interactions, controlled deposition

## ÖZ

### SELÜLOZ NANOKRİSTAL SÜSPANSİYONLARININ HİZALI BİRİKTİRME YÖNTEMİYLE İŞLENMESİ

Kocaman, Ceren

Yüksek Lisans, Kimya Mühendisliği Bölümü

Tez Yöneticisi: Doç. Dr. Emre Büküşoğlu

Ortak Tez Yöneticisi: Doç. Dr. Zeynep Çulfaz Emecen

Nisan 2022 , 83 sayfa

Üretim parametrelerini ayarlayarak membran performansı üzerinde hassas kontrol oldukça arzu edilir. 180 nm uzunluğunda ve 8 nm çapında selüloz nanokristalleri (CNC'ler) teğetsel akış filtrasyonu yoluyla gözenekli destek üzerinde biriktirerek ve ardından bireken tabakaya yüksek konsantrasyonlu  $AlCl_3$  çözeltisi nüfuz ettirerek tabakayı geri döndürülemez şekilde pıhtılaştırarak ultrafiltrasyon membranları geliştirdik. Yeterince yüksek bir kesme hızında destek yüzeyinde CNC'ler akış yönünde hizalanarak nematik bir düzen gösterir. Nematik faza geçiş için kesme hızı, reoloji analizi, polarize optik mikroskopisi ve membran performansı birbirleriyle tutarlıydı yaklaşık olarak  $10\text{ s}^{-1}$  idi. Bir  $AlCl_3$  çözeltisinin kesme hizalı CNC tortusu içinden geçmesi, itici elektrostatik etkileşimleri tarayarak CNC katmanını stabilize etti ve kararlı CNC katmanı elde edildi. Yüzey kesme hızı  $10$ 'dan  $50\text{ s}^{-1}$ 'a değiştirildiğinde, CNC'lerin sıra parametresi  $0,17$ 'den  $0,7$ 'ye yükseldi ve Mavi Dekstran (5 kDa) için reddetme  $\%82$ 'den  $\%92,7$ 'ye yükseldi ve  $\beta$ -laktoglobulin (18 kDa)  $\%89,6$ 'dan  $\%93,7$ 'ye yükseldi. Biriktirme sırasında nanokristaller arasındaki elektrostatik etki-

leşimleri deęiştirerek, CNC süspansiyonlarının iyonik gücü ve pH'ı deęiştirilerek, membran performansı ayarlandı. CNC süspansiyonlarının NaCl konsantrasyonunun 0'dan 25 mM'ye artırılması, Mavi Dekstran (5 kDa) reddini yüksek teęetsel akıř hızında %92,7'den %97'ye ve düşük teęetsel akıř hızında %82'den %97'ye yükseltti. Yüksek teęetsel akıř hızında üretilen membranlar için, NaCl konsantrasyonu 0'dan 25 mM'ye yükseldiğinde  $\beta$ -laktoglobulin (18 kDa) reddi %93,7'den %98'e yükseldi. CNC süspansiyonlarının artan pH'ı ayrıca, biriken katmandaki CNC'ler arasında daha küçük bir genel parçacıklar arası mesafe anlamına gelen prob moleköl reddini de arttırdı. CNC membranlarının saf su geçirgenlikleri, benzer ayırma özelliklerine sahip ticari membranlarla karşılaştırılabilir ölçekteydi. Polarize optik mikroskop analizleri, CNC'lerin ve bunların kümelerinin veya taktoidlerinin hizalanmasının CNC tortularının morfolojisini etkilediğini gösterdi. Her durumda, CNC membran yapıları ve performansları, uygulaması kolay parametrelerle ayarlandı. Sonuç olarak, seçici tabakayı oluşturmak için sulu CNC süspansiyonlarını kullanan, ultrafiltrasyon membranlarının reddetme özelliklerini kontrol etmek için basit ve ölçeklenebilir bir yöntem geliştirilmiştir.

Anahtar Kelimeler: selüloz nanokristal, ultrafiltrasyon, teęetsel akıř filtrasyonu, kesme hizalaması, elektrostatik etkileşimler, kontrollü biriktirme



To my family and dearest Cem, people who have made me who I am today

## ACKNOWLEDGMENTS

Firstly, I would like to express my deepest gratitude to my supervisor, Assoc. Prof. Dr. Emre Büküşođlu for his guidance, advice, and encouragement for this study. I am grateful to him for giving me the opportunity to work in his lab while I was an undergraduate and for introducing me to the exciting world of scientific research. I would also like to express my most profound appreciation to my co-supervisor, Assoc. Prof. Dr. Zeynep ulfaz Emecen for her endless patience, constant support, and guidance throughout this study. She has been an excellent role model for me.

I would like to thank all the Soft and Functional Materials Laboratory members; Özge Batır, Elif Kurt, Aslı Karausta, Elif Erelik, Pınar Beyazkılı Ayas, Ali Akman, Umut Din, Burak Akdeniz, Deniz Işınsu Avşar and Selin Şengöl for their help, support, and giving me another good reason to come work every day; their pure friendship. I would also thank Berk Can İten, Ecem Deveci, Fatma Seden Tekin, Onur Kaan Aydın, and the other members of Membranes for Energy and Water Laboratory, and Öznur Dođan for their help and partnership during this study.

I also would like to thank my friends, Melis Özdemir, Dođa Tekbaş, Deniz Cansel Gürsul, Ceren Dođan, Yađmur Demirci, and Ođuz Süyün, for reminding me to take breaks and have fun when I needed the most.

Last but not least, I would like to thank my parents, Muzaffer Kocaman and Bengöl Kocaman, for their unconditional love, understanding, and unwavering support in every aspect of my life. Thank you, for making me the luckiest in the world. I also would like to thank Begüm Cömert, the best sister in the world, and my brother Kaan Cömert, for bringing the brightest light of my life to the world; Pera Cömert.

And, I would like to thank Cem Bilalođlu, for being the best playmate I can imagine, always encouraging me for the best, and giving me a reason to smile every day.

## TABLE OF CONTENTS

ABSTRACT . . . . .	v
ÖZ . . . . .	vii
ACKNOWLEDGMENTS . . . . .	x
TABLE OF CONTENTS . . . . .	xi
LIST OF TABLES . . . . .	xiv
LIST OF FIGURES . . . . .	xv
CHAPTERS	
1 INTRODUCTION . . . . .	1
2 LITERATURE REVIEW . . . . .	11
3 EXPERIMENTAL PROCEDURES . . . . .	19
3.1 Materials . . . . .	19
3.2 Preparation of Cellulose Nanocrystal (CNC) Suspensions . . . . .	19
3.3 Cellulose Nanocrystal Suspension Characterization . . . . .	20
3.3.1 Rheological Analysis of CNC Suspensions . . . . .	20
3.3.2 Stability Analysis of CNC Suspensions . . . . .	20
3.3.3 Capillary Flow of CNCs . . . . .	21
3.3.4 CNC Suspension Flow Simulations . . . . .	21
3.4 Cellulose Nanocrystal Membrane Fabrication . . . . .	21

3.4.1	Fabrication of Support Layer . . . . .	21
3.4.2	Fabrication of Cellulose Nanocrystal Deposit Layer . . . . .	22
3.4.3	AlCl <sub>3</sub> Treatment of Cellulose Nanocrystal Deposit Layer . . . . .	23
3.4.4	Membrane Separation Tests . . . . .	24
3.5	Optical Characterizations . . . . .	25
3.5.1	Polarized Optical Microscopy . . . . .	25
3.5.2	Atomic Force Microscopy . . . . .	25
3.5.3	Scanning Electron Microscopy . . . . .	25
4	RESULTS AND DISCUSSIONS . . . . .	27
4.1	Shear Aligned Cellulose Nanocrystal Membranes . . . . .	27
4.1.1	Cellulose Nanocrystals . . . . .	27
4.1.2	Rheology of Cellulose Nanocrystals . . . . .	28
4.1.3	Flow Characteristics of Cellulose Nanocrystal Suspensions . . . . .	29
4.1.4	Shear-Aligned Deposition of CNCs . . . . .	33
4.1.4.1	CNC Deposition on Support Layers . . . . .	33
4.1.4.2	Shear Alignment of the Deposited CNC Layer . . . . .	39
4.1.4.3	Separation Performance of Shear Aligned Membranes . . . . .	44
4.1.5	CNC Membranes with Tuned Electrostatic Interactions . . . . .	46
4.1.5.1	Cellulose Nanocrystals in Presence of Salts . . . . .	46
4.1.5.2	Electrostatic Interactions Effects on CNC Membranes . . . . .	50
4.1.5.3	Structural Characteristics of CNC Deposit Layers . . . . .	57
5	CONCLUSIONS . . . . .	65
	REFERENCES . . . . .	67

A MICHEL-LEVY COLOR CHART . . . . .	77
B MEMBRANES AFTER FILTRATION TESTS AGAINST CHARGED MOLECULES	79
C ANALYTICAL MODELLING OF CAPILLARY FLOW OF CELLULOSE NANOCRYSTAL SUSPENSIONS . . . . .	81

## LIST OF TABLES

### TABLES

Table 3.1 CNC Membranes . . . . .	24
Table 4.1 Pure Water Permeances (PWP) of CNC Membranes and Commercial Ultrafiltration Membranes and with Varying Molecular Weight Cut-off (MWCO) . . . . .	53

## LIST OF FIGURES

### FIGURES

- Figure 1.1 Hierarchical structure of cellulose nanocrystal from macro-scale to nano-scale (A), representation of strong hydrolysis of cellulose to for synthesis of cellulose nanocrystals (B) [3] . . . . . 2
- Figure 1.2 Schematic of the self-assembly of a CNC suspension upon evaporation to form a structurally colored film. Phase diagram showing the transition from isotropic to cholesteric phase (blue dots) upon increasing CNC concentration and the corresponding equilibrium pitch (red diamonds). b) Atomic force microscopy image of individual cellulose nanocrystals. c) Polarized optical microscopy image of a typical fingerprint pattern of the cholesteric phase. a–c) [8] . . . . . 3
- Figure 1.3 Representation of light interaction of rod-like liquid crystal replaced in between crossed polarizers . . . . . 4
- Figure 1.4 Schematic description of CNC suspensions from rest to increasing applied shear rates, displaying transitions from isotropically distributed "cholesteric tactoids" at rest, to aligned "cholesteric tactoids" in regime I, to fragmentation of micrometer size tactoids in regime II, to isolated oriented CNCs in regime III. Blue circles or blue ellipses drawn in the scheme identify the cholesteric phase domains or tactoids with respect to the isotropic phase. [14] . . . . . 5
- Figure 1.5 Pressure-driven membrane processes for water treatment technologies, showing the particles effectively captured by each process along with the pore sizes of the membranes used for each process [21] . 7

Figure 1.6 Schematic representation of (a) dead-end filtration and (b) cross-flow filtration [22] . . . . . 8

Figure 1.7 The effect of pressure on ultrafiltration membrane flux and the formation of a secondary gel layer. Ultrafiltration membranes are best operated at pressures below  $P_2$  when the gel layer has not formed. Operation at high pressures such as those above  $P_3$  leads to formation of thick gel layers, which consolidate over time, resulting in permanent fouling of the membrane[20] . . . . . 10

Figure 2.1 (a) Formation of polyelectrolyte multilayer nanofiltration membrane. Membrane pore structure is determined by the polyelectrolyte and salt concentrations of the deposition solution due to interactions between the polyelectrolyte and salt.[33] (b) Fabrication of ultrathin cellulose nanoporous membranes by nanofibers. Illustration of the membrane fabrication process: (i) the very dilute cellulose solution was frozen to form cellulose-NMMO solids, (ii) the frozen solids were extracted in water to produce the cellulose nanofibers, and (iii) the cellulose nanofibers were used to form an ultrathin nanoporous membrane by direct filtration.[35] (c) Sketch of the membrane formation by nanoparticle assembly: during the course of the solvent evaporation, the increase of the block copolymer concentration triggers their self-assembly into micelles, which assemble in three dimensions forming a dynamic interactive membrane film. [37] (d) A schematic representation of 2D nanosheets used for graphene oxide membranes (GOM).  $K^+$  ions in a GOM determine and fix the interlayer spacing such that other cations are rejected while pure water can penetrate. Yellow pillars between the graphene oxide sheets depict the fixation of interlayer spacing by hydrated  $K^+$ .[43] . . . . . 12



Figure 2.2	Schematic of CNC film processing and the configuration of the test samples extracted from the as cast films for (a) unsheared and (b) shear casting. The directionality of the shear cast films was defined as “axial” or “transverse” for the direction parallel to or perpendicular to the shear direction.[59]	14
Figure 2.3	Schematic illustration of CNC film formation from CNC suspensions as water evaporates. A lyotropic phase transition occurs as the CNC concentration reaches $C^*$ upon drying. Tactoids nucleate and grow over time to yield larger anisotropic domains. (b) POM image of a CNC film revealing optical birefringence due to the locked-in cholesteric mesophase (the pitch is visible in the 2x enlargement of the identified region). (c) Cross-sectional cryofractured SEM image displaying a layered morphology. (d) POM images of mesomorphic films cast from aqueous suspensions containing 3 wt% CNC and 4 different salts (labeled on left) at 4 different concentrations (labeled on top). The scale bar applies to all images.[17]	15
Figure 2.4	Schematic representation of the vacuum-assisted CNC self-assembly process [67]	16
Figure 3.1	Cellulose nanocrystal suspension synthesis by sulfuric acid hydrolysis of cotton linters	20
Figure 3.2	Support layer fabrication by phase inversion steps	22
Figure 3.3	Tangential flow filtration system used for fabrication of cellulose nanocrystal membranes	23
Figure 4.1	Atomic force microscopy 2D height image of CNCs. Scale bar: 250 nm	28
Figure 4.2	Steady shear viscosity of 6.4% (w/v) (blue), 3.2% (w/v) (orange), 2% (w/v) (gray), and 1.5% (w/v) (yellow) aqueous CNC dispersions as a function of shear rate.	29

Figure 4.3	Polarized optical microscopy images of cellulose nanocrystal suspension flow in a capillary tube at different concentrations: (a) 1.5% (w/v) (inset: bright field image of the 1.5% (w/v) CNC suspension flow; inset image scale bar is 100 $\mu$ m), (b) 2% (w/v) (inset: high-exposure image of CNC at a flow rate of 2000 $\mu$ Lh <sup>-1</sup> ), (c) 3.2% (w/v) (inset: high-exposure image of CNC at a flow rate of 1000 $\mu$ Lh <sup>-1</sup> ), and (d) 6.4% (w/v) (rows); flow rates and wall shear rates (columns). Scale bar is 250 $\mu$ m. . . . .	31
Figure 4.4	(a) Intensity profile plots with varying flow rates of CNC suspensions with a concentration of 3.2% (w/v) along the diameter of the capillary tube. Simulated shear stress profile of 2% (w/v) dispersion at flow rate 2000 $\mu$ Lh <sup>-1</sup> (b) and 3.2% (w/v) dispersion at flow rate 1000 $\mu$ Lh <sup>-1</sup> (c) along the capillary tube with the cross-section view. . . . .	33
Figure 4.5	Cellulose nanocrystal suspension tangential flow filtration onto porous support layer . . . . .	34
Figure 4.6	(a) Permeate flux as a function of transmembrane pressure (TMP) for various feed flow rates during the filtration of CNCs (0.3 % (w/v)) on Supports I and II (after determining the limiting flux on Support I, only two TMP values with fluxes both at the limiting value were applied for CNC membrane preparation by CNC deposition on Support II) (b) Estimation of gel concentration from experimental data based on gel-polarization model . . . . .	35
Figure 4.7	(a) Cellulose nanocrystal suspension with concentration of 0 mM (left) and 200 mM (right) AlCl <sub>3</sub> (b) Fabricated CNC80 membrane after deposition of CNCs via 0.2 mM AlCl <sub>3</sub> salt filtration on Support II (c) CNC80 placed in DMSO solution before (a) and after (b) the Support II dissolved in DMSO . . . . .	36

Figure 4.8 (a) CNC deposit resistance (left axis) after CNC filtration on Support II and after salt permeation for CNC membranes fabricated under different flow rates, calculated by Darcy's law and resistances in series. Specific resistances of each membrane, calculated by deposit resistances of each membranes divided by CNC layer thickness (right axis) (b) Scanning electron microscopy images of cross section of membranes (CNC200, CNC80, CNC30 and CNC9). Measured thicknesses for CNC200, CNC80, CNC30 and CNC9 are  $14.3\pm 0.9$ ,  $21.6\pm 2.5$ ,  $31.5\pm 2.3$ ,  $36.2\pm 1.4$   $\mu\text{m}$  Scale bars: 50  $\mu\text{m}$  (first row), 25  $\mu\text{m}$  (second row), 10  $\mu\text{m}$  (third row). . . . . 38

Figure 4.9 Brightfield (BF) and polarized light (PL) optical images of empty Support I (a) and Support II (b). Single white arrow represents the membrane position with respect to analyzer. Crossed white arrows show the direction of analyzer and polarizer. Scale bars: 250  $\mu\text{m}$  . . . . 39

Figure 4.10 (a) Polarized light images of the middle part of CNC-deposited membranes with a flow rate of  $80 \text{ mLmin}^{-1}$  and feed concentration of 0.3% (w/v). Single white arrows represent the feed flow direction. Crossed arrows show the direction of the analyzer and polarizer. Scale bar is 250  $\mu\text{m}$  (insets: first-order retardation plate images; additive red arrow to crossed-polarizers represents the direction of the first-order retardation plate; and the inset scale bar is 100  $\mu\text{m}$ ). (b) Mean gray values of polarized light images with respect to the angle of deposition of the CNC membrane in (a) to the analyzer angle. . . . . 40

Figure 4.11 Simulated shear rate profile of CNC suspension flow at the surface of the tangential flow filtration module with the feed flow rate of  $80 \text{ mLmin}^{-1}$ . . . . . 41

Figure 4.12 (a) Polarized light images of CNC-deposited membranes on Support I placed with feed flow in the same direction with the polarizer (first column) and rotated 45° clockwise to the analyzer (second column) with a feed concentration of 0.3% (w/v). Single white arrows represent the feed flow direction. Crossed arrows show the direction of the analyzer and polarizer. Feed flow rates and generated mean shear rate values in the central region of the modules during the CNC filtration: (a) 80 mLmin<sup>-1</sup>, 40 s<sup>-1</sup>; (b) 60 mLmin<sup>-1</sup>, 30 s<sup>-1</sup>; (c) 40 mLmin<sup>-1</sup>, 20 s<sup>-1</sup>; and (d) 20 mLmin<sup>-1</sup>, 10 s<sup>-1</sup>. Inset sketches (a) and (d) represents the nematic and cholesteric order of the membranes. Scale bar is 250 μm. (e) Scanning electron microscopy images of cross sections of CNC9 and CNC80 membranes (f) Mean gray profile along the SEM cross-section view of CNC9 membrane . . . . . 42

Figure 4.13 AFM top-view phase images of CNC-deposited membranes (a) CNC200, (b) CNC80, (c) CNC30, and (d) CNC9. Red arrow indicates the direction of feed flow during filtration. Scale bar is 250 nm. Bottom panel shows the polar histograms for each membrane for the % aligned nanocrystals where the reference axis is the CNC flow direction. . . . . 43

Figure 4.14 Percent rejection values of the empty support membrane (Support II) and membranes fabricated at CNC suspension feed flow rates of 9 mLmin<sup>-1</sup> (CNC9), 30 mLmin<sup>-1</sup> (CNC30), and 80 mLmin<sup>-1</sup> (CNC80) against different probes with varying molecular weights. . . . . 46

Figure 4.15 Change in distance between cellulose nanocrystal with the increase of salt concentration in the suspension . . . . . 47

Figure 4.16 (a) CNC suspension (0.3 % (w/v)) turbidity for varying salt concentrations and salt valence, (b) photographs of CNC suspensions with pH=3 upon salt addition with varying ion valance (c) CNC suspensions with pH values of 3 and 7, with 50 mM NaCl, 200 mM NaCl, 200 mM CaCl<sub>2</sub>, 5 mM AlCl<sub>3</sub>, 20 mM AlCl<sub>3</sub> and 50 mM AlCl<sub>3</sub> (photographs were taken after 1 day of sample preparation). Small blue arrows indicate the level of CNC aggregation phase within suspension. . . . . 47

Figure 4.17	Internal potential energies of cellulose nanocrystals at different salt concentrations in parallel (a) and cross (b) orientation . . . . .	49
Figure 4.18	Polarized light optical images of CNC80 membranes with 5 mM AlCl <sub>3</sub> (a) and 25 mM CaCl <sub>2</sub> (b) concentration. Insets show POM Double-sided yellow arrows indicate the direction of flow during deposition. Scale bars: 250 μm for POM images. . . . .	50
Figure 4.19	CNCs limiting fluxes with varying NaCl concentration in the CNC feed and feed pH . . . . .	51
Figure 4.20	(a) CNC9 and CN80 membrane percent rejection values and pure water permeances with varying NaCl concentration in the CNC feed and at neutral pH (b) CNC80 and CNC80-25 percent rejection values against probe molecules of Vitamin B12 and β-lactoglobulin . . . .	52
Figure 4.21	CNC deposit layer resistances before and after AlCl <sub>3</sub> treatment and specific resistances of each membrane for membranes at varying NaCl concentrations (a and b) and different pH (c) . . . . .	56
Figure 4.22	POM images of (a) CNC9 (d) CNC80 membranes with different NaCl concentrations at suspension pH value of 3. Insets show POM images of CNC deposits without a support layer obtained by dissolving the support in acetone. Red arrows in CNC9-25 and CNC80-25 show tactoids. Double-sided yellow arrows indicate the direction of flow during deposition. Illustrations below the polarized images represent CNC assembly in the corresponding CNC deposit layer (b,e). Scale bars: 250 μm μm for POM, 50 μm for inset images. The bottom panel shows the scanning electron micrographs of each membrane for the same column (c,f). Blue arrows indicate the cross-section of CNC deposit layers. . . .	59
Figure 4.23	Polarized light optical images of CNC9-50 and CNC80-50 membranes. Double-sided yellow arrows indicate the direction of flow during deposition. Scale bars: 250 μm for POM images. The bottom panel shows the scanning electron images of each membrane for the same column. Blue arrows indicate the cross-section of CNC deposit layers. .	60

Figure 4.24	Scanning electron microscopy images of cross-section of CNC9-pH7 and CNC80-pH7 membranes. Double sided arrows indicate CNC layer deposit on support. . . . .	61
Figure 4.25	(a) Polarized light optical images of CNC9-pH7 and CNC80-pH7 membranes and mean gray value profile of these membranes with respect to angle of deposition direction relative to analyzer direction based on POM images. Double sided blue arrows in POM images represents the deposition direction. Crossed-white arrows represent the direction of analyzer and polarizer. Scale bars: 250 $\mu\text{m}$ for POM images (b) Atomic force microscopy image of top view of CNC9-pH7 membrane and angle frequency plot of the angles of nanocrystals based on AFM images. Angles represent the local direction relative to flow direction. Scale bar: 250 nm for AFM image (c) First-order-retardation plate images of CNC9-pH7 membranes at 0 and 90° of deposition direction relative to polarizer. Same colored circles show the same regions at two orientations. Additional orange double sided arrow represents the direction of retardation plate. Scale bars: 250 $\mu\text{m}$ . . . . .	63
Figure A.1	Michel-Levy color chart . . . . .	77
Figure B.1	Photographs of CNC80 membranes after rejection tests against (a) Rose Bengal (973 Da, negatively charged) (b) Crystal Violet (408 Da, positively charged) . . . . .	79
Figure C.1	Representation of control volume in a capillary tube . . . . .	81

## CHAPTER 1

### INTRODUCTION

Cellulose nanocrystals (CNCs) are biodegradable nanomaterials derived from the natural polymer cellulose. They have attracted considerable attention in engineering applications due to their biocompatibility, renewability, availability, and intrinsic properties, including high elastic modulus, high specific strength, high surface area, and optical transparency.[1, 2] CNCs are rod-like nanostructures whose length and diameter vary based on the cellulose source and extraction method of the nanocrystals. The common cellulose sources used in cellulose nanocrystal synthesis are plants (wood pulp and cotton linter), algae (red, green, and yellow algae), bacteria, and tunicates.[1]

There are different mechanical (high-pressure homogenization, ultrasonic treatments, cryo crushing, micro fluidization techniques) and chemical (enzymatic reactions, strong acid hydrolysis) treatments for extraction of cellulose microfibrils. Cellulose microfibrils consist of long fiber networks with amorphous and crystalline regions. The individual fibers with nanoscale diameters, called cellulose nanofibers, are produced with suitable chemical treatments. [1] For the production of cellulose nanocrystals from cellulose microfibrils, chemical methods, especially strong acid hydrolysis, are mostly preferred due to the low consumption of energy and enhanced crystallinity of resultant cellulose nanocrystals. As schematically shown in Figure 1.1, in strong acid hydrolysis, strong acid agents penetrates disordered (amorphous) regions of cellulose and hydrolyze these parts; repeated highly ordered crystalline structures with higher resistance to acids are remained unaffected by this process. [1] Several strong acids, such as hydrochloric, phosphoric, and hydrobromic acids, have been used in literature for the synthesis of cellulose nanocrystals. The type of strong acid used in synthesis directly affects the suspension stability. [1] Thus, sulfuric acid hydrolysis is the most

common one to synthesize CNCs since resultant CNCs possess negatively charged sulfate groups on the nanocrystal surface.[2, 1]Electrostatic repulsion resulting from these negatively charged groups promotes uniform dispersions of cellulose nanocrystals that show good colloidal stability with isotropic behavior in an aqueous medium at dilute concentrations.[2]

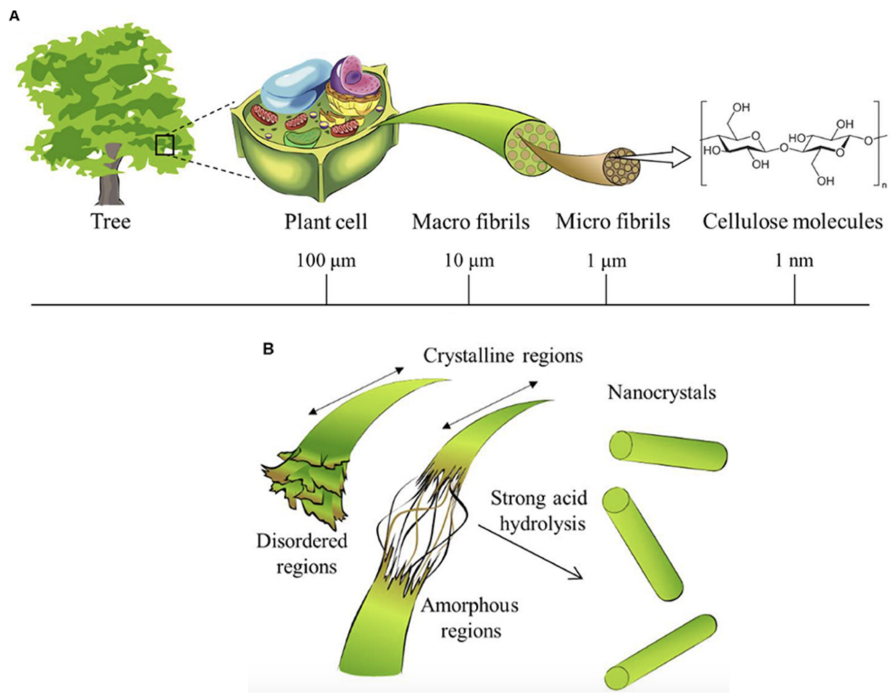


Figure 1.1: Hierarchical structure of cellulose nanocrystal from macro-scale to nano-scale (A), representation of strong hydrolysis of cellulose to for synthesis of cellulose nanocrystals (B) [3]

Liquid crystals (LCs) are condensed fluid phases between crystalline solids and isotropic fluids. There are two main classes of liquid crystals; LCs with temperature affected phase behavior (thermotropics) and LCs with concentration affected phase behavior (lyotropics), which require solvent to form LCs.[4] The dispersions of rod-like particles exhibit lyotropic liquid crystalline phases above a critical concentration because of the balance between rotational and translational entropy.[5, 6] The aspect ratio, size polydispersity, and particle-solvent interactions of nanorods affect lyotropic liquid crystalline phase formation dynamics.[7] CNCs possess rigidity, a suitable aspect ratio, and anisotropy to exhibit lyotropic liquid crystal phase behavior. Above



a certain concentration, their aqueous suspensions self-assemble into chiral nematic, or cholesteric structures.[8, 9] As shown in Figure 1.2, aqueous suspensions of cellulose nanocrystals obtained by sulfuric acid hydrolysis form isotropic suspensions where nanocrystals are randomly distributed in the suspension as a result of electrostatic repulsion between negatively charged sulfate groups at low CNC concentrations. Removal of the water results in ordered CNC configurations to minimize the repulsive interactions between nanocrystals; thus, at higher CNC concentrations, anisotropy is observed.[2] In the intermediate CNC concentration region, both phase (isotropic and anisotropic (liquid crystalline)) coexists and this phase region called as "biphasic".[2, 8] (Figure 1.2). As also shown in Figure 1.2, at higher concentrations cellulose nanocrystals self-assembled into cholesteric arrangements with a cholesteric pitch,  $p$ . [8]

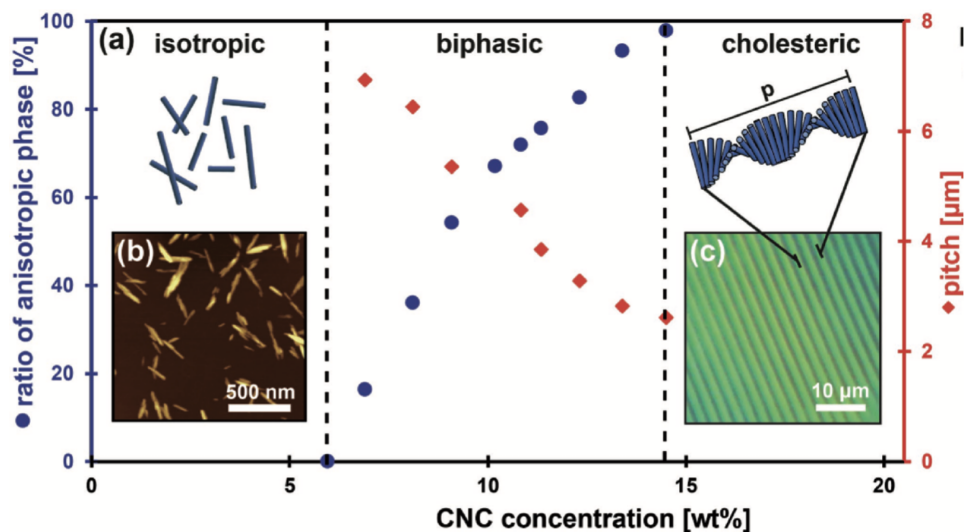


Figure 1.2: Schematic of the self-assembly of a CNC suspension upon evaporation to form a structurally colored film. Phase diagram showing the transition from isotropic to cholesteric phase (blue dots) upon increasing CNC concentration and the corresponding equilibrium pitch (red diamonds). b) Atomic force microscopy image of individual cellulose nanocrystals. c) Polarized optical microscopy image of a typical fingerprint pattern of the cholesteric phase. a-c) [8]

The critical concentration  $C^*$  for the cellulose nanocrystal suspension phase change from isotropic-to-biphasic can be predicted based on the Onsager Model, which describes the liquid crystalline phase formation of nanorod suspensions such as carbon nanotubes, boehmite, fd virus, and cellulose nanocrystals. [10, 5, 6] Based on this model, the aspect ratio of CNCs ( $L/d$ ) is inversely proportional to  $C^*$ . [11]

$$C^* = \frac{\pi \cdot \rho \cdot d^2}{4 \cdot L^2} \tag{1.1}$$

$\rho$  in the Equation 1.1 is the density of cellulose nanocrystals, which is  $1.53 \text{ gcm}^{-3}$ . [12] Based on this model, longer and thinner nanorods result in a decrease of the critical concentration for isotropic to anisotropic phase change, and a higher aspect ratio of cellulose nanocrystals results in enhancement of anisotropy of the CNC samples.

The ordered configuration of cellulose nanocrystals allows the suspension to acquire birefringence, which makes anisotropic cellulose nanocrystal suspensions visible through crossed polarizers. [8] The representation of birefringence of rod-like liquid crystal is shown in Figure 1.3. As can be seen in the figure, when the cellulose nanocrystal is placed in the same direction as one of the analyzers, no light appears. However, when the CNC is rotated to some degree, light passes through polarizers due to the birefringence of the CNC.

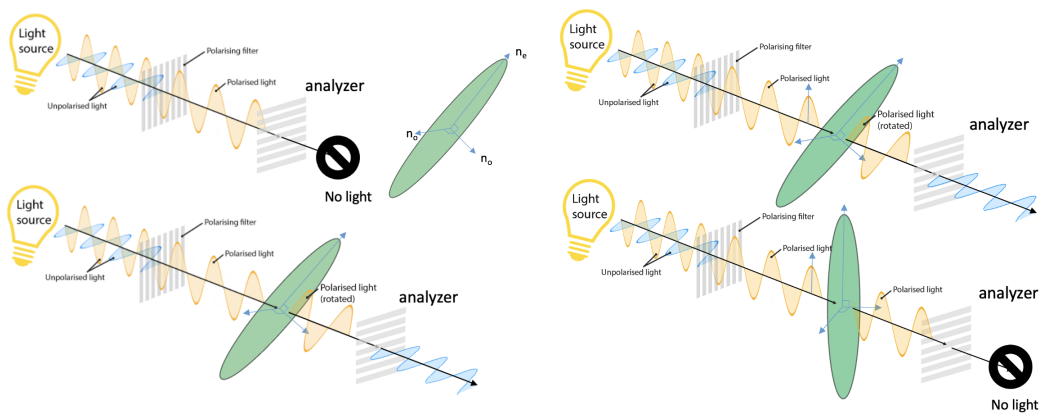


Figure 1.3: Representation of light interaction of rod-like liquid crystal replaced in between crossed polarizers

In addition to the change in phase behavior that occurs above the critical concentration, the rheological behavior of CNCs also changes.[9] For isotropic suspensions, the viscosity of the suspension is almost independent of the shear rate. In contrast, for suspensions in the liquid crystalline phase, the shear viscosity is dependent on the shear rate. The measurements of steady shear viscosity with respect to shear rate usually show a constant viscosity plateau for isotropic suspensions, while for anisotropic suspensions, a three-region behavior appears, a shear-thinning region at low shear rates, followed by a plateau region and a final shear-thinning region.[13] The rheological behavior of cellulose nanocrystals with applied shear is shown in Figure 1.4.

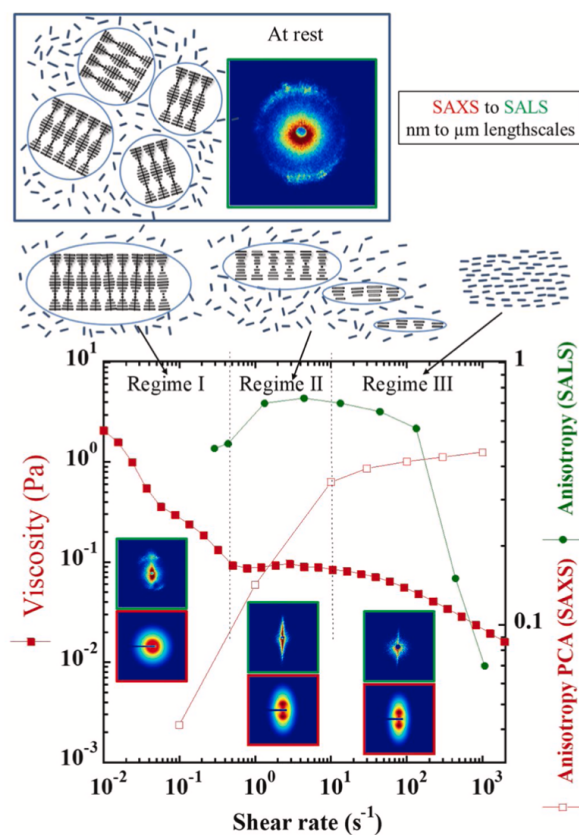


Figure 1.4: Schematic description of CNC suspensions from rest to increasing applied shear rates, displaying transitions from isotropically distributed "cholesteric tactoids" at rest, to aligned "cholesteric tactoids" in regime I, to fragmentation of micrometer size tactoids in regime II, to isolated oriented CNCs in regime III. Blue circles or blue ellipses drawn in the scheme identify the cholesteric phase domains or tactoids with respect to the isotropic phase. [14]

As shown in Figure 1.4, Region I (shear thinning at low shear rates) and Region II (intermediate shear rates) were generally associated with shear-dependent variations of the polydomain structures and their textures. Shear-thinning at higher shear rates, Region III, is observed where the nanocrystals are mostly oriented in the direction of flow, in the form of larger domains.[15, 16] The change in the structure resulting from alignment generates shear-thinning behavior.[12] Thus, applied shear on cellulose nanocrystals results in a change in the degree of alignment of CNCs, which will be discussed further in Section 2 as well as the difference in the rheological behavior of the suspension.

The presence of electrolytes affects electrostatic interactions between nanocrystals. The addition of electrolytes results in compression of the electrical double layer, so attractive forces become dominant between nanocrystals. The transition from stable suspension to aggregated state is directly affected by the ionic strength of the CNC suspension. The Schulze-Hardy rule explains the effect of ion valence on such systems' critical aggregation concentration (CAC). Based on this rule, CAC is inversely proportional to the ion valence of added electrolytes.[17, 18, 19] In this study, the aggregation behavior of cellulose nanocrystals in the presence of salt is used for two primary purposes; to form stable CNC deposits layer by irreversible coagulation of CNC in the presence of concentrated multivalent salt and to tune the distance between nanocrystals by adding salts to the CNC suspensions, which will be further explained in Section 2.

Herein, we aimed to control the assembly of CNCs by two approaches; first, controlling the degree of alignment of CNC by varying shear applied on CNCs; second, tuning electrostatic interactions between nanocrystals by adding inorganic salts to the CNC suspensions in varying proportions. In both cases, CNCs were deposited on porous support layers via tangential flow filtration of their dilute suspensions and irreversibly coagulated on the support layer to be further used as ultrafiltration membranes for the separation of macromolecules.

The membrane separation process principle is based on a presence of a semipermeable filter, where the mixture to be separated forced through the membrane with a driven force and separated based on size or charge. With the advantages such as low energy consumption and easy-to-scale-up systems, they are essential separation technologies for macromolecules.[20] Pressure-driven membranes are classified based on pore sizes; microfiltration, ultrafiltration, nanofiltration, and reverse osmosis membranes concerning decreased pore sizes(Figure1.5). Ultrafiltration (UF) membranes are used for a variety of macromolecules such as suspended particles, proteins, and polysaccharides.[20]

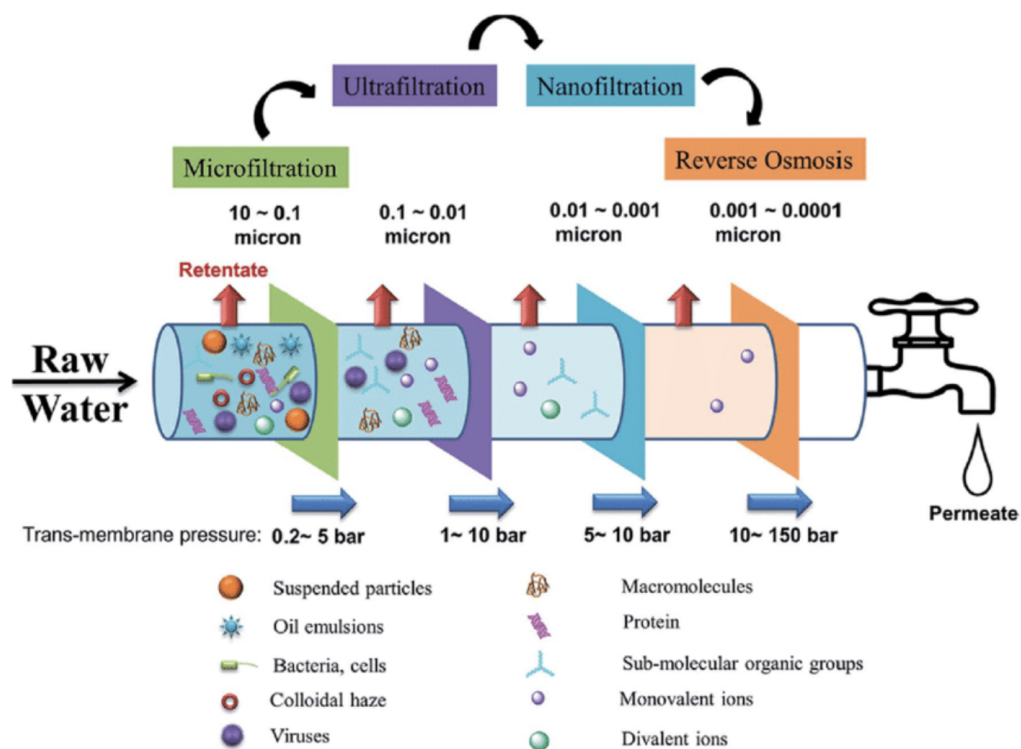


Figure 1.5: Pressure-driven membrane processes for water treatment technologies, showing the particles effectively captured by each process along with the pore sizes of the membranes used for each process [21]

Membrane separation processes can be performed in two ways; dead-end filtration and tangential flow (or crossflow) filtration (Figure1.6). Dead-end filtration is a batch process where a pressure difference forces the mixture; small molecules and solvent pass through the semipermeable membrane's pores while larger molecules are

rejected and accumulated on the membrane surface. Crossflow filtration feed mixture moves tangentially on the membrane surface while the transmembrane pressure (TMP) is applied perpendicularly to the tangential flow through the membrane.

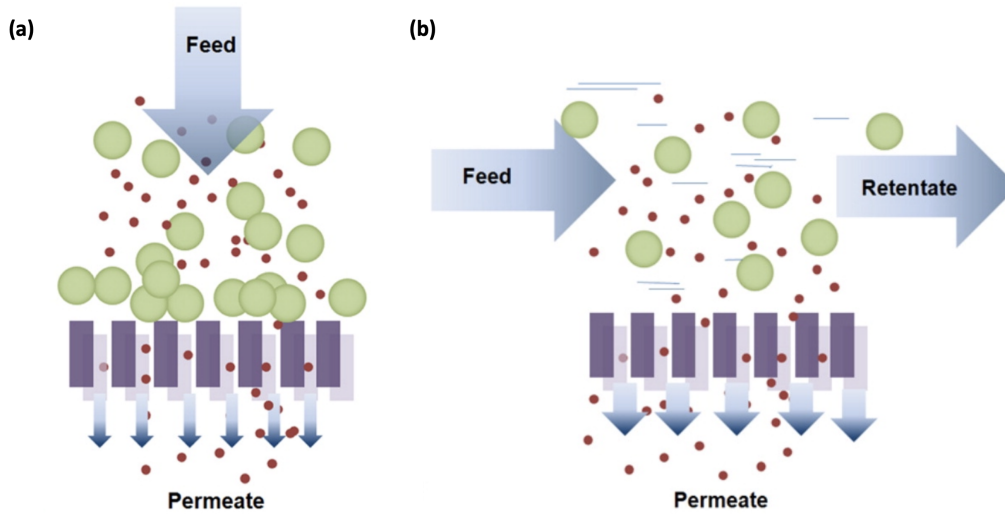


Figure 1.6: Schematic representation of (a) dead-end filtration and (b) crossflow filtration [22]

During tangential flow filtration through a porous layer, species rejected by the porous surface are enriched near the wall when the permeate drag toward the wall is larger than the back-diffusion of rejected species. Permeate drag is enhanced by the permeate flux through the porous layer, while the tangential flow velocity enhances back-diffusion. When the concentration at the wall reaches the maximum attainable value, due to the closest packing of particles or the solubility limit, a cake or gel layer starts to deposit on the surface. As shown in Figure 1.7, this phenomenon is clearly observed when the pressure difference across the porous layer is gradually increased while filtering a component that is rejected by the pores at a certain tangential flow velocity. The permeate flux through the porous layer is observed to increase linearly until the rate of increase with rising TMP drops, and finally, the permeate flux levels off at the "limiting flux". This point marks the maximum attainable concentration on the surface, which results in the deposition of rejected species on the surface if the filtration is continued. Further increasing the pressure only increases the thickness of this deposit on the surface while the permeate flux remains unchanged at the limiting value. [20, 23]

For 100% rejection of the filtered species, a species material balance in the mass-transfer boundary layer near the surface then yields the following relationship; [20]

$$\frac{C_{\text{gel}}}{C_{\text{bulk}}} = \exp\left(\frac{J\delta}{D_{ij}}\right) = \exp\left(\frac{J}{k_c}\right) \quad (1.2)$$

where  $C_{\text{gel}}$  is the maximum attainable concentration of the rejected species,  $C_{\text{bulk}}$  is the bulk concentration of this species,  $J$  is the permeate flux,  $\delta$  is the mass-transfer boundary layer thickness,  $D_{ij}$  is the diffusion coefficient of the rejected species in the solution, and  $k_c$  is the convective mass-transfer coefficient, which is equal to the ratio of  $D_{ij}$  to  $\delta$ , according to the film theory of mass transfer. The phenomenon of limiting flux and cake/gel deposition is typically observed during membrane filtration and is regarded as a form of membrane fouling, where the porous layer described above is a separation membrane, and the deposited species are those that are aimed to be rejected by the membrane.

The most common polymeric ultrafiltration membrane fabrication method is phase separation (NIPS), which relies on the phase separation of a polymer solution upon coming in contact with a non-solvent, as a result of which the polymer-rich phase forms the membrane matrix, and the polymer-lean phase forms the pores.[20] In this method, membrane permeance and selectivity can be varied with process parameters such as choice of solvent, non-solvent, and polymer solution composition, the relationship between these parameters and resulting membrane properties is not straightforward. It is highly desirable to design and control resulting membrane properties with membrane formation parameters. [24] Considering the complete life cycle of membrane modules, the use of natural and biodegradable materials such as cellulose and its derivatives is also very attractive.

Thus, intending to develop a novel method to fabricate membranes with controllable structure by using non-toxic membrane material, we used the phenomenon of limiting flux and cake/gel formation to deposit a CNC layer, which will act as the selective membrane layer itself, onto a support surface, which is a looser, larger-pore membrane. The shear-induced alignment of the CNC at the support surface due to the applied shear was used to adjust the CNC deposit's morphology and tune the CNC membranes' performance. In addition to shear-alignment tuning electrostatic inter-

actions by adding monovalent electrolytes to CNC suspensions and change in pH of the CNC suspensions offered a novel way to tune the structure and performance of CNC membranes. The method further provides the advantage of using an aqueous nanomaterial suspension derived from the natural polymer cellulose to prepare the selective membrane layer instead of synthetic polymers and harmful organic solvents typically used in ultrafiltration membrane fabrication.

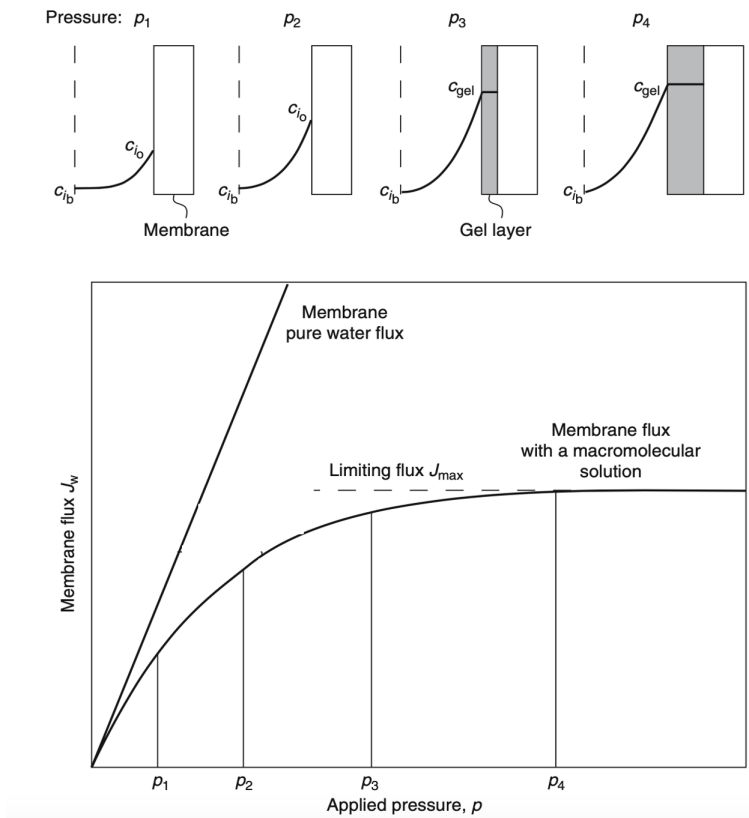


Figure 1.7: The effect of pressure on ultrafiltration membrane flux and the formation of a secondary gel layer. Ultrafiltration membranes are best operated at pressures below  $P_2$  when the gel layer has not formed. Operation at high pressures such as those above  $P_3$  leads to formation of thick gel layers, which consolidate over time, resulting in permanent fouling of the membrane[20]



## CHAPTER 2

### LITERATURE REVIEW

For decades, polymeric ultrafiltration membranes were fabricated via phase inversion (NIPS), which is a simple and scalable process to form flat or hollow fiber membranes with large areas.[25, 26]. In the last decade, alternative membrane fabrication methods that provide control over membrane properties are also suggested. For example, by using self-assembly of block copolymers[27, 28, 29] and zwitterionic amphiphilic copolymers[30, 31] significant improvement has been achieved not only in the degree of control over membrane structure in relationship to polymer properties, but also in ultrafiltration and nanofiltration range selectivity.

Fabricating membranes from the bottom-up, starting from well-defined building blocks and assembling these in a controlled manner to form selective membrane layers of well-defined pore size, porosity, and thickness, is an alternative approach for better control over membrane properties. Layer-by-layer assembly of polyelectrolytes for the fabrication of nanofiltration and reverse osmosis membranes can be considered as the most prominent example of this approach, where by tuning the type of polyelectrolyte, ionic strength and pH of the coating solutions membrane properties can be adjusted [32, 33, 34]. Membranes formed by assembling nanofibers[35, 36], nanoparticles[37, 38, 39] and 2D nanosheets [40, 41, 42] have also been demonstrated in several studies in literature. These approaches that summarized in Figure 2.1 typically rely on depositing the building blocks on a porous support layer via coating or dead-end filtration and offer control over the membrane structure primarily through the building block's properties.

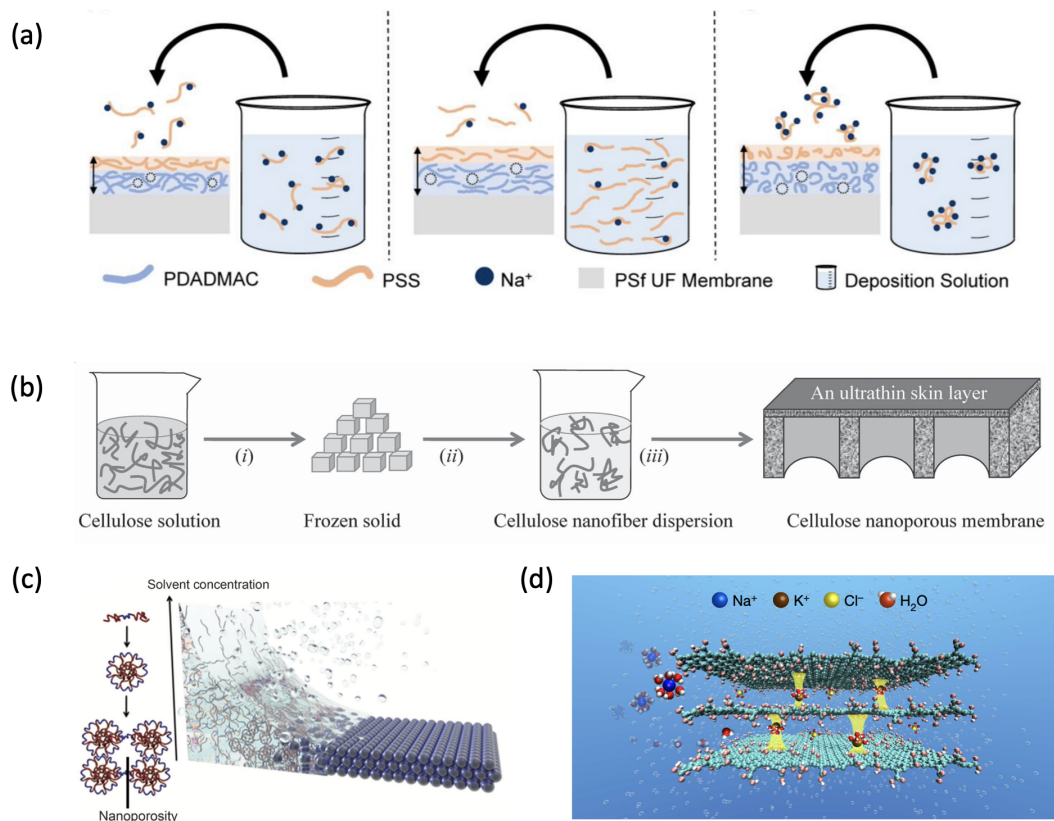


Figure 2.1: (a) Formation of polyelectrolyte multilayer nanofiltration membrane. Membrane pore structure is determined by the polyelectrolyte and salt concentrations of the deposition solution due to interactions between the polyelectrolyte and salt.[33] (b) Fabrication of ultrathin cellulose nanoporous membranes by nanofibers. Illustration of the membrane fabrication process: (i) the very dilute cellulose solution was frozen to form cellulose-NMMO solids, (ii) the frozen solids were extracted in water to produce the cellulose nanofibers, and (iii) the cellulose nanofibers were used to form an ultrathin nanoporous membrane by direct filtration.[35] (c) Sketch of the membrane formation by nanoparticle assembly: during the course of the solvent evaporation, the increase of the block copolymer concentration triggers their self-assembly into micelles, which assemble in three dimensions forming a dynamic interactive membrane film. [37] (d) A schematic representation of 2D nanosheets used for graphene oxide membranes (GOM). K<sup>+</sup> ions in a GOM determine and fix the interlayer spacing such that other cations are rejected while pure water can penetrate. Yellow pillars between the graphene oxide sheets depict the fixation of interlayer spacing by hydrated K<sup>+</sup>. [43]

A further advantage of these bottom-up approaches is that they can typically be employed by using water as the solvent, whereas in NIPS, most membrane polymers need to be dissolved in polar aprotic solvents such as n-methyl pyrrolidone (NMP) and dimethyl formamide (DMF), which are reprotoxic. In 2018, NMP was added by the European Union to the REACH Annex XVII, restricted substances list[44] and research efforts in replacing harmful and toxic solvents with more benign ones in NIPS are increasing.[45, 46, 47]. Recently, aqueous phase separation (APS) has been introduced as a novel, sustainable method of fabricating membranes using responsive polymers and polyelectrolyte complexes as membrane polymers and water as the sole solvent.[48, 49, 50, 51, 52]

Considering the impact on the nature of membrane production, it is important to choose materials less harmful to nature and human beings as membrane materials. Cellulose is a good alternative to synthetic polymers for membrane fabrication in that content. Cellulose and its derivatives have been used as membrane polymers since the early times of membrane technology. In time, they have been mostly replaced by synthetic polymers.[24] Thus, cellulose nanocrystal, which is the derivative of cellulose, with unique properties such as high resistance to extreme pH and temperature and higher specific strength compared to bulk cellulose, is a promising material for membrane fabrication.

Cellulose nanocrystal is not only renewable and biodegradable material but also, due to their aspect ratio, ease of functionalization, and controllable assembly can attract considerable interest for different applications. The predictable and altered assembly of CNCs into ordered structures results in a variety of interesting properties on the macroscale.[53] Several methods have been used to control the degree of alignment of cellulose nanocrystals, such as electric[54] and magnetic field[55, 56] application on nanocrystals, rotational shearing[57], and shear casting.[58, 59, 60, 61] Shear applying on CNC to control their degree of alignment is easy to apply method, compared to other time-consuming and expensive procedures such as application of the magnetic and electric field.[58] In previous studies, the shear-flow alignment of CNCs was investigated by different techniques such as small-angle neutron scattering[62, 14], polarized optical microscopy[60, 59], atomic force microscopy[58] and UV-visible spectroscopy[63] and all of these studies show that the degree of alignment of CNCs

increased with the increasing amount of shear that applied on CNCs. The most common experimental technique for the formation of a shear-aligned structure is the doctor blade casting, where the CNCs suspensions with a concentration above the critical concentration are cast on solid support by a withdrawal blade, as shown in the Figure 2.2. The resultant CNC layer shows an overall alignment in the direction of the withdrawal plate and the applied shear direction. The shear alignment of CNCs used in various applications such as the fabrication of optical films, sensors, 3D printing, coatings, and flexible electronics.[53]

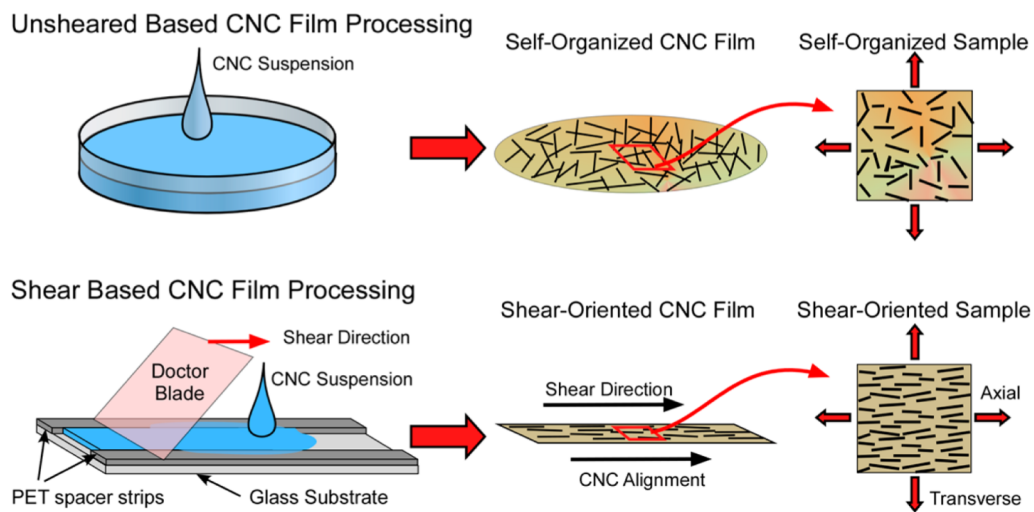


Figure 2.2: Schematic of CNC film processing and the configuration of the test samples extracted from the as cast films for (a) unsheared and (b) shear casting. The directionality of the shear cast films was defined as “axial” or “transverse” for the direction parallel to or perpendicular to the shear direction.[59]

The colloidal stability of cellulose nanocrystals and isotropic to anisotropic phase change sensitivity can be altered by adding electrolytes to CNC suspensions.[2, 17, 18, 64, 65] The presence of electrolytes affects electrostatic interactions between nanocrystals. The relation between electrolytes and CNC assembly is rationalized by DLVO theory, which uses two main interactions between nanocrystals; electrostatic double-layer repulsions and van der Waals attractions between two charged nanocrystals. Electrolyte addition results in the compression of EDL; as a result, it causes an increase in the aspect ratio of cellulose nanocrystal, a decrease in distance between

nanocrystals, and the pitch size of CNCs. Based on Onsager's predictions, with the higher aspect ratio of CNC at low concentrations, the chiral order of CNCs can be enhanced. However, at high concentrations of electrolytes, CNCs lose their stability and may form aggregates (or tactoids) in the suspension. [17, 18]. The behavior of CNC with the addition of salts was used for the formation of ion-induced CNC hydrogels[66] and CNC films with altered structures where the pitch size of CNCs within the optical film is controlled by salt addition.[17]

The cellulose nanocrystal films in the presence of various salts with varying concentrations were fabricated in a previous study. The addition of salt resulted in the decrease of the pitch size of the CNCs in the resultant film, as a result of compression of EDL.[17] (Figure 2.3) As seen in Figure 2.3, the POM images of CNC films showed that the salt addition resulted in the formation of CNC tactoids; at high concentrations, these tactoids coalescences. Thus, the study showed that the addition of electrolytes to the aqueous suspension of CNCs could tune the structure of CNC films.

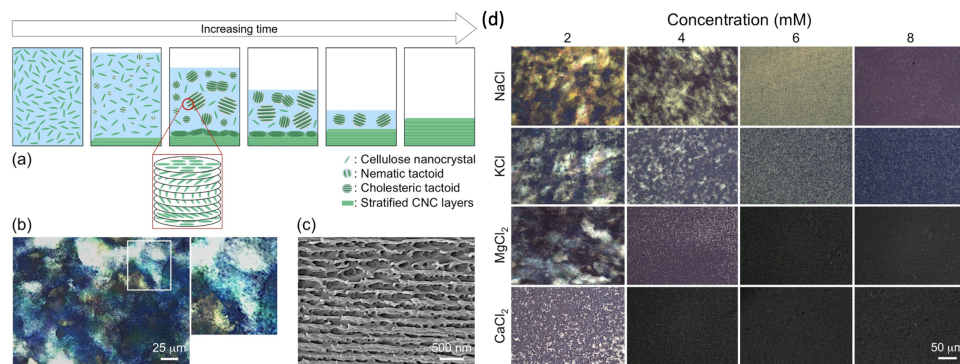


Figure 2.3: Schematic illustration of CNC film formation from CNC suspensions as water evaporates. A lyotropic phase transition occurs as the CNC concentration reaches  $C^*$  upon drying. Tactoids nucleate and grow over time to yield larger anisotropic domains. (b) POM image of a CNC film revealing optical birefringence due to the locked-in cholesteric mesophase (the pitch is visible in the 2x enlargement of the identified region). (c) Cross-sectional cryofractured SEM image displaying a layered morphology. (d) POM images of mesomorphic films cast from aqueous suspensions containing 3 wt% CNC and 4 different salts (labeled on left) at 4 different concentrations (labeled on top). The scale bar applies to all images.[17]

CNC films are usually fabricated by drop-casting (or solution casting) on solid support from different researchers.[60, 59, 8] However, this method has some limitations, such as; the duration of waiting time for the water to evaporate completely to form CNC film, the use of concentrated CNC suspensions to achieve controlled structures, the lack of the comprehensive control over the resultant film homogeneity and the thickness. Thus, in another study, vacuum-assisted filtration of CNC on a support layer was used as a new way to fabricate CNC optical films. In the study, to remove water from CNC suspensions to obtain anisotropic CNC films, CNC suspension was filtered on a filter paper instead of complete evaporation of water, and the resultant layer was used as an optical film.[67, 68]

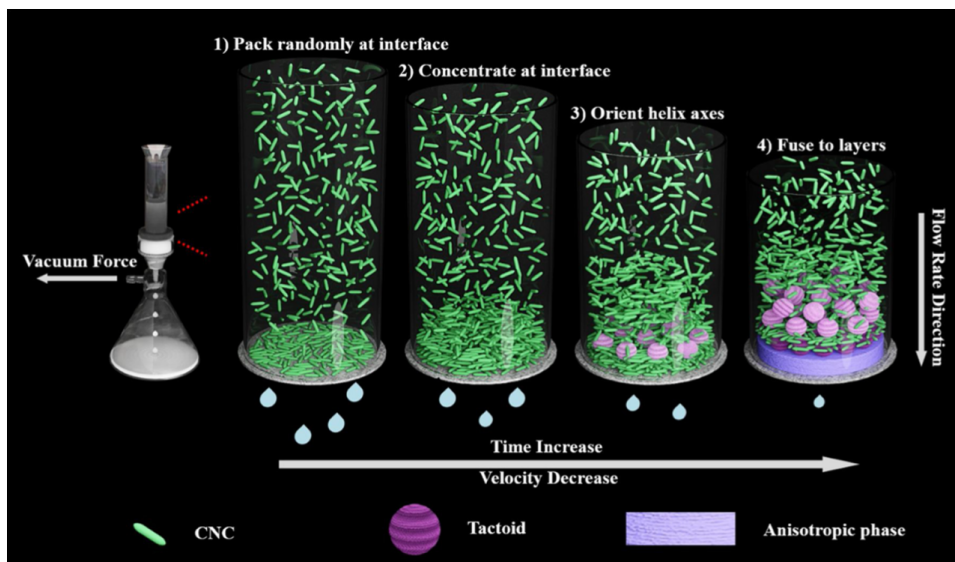


Figure 2.4: Schematic representation of the vacuum-assisted CNC self-assembly process [67]

In a previous study, cellulose nanocrystals were deposited on a porous support layer using a dead-end filtration module to be further used as ultrafiltration membranes. [69] The filtered cake CNC layer on the support was stabilized by filtering highly concentrated multivalent  $AlCl_3$  salt, which caused the formation of irreversible coagulates of CNCs. This approach was previously used for the formation of nanopaper from cellulose nanofibril filters, where the cake layer was used for ultrafiltration[70] and nanofiltration[71] membrane.

This study combined the CNC's unique characteristics, such as controllable assembly and tunable electrostatic interactions, to fabricate structured CNC membranes by depositing CNCs on a support layer by tangential filtration. This novel approach enables us to control the degree of alignment of CNCs. Thanks to the shear applied to CNCs during tangential flow filtration, we altered the finalized morphology of the deposited CNC layer. Further, we controlled the spacing between CNCs by changing the suspension's ionic strength and pH, which enabled us to fabricate CNC with tuned structures. These controlled CNC structures were destabilized on the porous support layer to be further used as membranes. The resultant membranes showed a tunable rejection and permeances by changing the easy-to-apply membrane fabrication properties such as tangential flow rate, ionic strength, and pH of the CNC suspension.





## CHAPTER 3

### EXPERIMENTAL PROCEDURES

#### 3.1 Materials

Cellulose (cotton linter, medium fibers), cellulose acetate (Mn = 50000), sulfuric acid H<sub>2</sub>SO<sub>4</sub>, 95-97%), aluminum chloride hexahydrate (AlCl<sub>3</sub>6H<sub>2</sub>O, 99%), 1-ethyl-3-methylimidazolium acetate ([EMIM]OAc, 95%), sodium hydroxide (NaOH), Rose Bengal (RB, 95.0 %, 973 Da), Vitamin B12 (1356 Da), Blue Dextran (5 kDa), and  $\beta$ -lactoglobulin (18 kDa) were purchased from Sigma-Aldrich. Dimethyl sulfoxide (DMSO, 99.0%), Crystal Violet (CV, 88% Dye content, 408 Da), Dimethylformamide (DMF, 99.5%) and acetone (99.5%) were purchased from Merck. Ethanol (99.5% purity) was purchased from J.T. Baker.

#### 3.2 Preparation of Cellulose Nanocrystal (CNC) Suspensions

CNC suspensions were prepared by sulfuric acid hydrolysis of cotton linter as described in Figure 3.1. The cellulose was hydrolyzed at 45°C in 64% (w/v) aqueous sulfuric acid solution for 30 min. The mixture was then quenched in cold ultra-pure water at a volume three times the reaction volume to stop the reaction. Then, the solution was washed with ultra-pure water at least five times, and the resultant mixture was dialyzed against ultrapure water until the pH in the suspension remained constant at around 3. Neutral cellulose nanocrystal suspensions were prepared by adding NaOH (0.1 M) to acidic suspensions. The concentration of the suspension batch was measured with a Shimadzu DTG-60 thermogravimetric analyzer (IKA 36400.00) and a Shimadzu MOC63u moisture analyzer. To disperse CNCs in suspensions com-

pletely, Bandelin SonoPlus MS 2.5 ultrasonic processor was used for 10 min while the suspensions were kept in the ice bath. An HB 10 rotary evaporator was used to concentrate suspensions where the solvent, water, was removed from the initial aqueous suspension slowly at 38°C . This way, 1.5, 2, 3.2, and 6.4% (w/v) suspensions were prepared for rheology and capillary flow experiments.

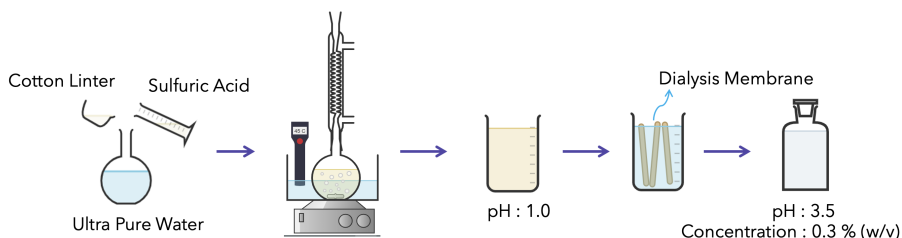


Figure 3.1: Cellulose nanocrystal suspension synthesis by sulfuric acid hydrolysis of cotton linters

### 3.3 Cellulose Nanocrystal Suspension Characterization

#### 3.3.1 Rheological Analysis of CNC Suspensions

Rheological analyses of cellulose nanocrystal suspensions were performed using an Anton Paar MCR302 modular compact rheometer with cone-plate geometry. Steady shear viscosity behavior with varying shear rates ( $0.01-100 \text{ s}^{-1}$ ) was investigated for each suspension with a pH value of 3. To minimize the evaporation of the sample, evaporation blocker was used during the analysis. All rheological measurements were performed at 25°C.

#### 3.3.2 Stability Analysis of CNC Suspensions

HI88703 HANNA turbidimeter was used to measure the turbidity of CNC samples with varying electrolyte concentrations. Zeta potentials of suspensions were measured using Zetasizer Ultra (Malvern Instruments) at 25°C; 10 mL of 0.1 % (w/v) CNC suspensions with varying electrolyte concentrations were subjected to Bandelin SonoPlus MS 2.5 ultrasonic processor for 5 minutes before the measurements.

### 3.3.3 Capillary Flow of CNCs

For quantification of the shear alignment of the CNCs, suspensions with various concentrations (1.5, 2, 3.2, and 6.4% (w/v)) were pumped through a capillary glass tube with a diameter of 500  $\mu\text{m}$  using a New Era NE-1000 syringe pump at flow rates ranging from 1000 to 9000  $\mu\text{Lh}^{-1}$  with varying wall shear rates from 20 to 200  $\text{s}^{-1}$ . During suspension flow, the capillary tubes were placed between crossed-polarizers of an optical microscope (Olympus BX53M) for the optical analysis.

### 3.3.4 CNC Suspension Flow Simulations

Three-dimensional (3D) simulations of CNC suspension flow in a capillary tube and the tangential flow filtration module were conducted using COMSOL Multiphysics v.5.2a to compute the shear rate and shear stress distributions during cellulose nanocrystal suspension motion. Reynolds numbers (Re) the CNC suspensions with a concentration of 0.3% (w/v) are calculated, and it is found that the Reynolds number was changed from 0.78 to 7, with changing volumetric flow rate in the capillary from 1000 to 9000  $\mu\text{Lh}^{-1}$ . Thus, the capillary flow CNC suspensions were assumed as laminar. In addition, it was assumed that the fluid discharges to the atmospheric pressure, the density of the fluid is 1000  $\text{kgm}^{-3}$ , and suspensions obey non-Newtonian power-law characteristics.

## 3.4 Cellulose Nanocrystal Membrane Fabrication

### 3.4.1 Fabrication of Support Layer

Two different casting solutions were used for the fabrication of transparent support layers. For preparing Support I, first, 1-ethyl-3-methylimidazolium acetate was heated at 90  $^{\circ}\text{C}$  for 1 h and 70  $^{\circ}\text{C}$  for 3 h to remove volatile impurities. After that, cellulose (12 wt %), acetone (25 wt %), and pretreated [EMIM]OAc (63 wt %) re-cooled to room temperature were mixed using a roller mixer. Support II was prepared from a casting solution prepared by mixing cellulose acetate (15 wt%) and DMSO

(85 wt%) using a magnetic stirrer. Support layers were cast at room temperature at a thickness of 250  $\mu\text{m}$  using a casting bar on a glass substrate. The coagulation of the solutions was performed in a water bath. For Support I, before the coagulation process, the cast solution was placed in a 6 L evaporation flask with dry nitrogen flow at a rate of 0.6  $\text{Lmin}^{-1}$  for 30 min for evaporating acetone from the cast solution. For complete coagulation and solvent exchange, the support layers were washed in deionized water for 24 h and then stored in 20% aqueous ethanol solution until use. Representative fabrication steps of support membranes are shown in Figure 3.2. The pure water permeance of the support layers before CNC filtration experiments was measured to have a reference value for the support-layer resistance.

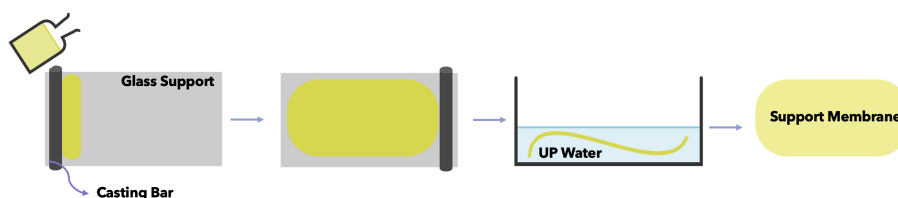


Figure 3.2: Support layer fabrication by phase inversion steps

### 3.4.2 Fabrication of Cellulose Nanocrystal Deposit Layer

Tangential flow filtration of CNC suspensions was performed in a lab-made setup with a Sterlitech CF042A crossflow cell ( $42 \text{ cm}^2$ ), Masterflex peristaltic pump, for providing tangential flow of the feed, and a Swagelok back-pressure regulator was used for adjusting the feed side pressure (Figure 3.3). Typically, as the feed solution CNC suspension (pH=3) with a CNC concentration of 0.3% (w/v) was used. Filtration experiments were performed at constant feed flow rates with varying transmembrane pressures (TMPs) on each support to observe the limiting flux. Experiments were repeated at least three times with different feed flow rates ranging from 9 to 80  $\text{mLmin}^{-1}$ .

To see the effects of electrostatic interactions between cellulose nanocrystals on CNC deposit layer structure, salty CNC feed suspensions with varying ion valence ( $\text{NaCl}$ ,  $\text{CaCl}_2$  and  $\text{AlCl}_3$ ) and different concentrations (0, 1, 5, 25 and 50 mM) were used. CNC suspension with neutral pH was also used to investigate the pH effect on deposit

layer structure. Tangential flow filtrations were performed at flow rates of 9 and 80 mLmin<sup>-1</sup>. Again, for each deposited layer, limiting flux was reached at different TMP values.

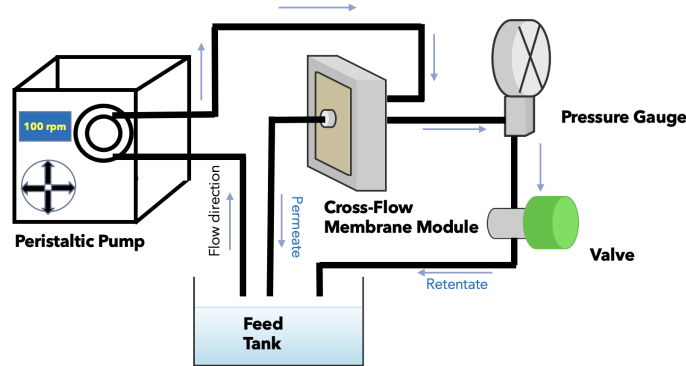


Figure 3.3: Tangential flow filtration system used for fabrication of cellulose nanocrystal membranes

### 3.4.3 AlCl<sub>3</sub> Treatment of Cellulose Nanocrystal Deposit Layer

After CNC filtration (deposition), a 200 mM aqueous AlCl<sub>3</sub> solution was permeated through the membranes in the dead-end mode for irreversible coagulation of CNCs on the support surface. [71, 70] Lastly, excess AlCl<sub>3</sub> within the CNC layer was washed via pure water permeation in the dead-end mode, and pure water permeance values of CNC-deposited membranes were measured. After the deposition, CNC deposit-layer resistances of fabricated membranes were predicted using Darcys law and resistances in the series model.

$$R = \frac{\text{TMP}}{\eta \cdot J} \quad (3.1)$$

$$R_m = R_s + R_c \quad (3.2)$$

where  $R$  is the resistance against the flow,  $\text{TMP}$  is the transmembrane pressure applied across the membrane,  $\eta$  is the viscosity of the permeate at the temperature of the experiment, and  $J$  is the permeate flux.  $R_m$ ,  $R_s$ , and  $R_c$  represent the resistance of

the CNC-deposited membrane, the resistance of the support layer, and the resistance of the formed CNC deposit, respectively. Resultant CNC deposit layers with varying tangential feed flow rates, the salt concentration in the feed, and initial pH value of the feed are tabulated in Table 3.1

Table 3.1: CNC Membranes

Membrane	Flow rate (mLmin <sup>-1</sup> )	NaCl Conc. in Feed (mM)	pH of the Feed
CNC9	9	0	3
CNC30	30	0	3
CNC80	80	0	3
CNC200	200	0	3
CNC9-1	9	1	3
CNC9-5	9	5	3
CNC9-25	9	25	3
CNC9-50	9	50	3
CNC80-1	80	1	3
CNC80-5	80	5	3
CNC80-25	80	25	3
CNC80-50	80	50	3
CNC9-pH7	9	0	7
CNC80-pH7	80	0	7

#### 3.4.4 Membrane Separation Tests

Probe molecules (vitamin B12, Blue Dextran,  $\beta$ -lactoglobulin, rose bengal, and crystal violet) with varying molecular weights were used in the filtrations. Probe molecule feed solutions were prepared with water, with probe concentrations of 0.03, 0.08, 0.01, 0.015, and 0.016 mM. Tangential flow filtration of probe solutions was done in the same lab-made setup used for CNC deposition at 0.4 bar transmembrane pressure (TMP) and 20 mLmin<sup>-1</sup> feed flow rate. The percent rejection (R %) of a probe was calculated as;

$$R\% = \left(1 - \frac{C_P}{C_R}\right) * 100\% \quad (3.3)$$

where  $C_P$  and  $C_R$  are the concentrations of the tested compound in the permeate and retentate, respectively. Samples were taken from permeate and retentate lines for analysis during the filtration, until the rejection became constant. Concentrations of probe molecules were measured using a Shimadzu UV-1601M UV-visible spectrophotometer.

### **3.5 Optical Characterizations**

#### **3.5.1 Polarized Optical Microscopy**

Polarized optical microscopy (Olympus BX53M) equipped with retardation plates was used for alignment characterizations of CNC suspensions and CNC-deposited membranes. Image analyses were performed using ImageJ.

#### **3.5.2 Atomic Force Microscopy**

Atomic force microscopy (AFM) was carried out using the Veeco MultiMode V microscope in the tapping mode for alignment characterizations of the CNC-deposited membranes and the size measurements of CNCs. The suspension was sonicated using an ultrasonic processor to obtain well-dispersed nanocrystals for particle size analysis. The obtained CNC suspension (0.03% (w/v)) was then spin-coated onto a flat silicon wafer surface and was dried at ambient conditions. Membranes prepared for the alignment analysis of CNCs were also dried before the AFM analysis.

#### **3.5.3 Scanning Electron Microscopy**

A Quanta 400F field emission microscope was used for further optical analysis of the membranes. Samples were fractured in liquid nitrogen and dried in vacuum, and sputter-coated with Au/Pd before imaging.





## CHAPTER 4

### RESULTS AND DISCUSSIONS

In this thesis, we sought to develop a new way to fabricate ultrafiltration membranes with controllable separation performances using cellulose nanocrystals as the membrane material. This way, we aimed to create the possibility of using water as the only solvent in the membrane fabrication. We used intrinsic properties of cellulose nanocrystals, such as shear-alignment, to tune the membrane structure, as well as membrane performances. In the second part, we utilized the electrostatic interactions between cellulose nanocrystals to alter the membrane structure with its performance.

#### 4.1 Shear Aligned Cellulose Nanocrystal Membranes

##### 4.1.1 Cellulose Nanocrystals

Cellulose nanocrystals synthesized by sulfuric acid hydrolysis have negatively charged sulfate groups that promote electrostatic repulsion on the nanocrystal surface and lead to the formation of highly stable acidic CNC suspensions. Phase and rheological behaviors of CNC suspensions depend on the aspect ratio of the nanocrystals and the suspension stability.[1] Due to sulfuric acid hydrolysis, the pH of the synthesized CNC suspension with a concentration of 0.3% (w/v) was measured as 3. Based on AFM results (Figure 4.1), the average length of nanocrystals was  $180 \pm 11$  nm, and the average diameter was  $8 \pm 3$  nm. Both pH and aspect ratio are consistent with previous reports where cotton linter was hydrolyzed in sulfuric acid for the CNC synthesis.[12]

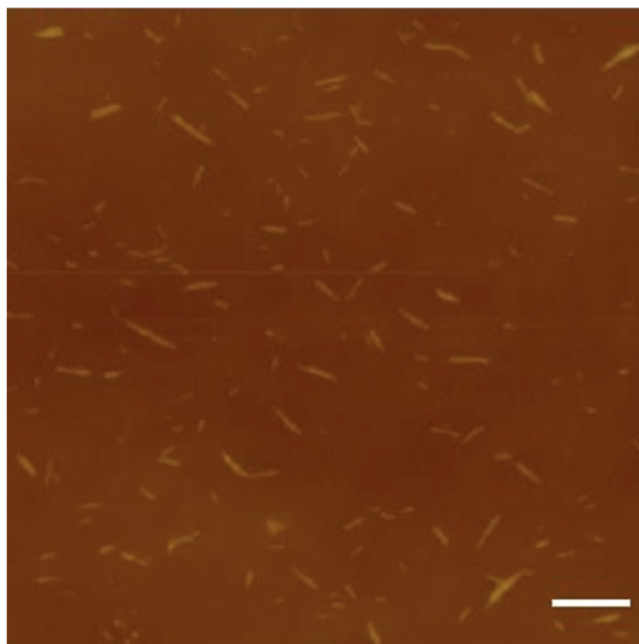


Figure 4.1: Atomic force microscopy 2D height image of CNCs. Scale bar: 250 nm

#### 4.1.2 Rheology of Cellulose Nanocrystals

For the investigation of the CNC phase behavior, rheological analysis was performed with suspensions at different concentrations (1.5, 2, 3.2, and 6.4% (w/v)) with CNC suspension pH value of 3. The shear rate dependence of the steady viscosity for each concentration is shown in Figure 4.2. For the 1.5% (w/v) suspension, nearly Newtonian behavior was observed at a broad range of applied shear rates, indicative of the random orientation of CNCs in the suspension consistent with its isotropic phase.[72] For the concentrated suspensions of 2-3.2% (w/v), shear-thinning behavior at low shear rates (region I), the plateau region at intermediate shear rates (region II), and second shear-thinning behavior at high shear rates (region III) were observed. This behavior can be easily followed by inset in Figure 4.2. This three-regime behavior of cellulose nanocrystal suspensions is typically associated with characteristics of lyotropic liquid crystals and can be explained by the ordering of liquid crystal domains under applied shear as described in the Chapter1.[2]

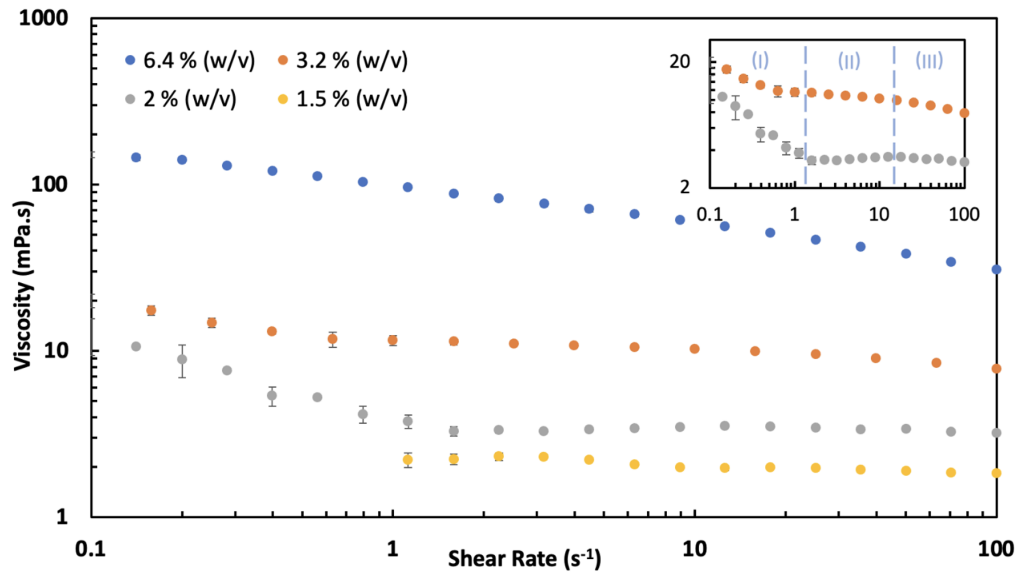


Figure 4.2: Steady shear viscosity of 6.4% (w/v) (blue), 3.2% (w/v) (orange), 2% (w/v) (gray), and 1.5% (w/v) (yellow) aqueous CNC dispersions as a function of shear rate.

Critical concentration ( $C^*$ ) where the phase change of cellulose nanocrystal suspension occurs from isotropic to biphasic phase is calculated by using Onsager Model, Equation 1.1 provided in Chapter 1. Using this model,  $C^*$  was predicted to be 2.1% (w/v), which agrees with  $C^*$  determined as 2% (w/v) based on the rheological analysis (Figure 4.2). For the suspension with 6.4% (w/v) concentration, the shear thinning behavior was observed at the entire range of shear rates, which can be interpreted as the gelation of CNCs at high nanocrystal concentration in the suspension, consistent with the literature.[16, 73]

#### 4.1.3 Flow Characteristics of Cellulose Nanocrystal Suspensions

To investigate the combined effect of suspension concentration on the shear-dependent flow alignment of CNCs, suspensions with varying concentrations were pumped through a transparent capillary tube placed in between crossed-polarizers of an optical microscope. Polarized light images of the suspensions with respect to concentration and suspension flow rates are shown in Figure 4.3, where the columns are on the order of increasing flow rates and the rows are on the order of increasing suspension concen-

tration.

No bright color appearance was seen under polarized light for the 1.5% (w/v) suspension at any flow rate, consistent with the isotropic phase seen in rheological analysis (Figure 4.2). However, for the 2% (w/v) suspension, although not strong, the bright appearance is first observed at flow rate  $2000 \mu\text{Lh}^{-1}$ , and the intensity of the light increased with increasing flow rate (Figure 4.3b). When the 3.2% (w/v) suspension was pumped through the capillary with the same flow rate, the brightness was higher (Figure 4.3c). Differently, the 6.4% (w/v) suspension showed a multicolored appearance under polarized light for the entire range of shear rates (Figure 4.3d).

The differences seen under polarized light are the result of variation in both concentration and flow dynamics of suspensions. For the isotropic suspension (1.5% (w/v)), the reason brightness was not observed under polarized light is the lack of global CNC ordering inside the suspension, and therefore, the suspension did not acquire birefringence. However, the suspension with critical concentration where liquid crystalline phase formation occurs revealed brightness under polarized light as a result of the birefringence of suspensions. The observed brightness increased with an increasing flow rate for suspensions at the critical concentration and above. The reason is that during the motion of CNCs in the capillary, shear stresses that develop on the wall of the capillary result in the shear alignment of CNCs. The shear applied to CNCs increased with increasing flow rates, which resulted in a higher degree of alignment of CNCs. As a result, birefringence also increased, resulting in a brighter appearance under polarized light overall.

The colored appearance in the highest concentration suspension was also associated with birefringence change of suspension with an increasing degree of ordering and can be explained by the Michel-Levy chart, which illustrates the relationship among retardation, thickness, and birefringence of a sample.[74] For CNC suspensions in capillary tubes, the thickness was constant. With an increase in flow rate, and hence applied shear on CNCs, the degree of alignment of nanocrystals increases. Therefore, the birefringence of the samples (the bright color of the suspensions when imaged between crossed-polarizers) was increased. Consequently, a higher-order interference color was seen under polarized light. The sequence of the appearing colors under

polarized light, which was white, yellow-orange, and purple-blue, matches with the color change in the first order of the Michel-Levy chart (see in A.1) in the direction of increasing birefringence.[74]

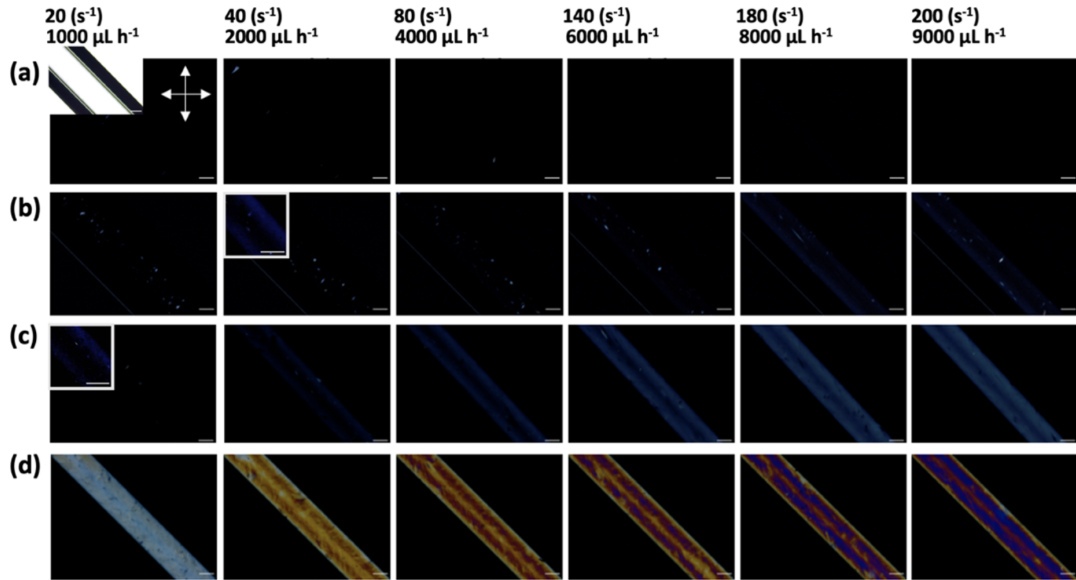


Figure 4.3: Polarized optical microscopy images of cellulose nanocrystal suspension flow in a capillary tube at different concentrations: (a) 1.5% (w/v) (inset: bright field image of the 1.5% (w/v) CNC suspension flow; inset image scale bar is  $100\mu\text{m}$ ), (b) 2% (w/v) (inset: high-exposure image of CNC at a flow rate of  $2000\mu\text{Lh}^{-1}$ ), (c) 3.2% (w/v) (inset: high-exposure image of CNC at a flow rate of  $1000\mu\text{Lh}^{-1}$ ), and (d) 6.4% (w/v) (rows); flow rates and wall shear rates (columns). Scale bar is  $250\mu\text{m}$ .

Along the capillary tube diameter, the intensity of brightness that appeared in polarized light images was measured using ImageJ for the varying CNC flow rates (Figure 4.4a). The intensity values were higher in the regions near the capillary walls than in the center zone since the developed shear stresses have their maximum value in the vicinity of the tube surfaces. As the applied shear was increased, the average alignment of the CNCs increased toward the direction of the applied shear and exhibited a higher intensity of birefringence under polarized light.

Simulation of the capillary flow of CNCs was conducted with COMSOL Multiphysics to calculate the magnitude of the shear rate with respect to the radial direction within the experimentally used flow rates.[75] The relation between shear rate and viscosity

was expressed by the power law; flow consistency and flow behavior indices were determined as 0.0021, 0.0053, 0.016, 0.1 and 0.92, 0.83, 0.76, 0.7 for the suspensions with concentrations of 6.4, 3.2, 2, and 1.5% (w/v), respectively, from data obtained from rheological analysis (Figure 4.2). The shear rate values that appeared in the vicinity of the capillary tube found by COMSOL simulations were compared with the results obtained by the analytical model (details are in AppendixC.1). The shear rate values on the wall of the capillaries were increased from 20 to 200  $s^{-1}$  by changing volumetric flow rates from 1000 to 9000  $\mu Lh^{-1}$  based on COMSOL simulations. Similarly, based on the one dimensional analytical model of capillary flow CNCs, the shear rates varied from 22.9 to 207.2  $s^{-1}$  for the suspension with the lowest concentration (1.5% (w/v)) and from 24.8 to 223  $s^{-1}$  for the suspension with the highest concentration (6.4% (w/v)) with the increase of volumetric flow rates from 1000 to 9000  $\mu Lh^{-1}$ . Hence, the simulation and one-dimensional model agreed with each other.

For the suspension with the critical concentration (2% (w/v)), at the flow rate where the first bright color appearance was observed under the polarized light (2000  $\mu Lh^{-1}$ ), the maximum shear stress appearing in the vicinity of the capillary walls was determined as 0.13 Pa (Figure 4.4b). Consistently, for the same suspension, based on the rheology measurement at the transition point of the plateau region (Region II) to the shear-thinning region (Region III) where global ordering of the CNCs starts, the shear stress value was found as 0.1 Pa (Figure 4.2). Similarly, the shear stress developed on the capillary wall during the flow of the suspension with a concentration of 3.2% (w/v) was determined as 0.18 Pa in the COMSOL simulation ((Figure 4.4c)), which agreed with the shear applied in the rheology analysis for transition to the third region of the three-region behavior of the 3.2% (w/v) suspension, which was 0.15 Pa (Figure 4.2).

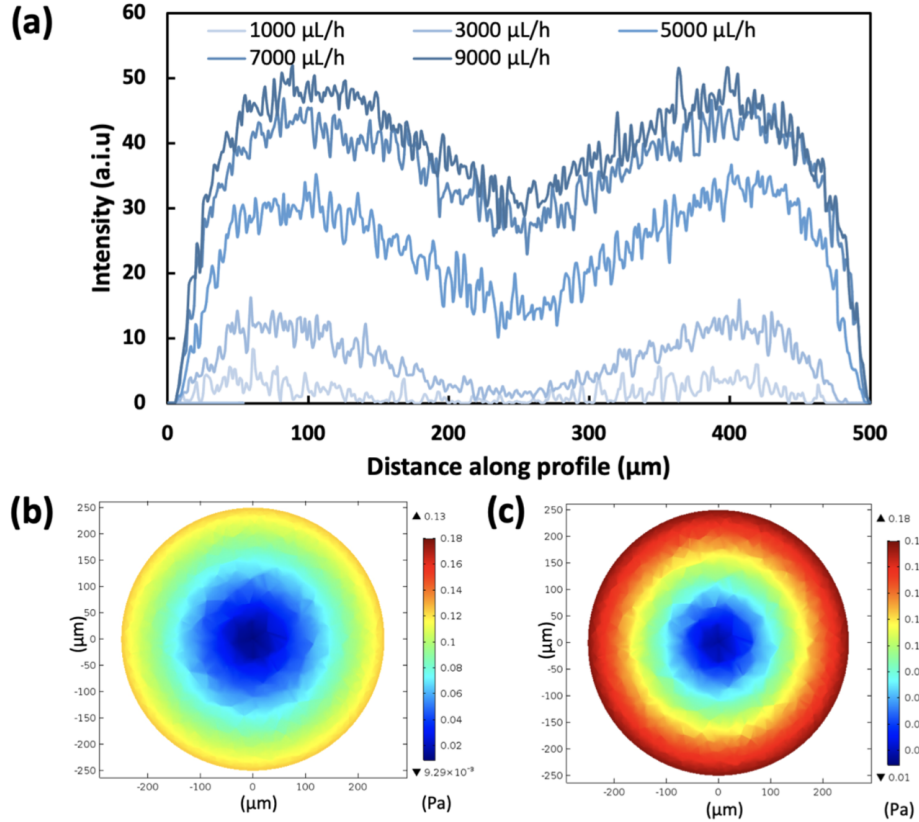


Figure 4.4: (a) Intensity profile plots with varying flow rates of CNC suspensions with a concentration of 3.2% (w/v) along the diameter of the capillary tube. Simulated shear stress profile of 2% (w/v) dispersion at flow rate 2000  $\mu\text{Lh}^{-1}$  (b) and 3.2% (w/v) dispersion at flow rate 1000  $\mu\text{Lh}^{-1}$  (c) along the capillary tube with the cross-section view.

#### 4.1.4 Shear-Aligned Deposition of CNCs

##### 4.1.4.1 CNC Deposition on Support Layers

Change in the degree of alignment of CNCs with the shear rate was exploited to deposit CNCs with different degrees of alignment on the support-layer surface by varying the tangential flow velocity during filtration of CNC suspensions. For this purpose, aqueous cellulose nanocrystal suspensions were used as feed solution and filtered tangentially to a porous support layer. The procedure for the aligned deposition of cellulose nanocrystals from aqueous suspensions is shown in Figure 4.5.

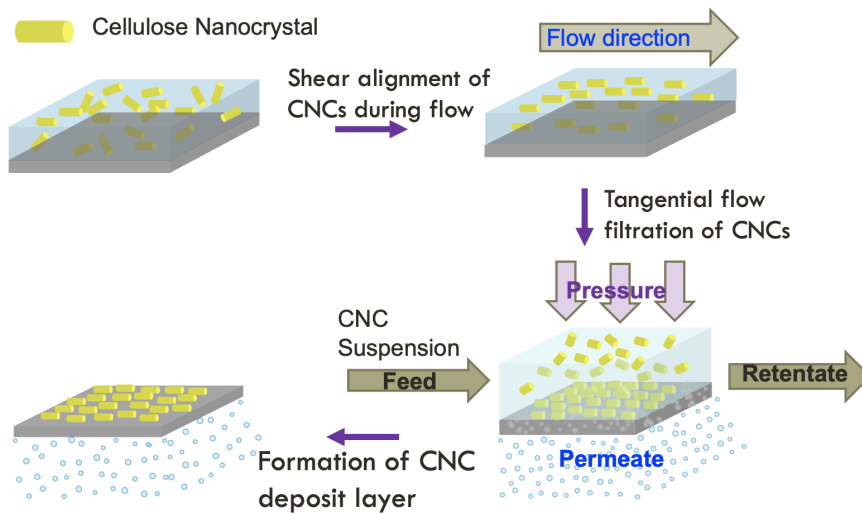


Figure 4.5: Cellulose nanocrystal suspension tangential flow filtration onto porous support layer

For deposition of CNCs, two support layers were used, which differed in permeance and transparency. Support I had a pure water permeance of  $7.0 \pm 0.5 \text{ Lh}^{-1} \text{m}^{-2} \text{bar}^{-1}$ , and support II had a pure water permeance of  $146 \pm 70 \text{ Lh}^{-1} \text{m}^{-2} \text{bar}^{-1}$  and lower transparency than Support I.

Figure 4.6a shows the permeate flux as a function of TMP during the filtration of CNC suspensions on these two support layers. The plateau observed with both supports indicates that the limiting flux is reached, and any increase in TMP once this limiting flux is reached increases the deposit layer thickness. While the TMP values where the limiting flux is reached are different for the two supports, due to their different intrinsic permeances, the limiting fluxes reached at the same tangential flow velocity are identical, and an increase in limiting flux with increasing tangential flow velocity is clearly observed. At 9, 30, 80, and 200  $\text{mLmin}^{-1}$  tangential flow rates, limiting fluxes measured on Support II are  $7.1 \pm 0.7$ ,  $8.1 \pm 1.5$ ,  $11 \pm 0.8$ , and  $13.7 \pm 1.2 \text{ Lh}^{-1} \text{m}^{-2}$ , respectively, increasing with increasing tangential flow rate as expected. The same trend is observed for Support I, which has a much lower pure water permeance itself, while the limiting flux at 80  $\text{mLmin}^{-1}$  was measured as  $10.7 \text{ Lh}^{-1} \text{m}^{-2}$ , almost identical to that seen on Support II.



The increase in limiting flux with increasing tangential velocity is a consequence of the higher convective mass-transfer coefficient,  $k_c$ , at a higher tangential velocity. As seen in Equation 1.2, at the same bulk suspension concentration,  $C_{bulk}$ , and with the gel concentration,  $C_{gel}$ , being an intrinsic property of the CNC suspension, the ratio of permeate flux,  $J$ , to the mass-transfer coefficient,  $k_c$ , is a constant. By plotting the limiting flux as a function of the bulk suspension concentration of CNCs at three values (0.36, 0.18, and 0.05 % (w/v)) and extrapolating the linear relationship between the limiting flux and the logarithm of the bulk concentration,  $C_{gel}$  was estimated as 5.9% (w/v) (Figure 4.6 b). [20] Concentration at which the single shear-thinning behavior was observed, 6.4% (w/v), in the rheological analysis (4.2), attributed to the gelation of CNCs. [73, 16]

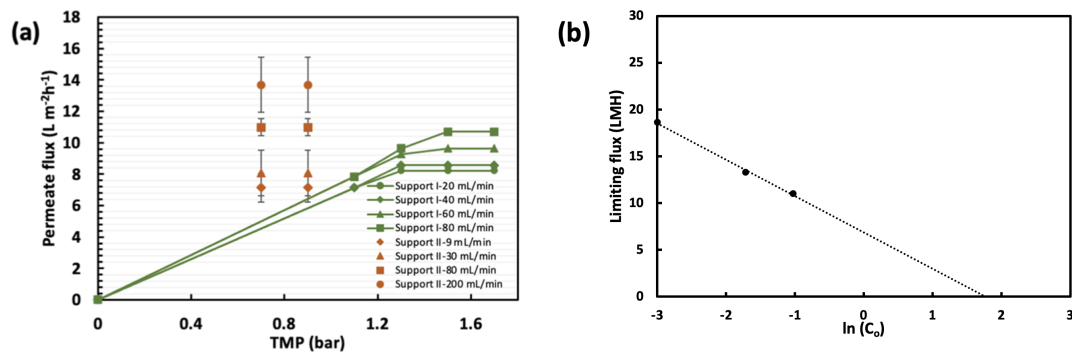


Figure 4.6: (a) Permeate flux as a function of transmembrane pressure (TMP) for various feed flow rates during the filtration of CNCs (0.3 % (w/v)) on Supports I and II (after determining the limiting flux on Support I, only two TMP values with fluxes both at the limiting value were applied for CNC membrane preparation by CNC deposition on Support II) (b) Estimation of gel concentration from experimental data based on gel-polarization model

Sulfuric acid hydrolysis of cellulose yields negatively charged sulfate groups on the CNC surface, which provide high stability of nanocrystals in the suspension medium due to electrostatic repulsion. The stability of CNC suspensions can be reduced by salt addition, which causes screening of electrostatic interactions. [18] After deposition of CNCs on the porous support layer, to destabilize the CNC suspension resting on the support and, as a result, ensure a stable CNC layer to act as the selective membrane, a 0.2 M AlCl<sub>3</sub> solution, which is suitable to destabilize CNCs (Figure 4.7a),

was permeated through the CNC-deposited support in the dead-end mode. As a result of salt permeation, CNCs with reduced colloidal stability collapsed on the support layer, and a stable CNC layer was obtained (Figure4.7b). The CNC layer, which easily dispersed back into the water without salt filtration, was stable in water after the  $\text{AlCl}_3$  treatment. The CNC deposit could also be obtained as a free-standing layer after the dissolution of the cellulose acetate support in DMSO (Figure4.7c).

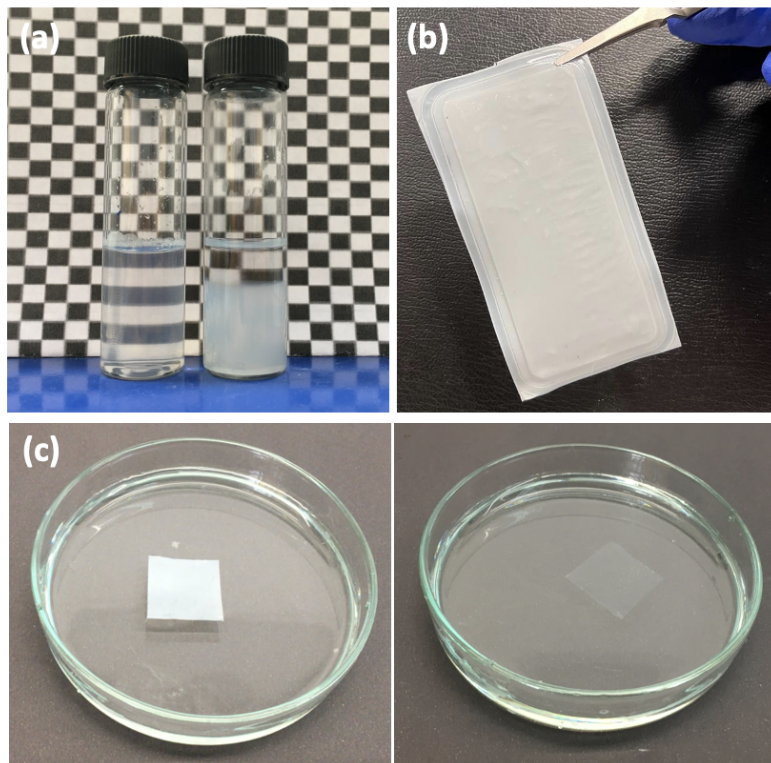


Figure 4.7: (a) Cellulose nanocrystal suspension with concentration of 0 mM (left) and 200 mM (right)  $\text{AlCl}_3$  (b) Fabricated CNC80 membrane after deposition of CNCs via 0.2 mM  $\text{AlCl}_3$  salt filtration on Support II (c) CNC80 placed in DMSO solution before (a) and after (b) the Support II dissolved in DMSO

Resistance of the CNC layer was calculated after CNC filtration at varying flow rates and after salt permeation, based on Darcy's law and the resistances-in-series model (Figure4.8a). CNC-layer resistances observed directly after CNC filtration slightly decreased with increasing feed flow rate until  $200 \text{ mLmin}^{-1}$ . This trend also followed the thickness of the CNC deposit layers, revealed by SEM images of cross-sections of deposits, which decrease with increasing flow rate (Figure4.8b).

After  $\text{AlCl}_3$  permeation through the CNC deposit, the resistance of the layer increased due to the compression of the deposited colloids upon screening of electrostatic interactions at high ionic strength. This increase, however, is less marked for the CNC layers deposited at 80 and 200  $\text{mLmin}^{-1}$ , likely due to the higher degree of liquid crystalline order in these layers that are less mobile for compression and reorganization, which is confirmed in the following sections.

Specific resistances of each membrane were calculated by dividing CNC layer resistances to CNC layer thicknesses measured by cross-section SEM images, and found as 1.56, 1.67, 1.84 and  $2.33 \times 10^{-18} \text{ m}^{-2}$  for CNC feed flow rates of 9, 30, 80 and 200  $\text{mLmin}^{-1}$ , respectively (Figure 4.8a). The increasing specific resistances with increasing feed flow rates showed that the higher flow rate of CNCs during tangential flow rate filtration results in more compact CNC deposit layers.

Pure water permeance values of resultant membranes after  $\text{AlCl}_3$  treatment were increased with increasing tangential flow filtration rates. The PWP values were determined as  $6.3 \pm 1.1$ ,  $6.3 \pm 1.7$ ,  $9.7 \pm 3.2$  and  $11.7 \pm 3.6$  for feed flow rates 9, 30, 80 and 200  $\text{mLmin}^{-1}$ , respectively.

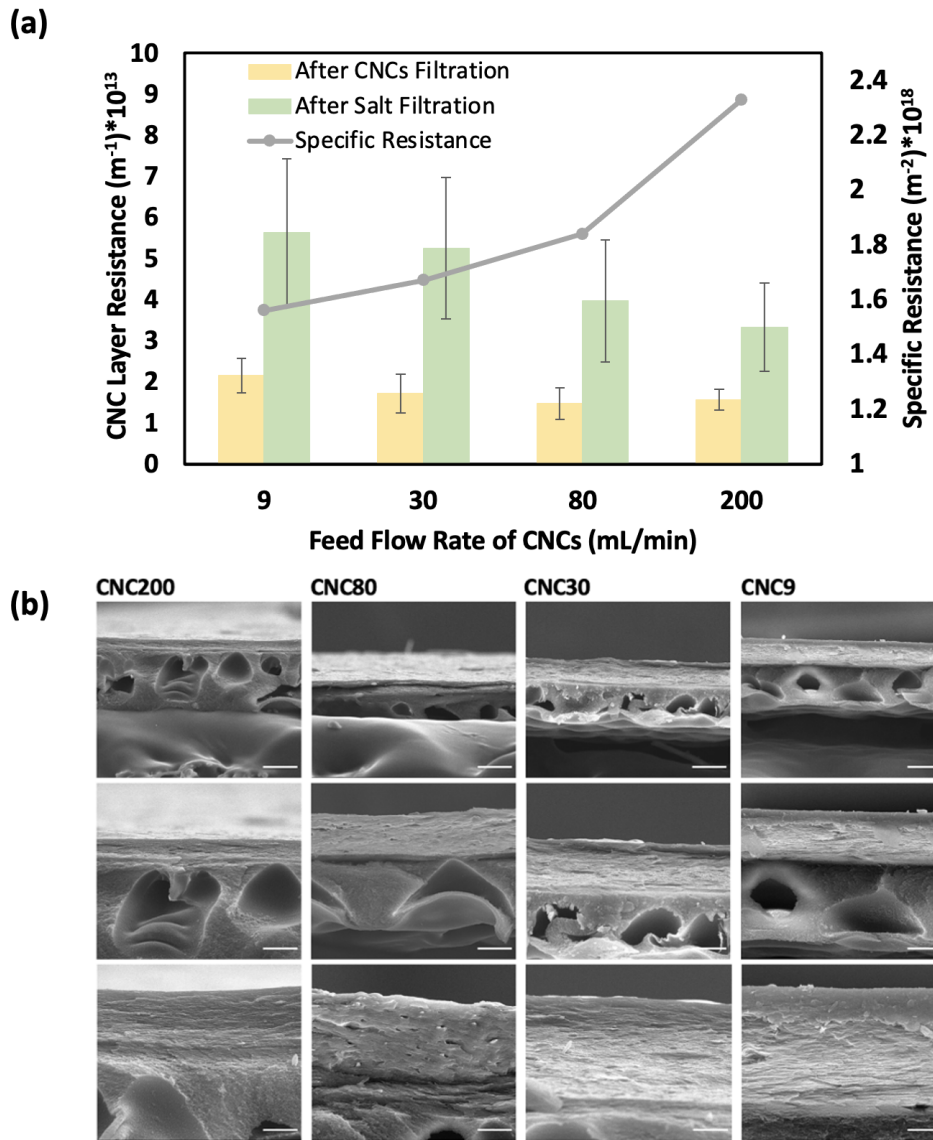


Figure 4.8: (a) CNC deposit resistance (left axis) after CNC filtration on Support II and after salt permeation for CNC membranes fabricated under different flow rates, calculated by Darcy's law and resistances in series. Specific resistances of each membrane, calculated by deposit resistances of each membranes divided by CNC layer thickness (right axis) (b) Scanning electron microscopy images of cross section of membranes (CNC200, CNC80, CNC30 and CNC9). Measured thicknesses for CNC200, CNC80, CNC30 and CNC9 are  $14.3 \pm 0.9$ ,  $21.6 \pm 2.5$ ,  $31.5 \pm 2.3$ ,  $36.2 \pm 1.4$   $\mu\text{m}$  Scale bars:  $50 \mu\text{m}$  (first row),  $25 \mu\text{m}$  (second row),  $10 \mu\text{m}$  (third row).

#### 4.1.4.2 Shear Alignment of the Deposited CNC Layer

CNCs tangential flow was performed at two different porous support layers, Support I with denser structure but higher transparency and Support II with looser structure with relatively low transparency. Both support layers were suitable for optical analysis since none have the birefringence. Brightfield and polarized light images of empty Support I (a) and Support II (b) are shown in Figure 4.9.

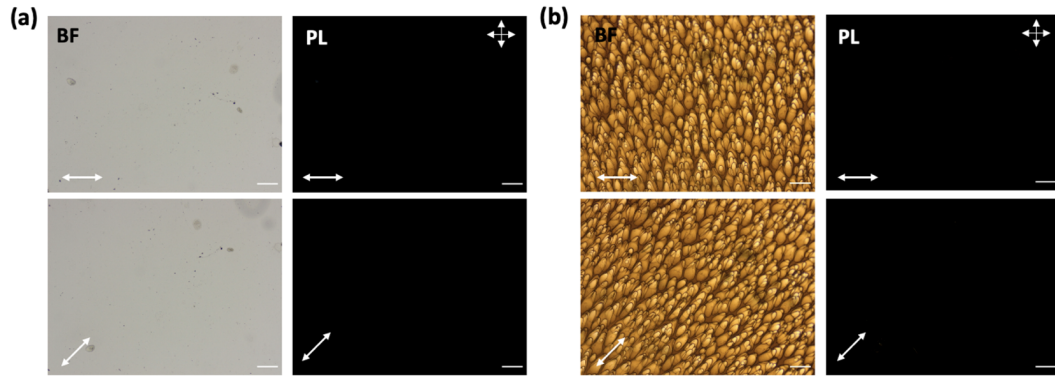


Figure 4.9: Brightfield (BF) and polarized light (PL) optical images of empty Support I (a) and Support II (b). Single white arrow represents the membrane position with respect to analyzer. Crossed white arrows show the direction of analyzer and polarizer. Scale bars: 250  $\mu\text{m}$

During the tangential filtration of CNCs in suspension on the porous support, the nanocrystals were expected to align in the direction of the shear developed on the support surface. After the critical concentration of CNCs reached on the support layer, where the CNCs acquire the birefringence, the orientation of CNCs can be analyzed by a polarized optical microscope as a result of their birefringence.

As can be seen in Figure 4.10a, dark images were observed under crossed-polarizers when the feed flow direction during deposition was in the same direction as one of the crossed-polarizers. When the membrane was placed so that the feed flow direction during deposition was  $45^\circ$  with the polarizers, a bright appearance was obtained (Figure 4.10a). The brightness of the transmitted light reached its maximum at this orientation, indicative of the CNC alignment in this direction. To further prove this, the membrane placed between the crossed-polarizers was rotated according to

the analyzer ( $0^\circ$ ) and the polarizer ( $90^\circ$ ) with a full ( $360^\circ$ ) turn. Mean gray values were calculated in polarized images of the membrane taken during this motion (Figure 4.10b). When the flow direction was aligned with the polarizer and the analyzer, the mean gray value was found to be minimum, while this value was maximum at  $45^\circ$  multiples. When analyzed using the polarized optical microscope equipped with a first-order retardation plate, coloring with a blue hue at  $45^\circ$  and an orange-yellow hue at  $135^\circ$  with respect to the analyzer also evidenced the alignment direction of CNCs in the deposited layer (Figure 4.10a, insets).

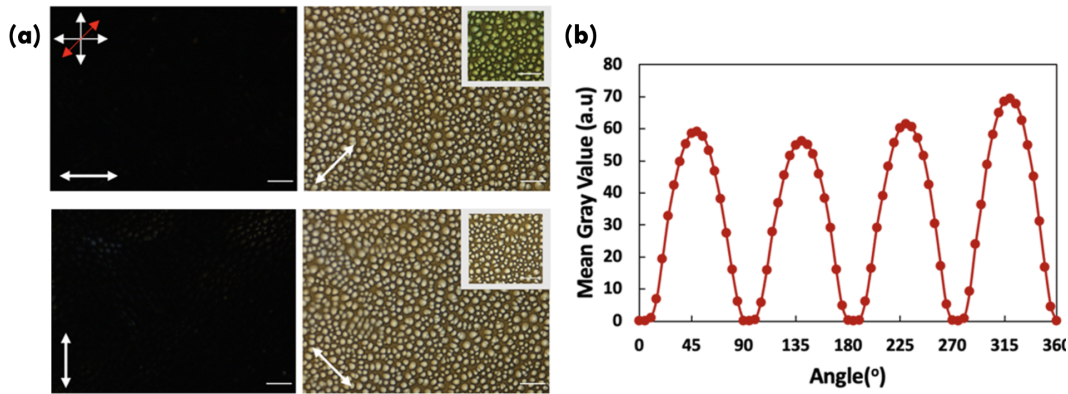


Figure 4.10: (a) Polarized light images of the middle part of CNC-deposited membranes with a flow rate of  $80 \text{ mLmin}^{-1}$  and feed concentration of 0.3% (w/v). Single white arrows represent the feed flow direction. Crossed arrows show the direction of the analyzer and polarizer. Scale bar is  $250 \mu\text{m}$  (insets: first-order retardation plate images; additive red arrow to crossed-polarizers represents the direction of the first-order retardation plate; and the inset scale bar is  $100 \mu\text{m}$ ). (b) Mean gray values of polarized light images with respect to the angle of deposition of the CNC membrane in (a) to the analyzer angle.

The average degree of alignment of CNCs depends on the amount of shear applied during the flow of CNC suspensions (Chapter 1), which indicates that the degree of alignment of CNCs could be controlled during the filtration of CNC suspensions by changing the feed flow rate. The second shear-thinning region (Region III) was observed at shear rates higher than  $10 \text{ s}^{-1}$  for the concentrated suspensions (2, 3.2, 6.4% (w/v)) where the large domains of CNCs align in the flow direction (Figure 4.2). Based on this observation, it was aimed to apply shear rates greater than  $10 \text{ s}^{-1}$  during

the flow of CNC suspension in tangential filtration. The feed flow rates required to achieve these shear rate values were determined by simulating the flow of CNCs in the tangential flow filtration module in 3D with COMSOL Multiphysics.[75] The simulation results were used to relate the feed flow rate of the filtration to the local shear rate appearing in the filtration module (Figure 4.11). The filtrations at 9, 20, 30, 40, 60, and 80 mL mLmin<sup>-1</sup> CNC suspension flow rates were simulated, and for these flow rate values, the mean shear rate values generated in the middle region of the filtration module were determined as 5, 10, 15, 20, 30, and 40 s<sup>-1</sup>, respectively. As a result, the CNCs deposited at feed flow rates above 20 mLmin<sup>-1</sup> were expected to show a preferential alignment at the support surface. The simulation of tangential flow in the module suggests that the shear rate is somewhat higher along the center-line of the module.

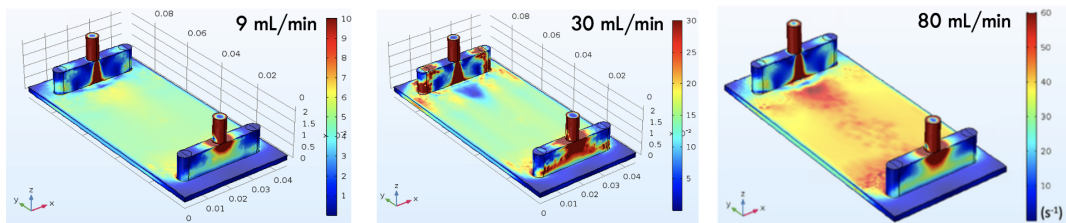


Figure 4.11: Simulated shear rate profile of CNC suspension flow at the surface of the tangential flow filtration module with the feed flow rate of 80 mLmin<sup>-1</sup>.

Figure 4.12 shows polarized optical images of membranes fabricated via deposition of CNCs at different feed flow rates. As can be seen in Figure 4.12a, at high shear rate values formed on the support surface depending on the high feed flow rate, a bright appearance is obtained when the membrane is rotated 45° clockwise to the analyzer. At these high shear rates, the majority of CNCs were aligned in the common direction giving strong birefringence. However, the intensity of the brightness decreases with a decline in shear rates (Figure 4.12 b,c). The optical images suggest that there was no helical twist formation at shear rates between 20 and 50 s<sup>-1</sup>, as a single white bright appearance was observed. On the other hand, as also indicated in rheological analysis results, at a shear rate of 10 s<sup>-1</sup>, the applied shear was not enough to align the CNCs in a uniform nematic order.[76] The optical appearance shown in Figure 4.12d and the layered, periodic appearance of the cross section of the deposited films (Figure

4.12e) are supportive of the possible formation of helical phases of the deposited films, consistent with literature examples.[17] The mean gray value profile along the cross-section view of the CNC9 membrane showed a periodicity of ca.  $1.6 \mu\text{m}$  (Figure 4.12f). Overall, the difference observed in the optical images is an indication that the alignment of the CNCs in the deposit can be controlled by shear, which changes as a result of the change in the feed flow rate.

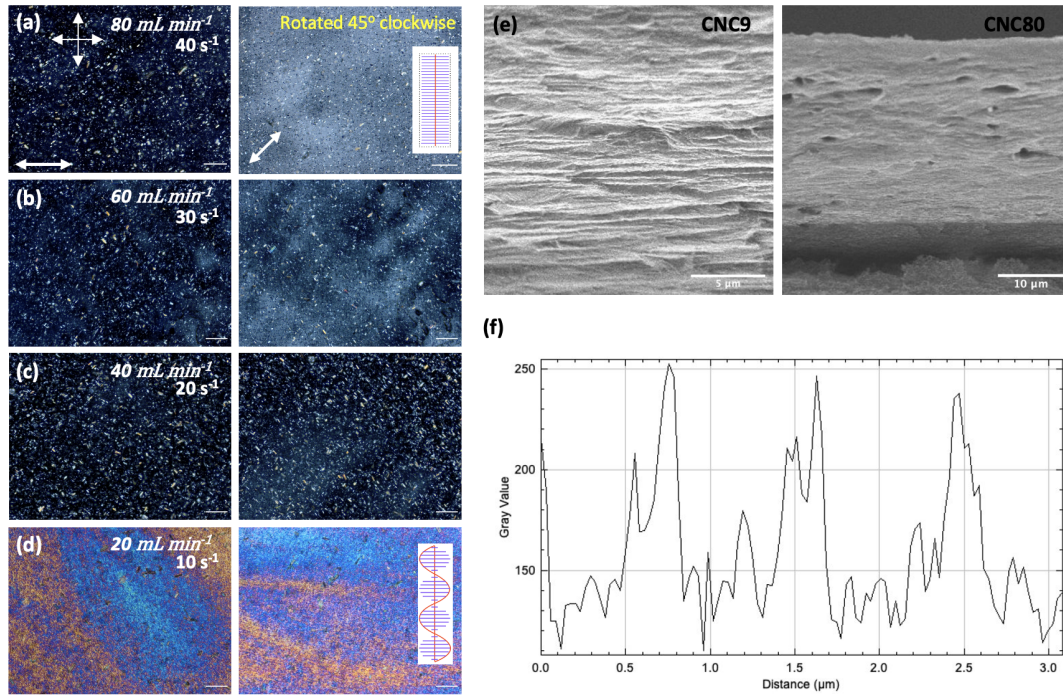


Figure 4.12: (a) Polarized light images of CNC-deposited membranes on Support I placed with feed flow in the same direction with the polarizer (first column) and rotated  $45^\circ$  clockwise to the analyzer (second column) with a feed concentration of 0.3% (w/v). Single white arrows represent the feed flow direction. Crossed arrows show the direction of the analyzer and polarizer. Feed flow rates and generated mean shear rate values in the central region of the modules during the CNC filtration: (a)  $80 \text{ mLmin}^{-1}$ ,  $40 \text{ s}^{-1}$ ; (b)  $60 \text{ mLmin}^{-1}$ ,  $30 \text{ s}^{-1}$ ; (c)  $40 \text{ mLmin}^{-1}$ ,  $20 \text{ s}^{-1}$ ; and (d)  $20 \text{ mLmin}^{-1}$ ,  $10 \text{ s}^{-1}$ . Inset sketches (a) and (d) represents the nematic and cholesteric order of the membranes. Scale bar is  $250 \mu\text{m}$ . (e) Scanning electron microscopy images of cross sections of CNC9 and CNC80 membranes (f) Mean gray profile along the SEM cross-section view of CNC9 membrane



The degree of alignment was also investigated in terms of the number of nanocrystals aligned in the flow direction for three different CNC suspension flow rates of 200, 80, 30, and 9 mLmin<sup>-1</sup>, where membranes were named as CNC200, CNC80, CNC30, and CNC9, respectively. AFM phase images are shown in Figure 4.13. Angular histogram plots of the number of aligned nanorods with respect to the flow direction indicate that over 60% of CNCs in CNC200 and CNC80 membranes exhibit preferentially a parallel alignment (0-30°) to the flow direction (Figure 4.13, bottom panel). With decreasing flow rate, the number of parallel aligned nanocrystals decreased. For CNC30, and ca. 50% of the nanocrystals oriented in the range of 0-30°. For the 9 mLmin<sup>-1</sup> feed flow rate, there was no preferential alignment of CNCs, and the nanocrystals were distributed between 0 and 90°.

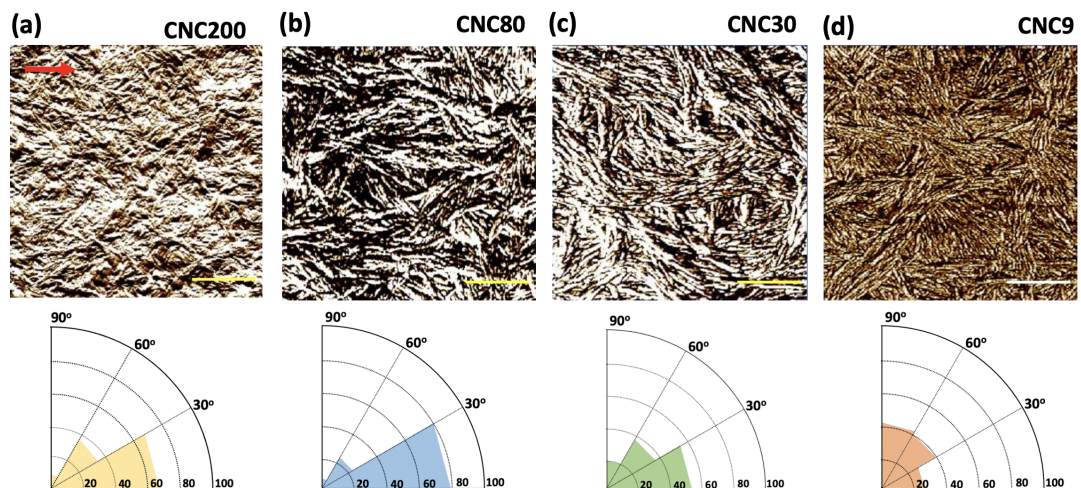


Figure 4.13: AFM top-view phase images of CNC-deposited membranes (a) CNC200, (b) CNC80, (c) CNC30, and (d) CNC9. Red arrow indicates the direction of feed flow during filtration. Scale bar is 250 nm. Bottom panel shows the polar histograms for each membrane for the % aligned nanocrystals where the reference axis is the CNC flow direction.

The order parameter,  $S$ , of each sample was calculated by the following equation;[77]

$$S = \frac{\{3 \cos^2 \theta - 1\}}{2} \quad (4.1)$$

where  $\theta$  is the angle between the nanocrystal and the reference axis; CNCs flow direction. The order parameter was determined as 0.7 for the CNC80 membrane, where a more uniform alignment of CNCs was observed: 0.48 for CNC30 with an intermediate flow rate and 0.17 for CNC9 where the nanocrystals were randomly deposited on the support membrane. The increase in order parameter values with an increase in applied shear on nanocrystals was consistent with the literature where the order parameter increased linearly and reached a plateau at a high shear rate.[62]

#### 4.1.4.3 Separation Performance of Shear Aligned Membranes

Cellulose nanocrystal membrane performance tests were carried out using three different compounds with different molecular weights. During the selection of the support membrane, it was important that the porous support did not have a significant rejection to the tested probes so that it would not affect the evaluation of deposited CNC layers. The rejection values of Support II were measured as 2.6, 4.1, and 26% for the tested vitamin B12 (B12, 1356 Da), Blue Dextran (BD5, 5 kDa), and  $\beta$ -lactoglobulin ( $\beta$ L, 18 kDa) compounds, respectively. As a result of these negligible rejection values and the higher permeance, CNC membranes fabricated on Support II were used in performance tests. Percent rejections of CNC membranes are summarized in Figure 4.14.

Experiments were carried out with CNC membranes that were fabricated with the following feed flow rate values: 80 mLmin<sup>-1</sup>, where the highest alignment of nanocrystals was observed (CNC80); 30 mL mLmin<sup>-1</sup>, where a relatively lower degree of alignment was observed (CNC30); and finally, 9 mLmin<sup>-1</sup>, where CNCs were not aligned in the shear direction (CNC9), based on the optical analysis. For vitamin B12 (1 kDa), no significant rejection was observed in any of the membranes. However, with the increase in the molecular weight of the probes to 5 and 18 kDa, rejections increased for all membranes. Furthermore, the rejection for each probe increased with increasing feed flow rate used in tangential flow filtration and hence the increase in the

alignment of CNCs. As can be seen in Figure 4.14, rejection values were measured as 93.7% ( $\beta$ L), 92.7% (BD5), and 31.4% (B12) for CNC80 membranes, whereas these rejection values decreased with decreasing alignment in CNC30 and CNC9 for each probe. The difference is distinguished most clearly in BD5 rejections, where partial rejection is observed in all membranes. B12 is rejected to a very small extent by all membranes, implying that all membrane pores are significantly larger than the molecule diameter. For  $\beta$ L, over 90% rejection is obtained with all three membranes, and the difference with increasing shear is less marked than for BD5. This is presumably because the diameter of  $\beta$ L is closer to all membranes' pore diameters, allowing the more ordered packing in CNC80 to increase the rejection by a smaller extent. On the other hand, when there is partial rejection, an increase in the ratio of the solute diameter to pore diameter, from CNC9 to CNC80, increases the probe's rejection to a larger extent.

The CNC80 membranes were tested against charged probes Rose Bengal (RB, negatively charged, 973 Da) and crystal violet (CV, positively charged, 408 Da). CNC80 rejected 93 % of RB; even though its molecular weight was lower than the molecule that CNC membranes did not show significant rejection, vitamin B12 (1356 Da). The high rejection performance was interpreted as negatively charged sulfate groups on the CNC membrane surface repelling the negatively charged RB molecules. Surprisingly, high rejection performance (93%) of CNC80 was observed against positively charged CV molecules. The color change of the CNC membrane was visible after the filtration test, unlikely to the membranes tested with RB molecules (Appendix B.1). The material balance around membrane showed that 20% of the filtered CV molecules sorbed on the membrane surface. Thus, the sorption of molecules on the membrane surface may cause a change in the membrane characteristics, resulting in the high rejection of positively charged molecules by the CNC membrane.

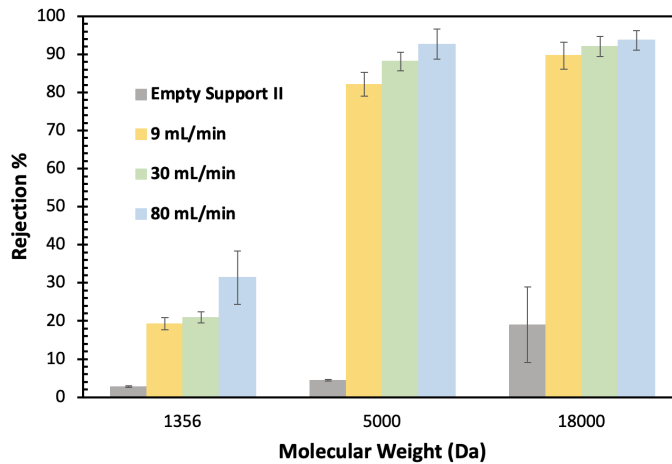


Figure 4.14: Percent rejection values of the empty support membrane (Support II) and membranes fabricated at CNC suspension feed flow rates of 9 mLmin<sup>-1</sup> (CNC9), 30 mLmin<sup>-1</sup> (CNC30), and 80 mLmin<sup>-1</sup> (CNC80) against different probes with varying molecular weights.

#### 4.1.5 CNC Membranes with Tuned Electrostatic Interactions

##### 4.1.5.1 Cellulose Nanocrystals in Presence of Salts

Cellulose nanocrystals synthesized by sulfuric acid hydrolysis of cotton linter have negatively charged sulfate groups on the surface and form highly stable aqueous suspensions due to electrostatic repulsion between sulfate groups.[2] Increasing ionic strength in these suspensions suppresses the electrical double layer (EDL) and decreases the magnitude of electrostatic repulsion forces between the charged colloids.[17, 18] A thinner EDL allows the CNCs to pack more tightly, and lower repulsive forces cause destabilization of the suspensions above a certain salt concentration (Figure4.15.[17]

As the EDL thickness decreases with ionic strength, chloride salts of monovalent (Na<sup>+</sup>), divalent (Ca<sup>2+</sup>), and trivalent (Al<sup>3+</sup>) ions at varying concentrations were tested. Figure 4.16a shows the turbidity of CNC suspensions with a pH value of 3, in the presence of NaCl, CaCl<sub>2</sub>, and AlCl<sub>3</sub>, as an indication of colloidal stability. As expected, turbidity increased in the presence of salts, which indicated CNC aggregation. At any salt concentration, the turbidity is higher with Al<sup>3+</sup>, followed by Ca<sup>2+</sup> and then Na<sup>+</sup>,

showing the more substantial destabilizing effect of higher valence ions. CNC suspension photographs also agreed with the turbidity measurement; the sedimentation of the samples was increased with the increasing salt concentration in the suspension, as shown in Figure 4.16b after 1 day of equilibration.

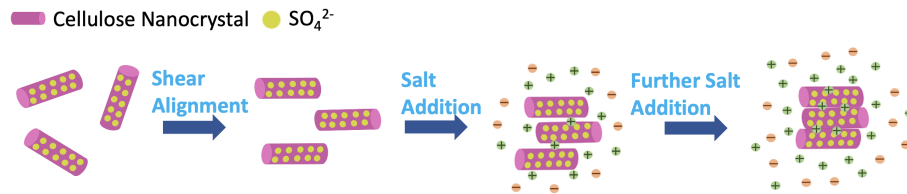


Figure 4.15: Change in distance between cellulose nanocrystal with the increase of salt concentration in the suspension

The pH dependence of the aggregation of the CNCs was also investigated in terms of turbidity of the samples upon salt addition. As shown in Figure 4.16c, at varying salt concentrations, sedimentation of CNCs suspensions with initial pH of 7 was more pronounced compared to suspensions prepared with an initial pH of 3.

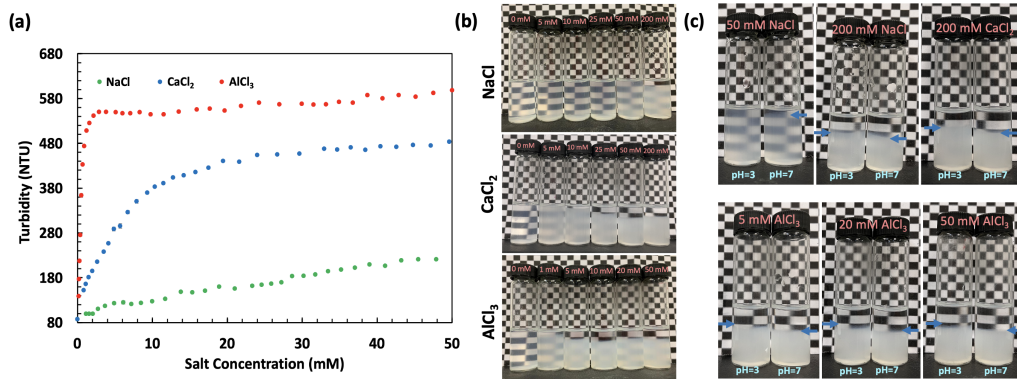


Figure 4.16: (a) CNC suspension (0.3 % (w/v)) turbidity for varying salt concentrations and salt valence, (b) photographs of CNC suspensions with pH=3 upon salt addition with varying ion valence (c) CNC suspensions with pH values of 3 and 7, with 50 mM NaCl, 200 mM NaCl, 200 mM  $\text{CaCl}_2$ , 5 mM  $\text{AlCl}_3$ , 20 mM  $\text{AlCl}_3$  and 50 mM  $\text{AlCl}_3$  (photographs were taken after 1 day of sample preparation). Small blue arrows indicate the level of CNC aggregation phase within suspension.

To further investigate the colloidal stability of cellulose nanocrystals in the presence of electrolytes, the interaction potential energy ( $V$ ) between nanocrystals in NaCl additive suspensions was calculated by the equation based on DLVO theory[78, 79];

$$V = (V_A) + (V_R) \quad (4.2)$$

where the  $V_A$  is the attractive van der Waals potential energy and  $V_R$  is the repulsive potential energy. NaCl was preferred for the analysis since it's also revealed by turbidity analysis, CNC suspensions form irreversible aggregates rapidly with multiple-valence salts. Assuming cellulose nanocrystals as cylindrical rods with length ( $L$ ) of 180 nm and diameter ( $a$ ) of 8 nm, Sparnaay's expressions used for interaction energies. The repulsive potential interactions between for parallel ( $V_R^P$ ) and crossed ( $V_R^C$ ) nanorods are given by the following expressions:

$$V_R^P = 64\pi^{0.5} \frac{(\kappa a)^{0.5}}{\kappa^2} nkT\gamma^2 L \exp(-\kappa H) \quad (4.3)$$

$$V_R^C = 128\pi \frac{\alpha}{\kappa^2} nkT\gamma^2 \exp(-\kappa H) \quad (4.4)$$

$$\gamma = \tanh\left(\frac{e\psi_0}{4kT}\right) \quad (4.5)$$

$$\kappa = \sqrt{\frac{e^2 \sum_i C_i z_i^2}{\varepsilon_0 \varepsilon kT}} \quad (4.6)$$

where  $n$  is the number density of ions,  $k$  is the Boltzmann constant,  $T$  is the temperature,  $e$  is the charge of an electron,  $H$  is the distance between nanocrystals,  $\psi_0$  is the surface potential,  $\kappa$  is the reciprocal Debye length in an electrolyte,  $\varepsilon_0$  is the vacuum permittivity,  $\varepsilon$  is the relative permittivity,  $C_i$  is the bulk electrolyte concentration, and  $z_i$  is the charge of electrolyte. Surface potential values were approximated as  $\zeta$ -potentials of CNC suspensions with the pH value of 3.5. For suspensions with concentrations of 0, 1, 5, 25 and 50 mM NaCl,  $\zeta$ -potential values were measured as  $-54 \pm 1$ ,  $-37.3 \pm 3$ ,  $-34.8 \pm 2$ ,  $-29 \pm 0.6$ , and  $-26 \pm 1$ , respectively. Debye length ( $\kappa^{-1}$ ), of CNC suspensions with NaCl concentrations of 1, 5, 25 and 50 mM were calculated and found as 9.55, 4.27, 1.91 and 1.36 nm, respectively. Potentials for attractive forces between parallel ( $V_A^P$ ) and crossed ( $V_A^C$ ) nanorods given by the following equations;

$$V_A^P = \frac{(-ALa)^{0.5}}{24H^{1.5}} \quad (4.7)$$

$$V_A^C = \frac{-Aa}{6H} \quad (4.8)$$

A is the Hamaker's constant and calculated as  $1.1 \times 10^{-20}$  J by the equation ;

$$A = (\sqrt{A_{11}} - \sqrt{A_{22}})^2 \quad (4.9)$$

with  $A_{11}(1.1 \times 10^{-20}$ J) Hamaker's constant for cellulose particles,  $A_{22}(4.38 \times 10^{-20}$ J) Hamaker's constant for water.[78]

The total interaction potential energies both for parallel and crossed nanocrystals were calculated using Equations 4.3-4.9 (Figure 4.17). To approach each other, large energy barriers the nanocrystals should overcome were observed for parallel and cross-oriented nanocrystals at different suspension salinity. By increasing salt concentration from 1 mM to 5 mM, the maximum potential was slightly increased from 180 kT to 192 kT for parallel orientation but decreased to 149 kT and then to 108 kT with increasing salt concentration from 5 mM to 25 mM and then 50 mM, respectively. For cross-orientation, a continuous decrease was observed for the energy barrier corresponding to increase of the salt concentration. The reduction in the maximum potential, resulting from the reduction in Debye length and increase of the ion density for both orientations, indicates that nanocrystals tend to approach each other with the increase in salt concentrations. But still, at the investigated concentration range (1-50 mM), cellulose nanocrystals can stay stable to some degree in the suspension since their energy barriers are sufficiently higher than kT.[80]

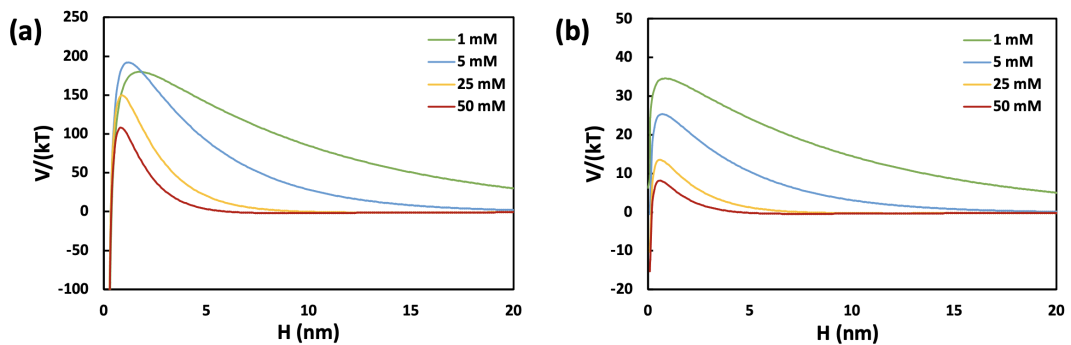


Figure 4.17: Internal potential energies of cellulose nanocrystals at different salt concentrations in parallel (a) and cross (b) orientation

#### 4.1.5.2 Electrostatic Interactions Effects on CNC Membranes

The electrostatic interactions of cellulose nanocrystals were utilized here to deposit a dense CNC layer as a selective membrane by filtering CNC suspension at varying salt concentrations or pH over porous support in tangential flow. To investigate the effect of ionic strength on the resultant CNC deposit layer, which is the selective layer of the membrane, CNC suspensions for the tangential-flow filtration were prepared with chloride salts with different valences, namely, NaCl, CaCl<sub>2</sub> and AlCl<sub>3</sub> and of varying concentrations. The CNC-AlCl<sub>3</sub> suspension was not suitable for filtration as it formed irreversible aggregates even at low concentrations (5 mM) in the feed tank resulting in poor control over the CNC deposit. Membrane formation by CNC-CaCl<sub>2</sub> suspensions of 5-25 mM was not reproducible, with a large scatter in probe rejection among membranes fabricated under the same conditions, also implying extensive aggregation. (Figure 4.18)

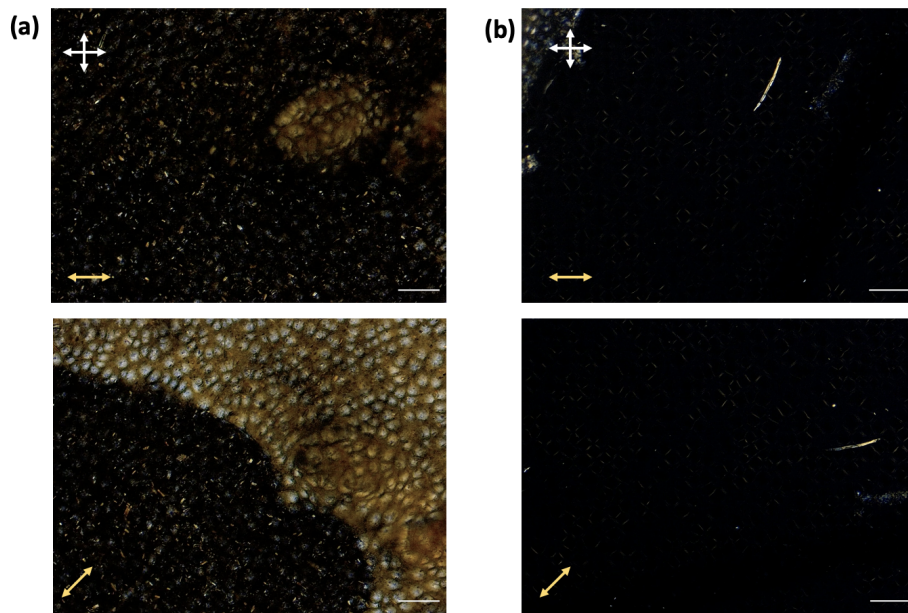


Figure 4.18: Polarized light optical images of CNC80 membranes with 5 mM AlCl<sub>3</sub> (a) and 25 mM CaCl<sub>2</sub> (b) concentration. Insets show POM. Double-sided yellow arrows indicate the direction of flow during deposition. Scale bars: 250  $\mu$ m for POM images.



Membranes could be obtained reproducibly using NaCl concentrations between 1 and 50 mM, since the suspensions were stable enough during deposition. A porous layer of cellulose acetate (Support II) was used for the deposition of salty CNC suspensions. Filtration of CNC-NaCl suspensions was performed at two extreme flow rates; 80 mLmin<sup>-1</sup>, where the highest degree of alignment of CNCs was observed, and 9 mLmin<sup>-1</sup>, where the CNCs were not preferentially aligned towards the direction of tangential flow in the absence of salt. During each filtration, a limiting flux was reached, indicating the presence of a CNC deposit on the support. The limiting flux decreased with increasing NaCl concentration at both feed flow rates and converged to almost the same values above 5 mM (4.19). The decreasing limiting flux implies a lower coagulation concentration of CNCs, also agreeing with their decreasing stability with increasing salt.

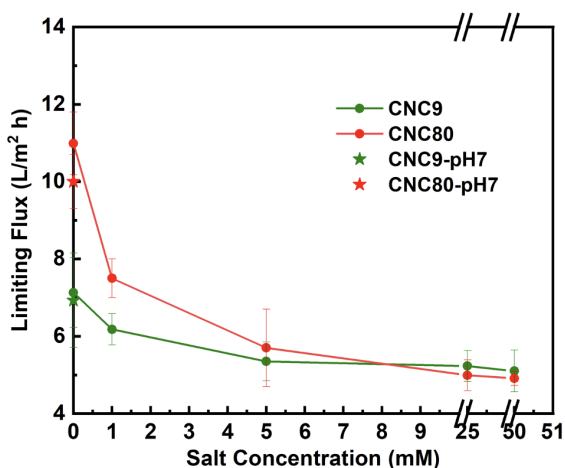


Figure 4.19: CNCs limiting fluxes with varying NaCl concentration in the CNC feed and feed pH

Pure water permeance values of high-sheared membranes decreased significantly from  $9.7 \pm 3.3$  up to  $4.9 \pm 0.4$  Lh<sup>-1</sup>m<sup>-2</sup>bar<sup>-1</sup>, and for low-sheared membranes from  $6.4 \pm 1.1$  to  $5.2 \pm 0.9$ , with the increase of the salt concentration from 0 to 50 mM as shown in 4.20a. The change in pH value from acidic to neutral of the feed suspension also resulted in a significant decrease of pure water permeances to  $3.4 \pm 0.04$  and  $5.7 \pm 1.3$  Lh<sup>-1</sup>m<sup>-2</sup>bar<sup>-1</sup> for low- and high-sheared membranes, respectively. Even though there is a significant decrease in pure water permeances with the addition of

salt or change in the suspension pH, these values are comparable with commercial ultrafiltration membranes with varying MWCO values (1-10 kDa), which are tabulated in Table 4.1.

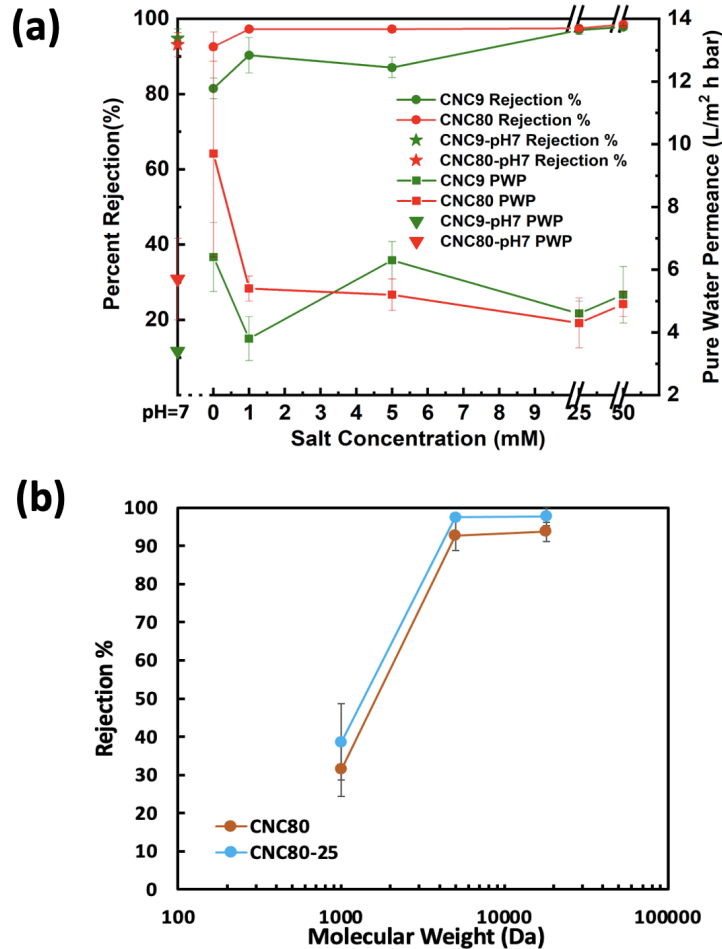


Figure 4.20: (a) CNC9 and CN80 membrane percent rejection values and pure water permeances with varying NaCl concentration in the CNC feed and at neutral pH (b) CNC80 and CNC80-25 percent rejection values against probe molecules of Vitamin B12 and  $\beta$ -lactoglobulin

Rejection of BD5 increased significantly with increasing NaCl concentration from 0 to 50 mM, from  $92.7 \pm 4\%$  to  $98.5 \pm 0.2\%$  for CNC80 membranes, and more substantially from  $82 \pm 3\%$  to  $98 \pm 0.3\%$  for CNC9 membranes, respectively. The increased rejection indicates a more compact CNC arrangement within the deposit due to the suppressed EDL thickness during deposition. At higher salinities (25 and 50 mM),

Table 4.1: Pure Water Permeances (PWP) of CNC Membranes and Commercial Ultrafiltration Membranes and with Varying Molecular Weight Cut-off (MWCO)

Membrane	MWCO (kDa)	PWP ( $\text{Lh}^{-1}\text{m}^{-2}\text{bar}$ )
Synder filtration UF (polyethersulfone)	1	3.7[81]
GE Osmonics GH (thin film)	1-2.5	3.33 [82]
Millipore PLB04310 (regenerated cellulose)	1-3	$6.98 \pm 0.7$ [82]
TriSep UA60, (polypiperazine-amid)	1-3.5	7.94[82]
GE Osmonics GK (thin film)	2-3.5	5.66[82]
Millipore Ultracel Disk (regenerated cellulose)	5	4.9[83]
Amfor PES5 (polyethersulfone)	5	22[43]
Alfa Raval RC70PP (regenerated cellulose acetate)	10	14.76[83]
Millipore Ultracel PLGC (regenerated cellulose)	10	25.9[43]
Millipore PLGC0431 (regenerated cellulose)	10	26.8[84]
Amfor PES10 (polyethersulfone)	10	89.5[43]
CNCX-Y and CNC-pH7 Membranes	BD5 Rejection(%)=87-98.5	3.8-5.7

the difference due to shear-alignment was compensated with further electrolyte addition, and rejections reached similar values for both CNC9 and CNC80 membranes which we judged to be a significant improvement. It is also noted that the membrane permeances of CNC9 and CNC80 membranes were similar at high salinities (Figure 4.20a). Membranes fabricated with a feed CNC suspension with 25 mM NaCl, at a flow rate of 80 mLmin<sup>-1</sup> (CNC80-25) were tested against Vitamin B12 (B12) and  $\beta$ -lactoglobulin (BL). Rejection performance of the CNC80 membrane was also enhanced with the addition of salt against both probe molecules; from 32% to 38% and from 94% to 98%, for B12 and BL probes, respectively (Figure 4.20b).

CNC deposit layers were formed using cellulose nanocrystal suspensions with neutral pH value by the same procedure, at two extreme feed flow rates (80 mLmin<sup>-1</sup> (CNC80-pH7) and 9 mLmin<sup>-1</sup> (CNC9-pH7)). Rejection against BD5 was measured as 94.6 $\pm$ 2.3% for CNC80-pH7 and 94 $\pm$ 3.3% for CNC9-pH7 membranes, which were higher compared to membranes fabricated under the same hydrodynamic conditions but with a feed suspension pH value of 3 (CNC80 and CNC9) (4.20a). This implies that the repulsive interactions between the nanocrystals were lowered, allowing tighter CNC deposits at neutral pH. The rejections obtained roughly indicate a Molecular Weight Cut-Off below 5 kDa for these membranes. Table 4.1 shows the pure water permeance of several commercial ultrafiltration membranes as reported in the literature, together with those of the membranes in this study, and illustrates that the permeances of CNC membranes are comparable to conventional ultrafiltration membranes of similar separation performance.

After filtration of CNCs, the deposit was stabilized on the support by a high concentration AlCl<sub>3</sub> solution treatment, which causes irreversible coagulation of CNCs on the support and finalizes the structure of the selective CNC layer without disrupting the CNC assembly. Resistance of the deposited CNC layers before and after AlCl<sub>3</sub> treatment, calculated by Darcy's law and resistances-in-series model, are shown in Figure 4.21. There is a consistent increase in the resistance after CNC deposition with increasing salt concentration and upon AlCl<sub>3</sub> treatment, the resistance further increases, showing that the deposit is further compressed. The same observation was also made with membranes fabricated using neutral CNC suspensions.

The specific resistance of the CNC layers after  $\text{AlCl}_3$  permeation through the CNC deposits, shown in Figure 4.21, were calculated by dividing the CNC layer resistance by the thickness of CNC layers observed in SEM images (Figure 4.22-4.24). It was observed that the specific resistance increases with NaCl addition until a certain concentration and then decreases with further salt. While the specific resistance can be considered as a measure of the compactness of the CNC deposit, which would be directly proportional to the rejections, these increased with added salt until a certain point and then remained constant. We believe the increased CNC deposit thickness at high concentrations causing the decreased specific resistance is related to CNC aggregates that form in bulk or the concentration polarization layer during tangential flow deposition, as shown in polarized optical microscopy images and more clearly explained in the coming section. The presence of aggregates, on the other hand, does not appear to decrease rejection, implying they are also composed of densely packed ordered CNC layers within, and the voids between aggregates do not span through the whole membrane cross-section.

Increasing pH to 7 also resulted in CNC layers of higher specific resistance (Figure 4.21c) while they had similar thickness (Figure 4.24) compared to those of CNC9 and CNC80 membranes which were shown in Figure 4.8. The higher specific resistances were directly reflected in the increased probe molecule rejections, implying more compact CNC deposits.

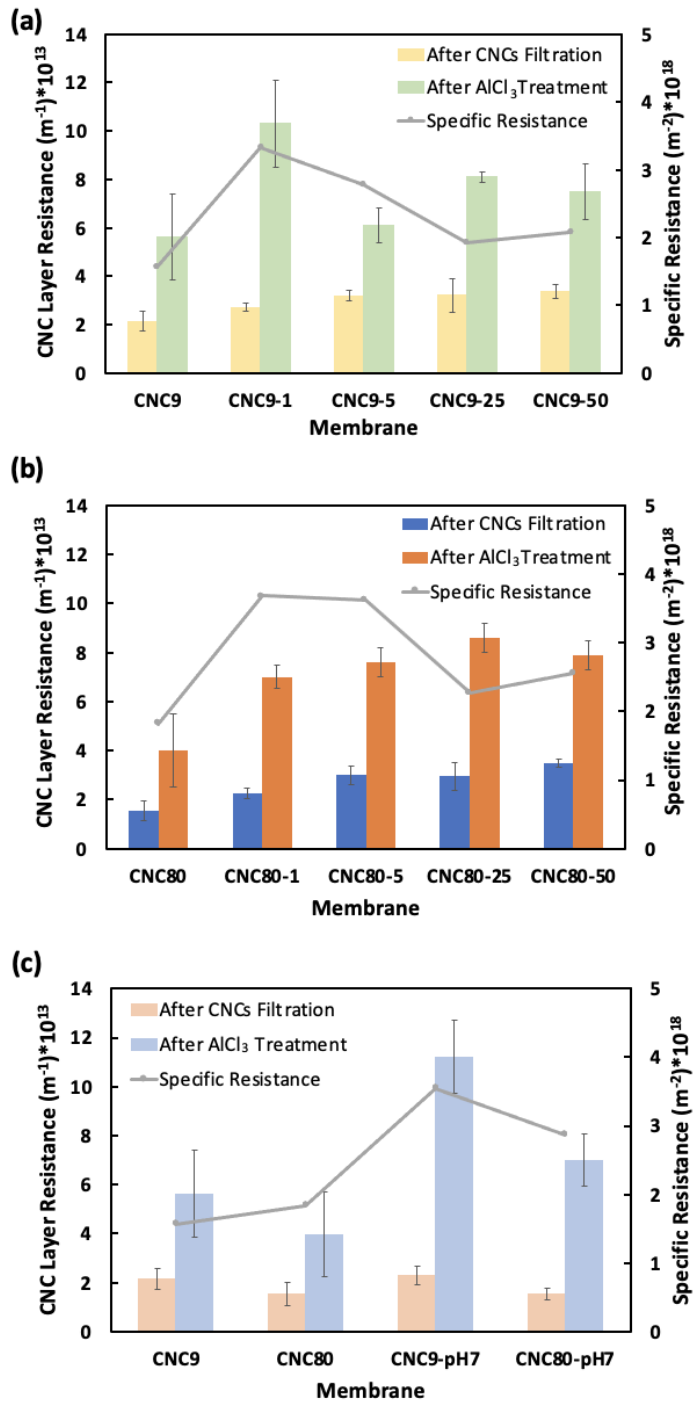


Figure 4.21: CNC deposit layer resistances before and after  $\text{AlCl}_3$  treatment and specific resistances of each membrane for membranes at varying NaCl concentrations (a and b) and different pH (c)

### 4.1.5.3 Structural Characteristics of CNC Deposit Layers

Optical characterizations were performed to understand the morphological changes of CNC deposit layers with the addition of salt or pH change of the suspension that result in changes in membrane performances. The extent and type of alignment, that is, the symmetry of the deposited layer, were analyzed by placing the CNC membranes in between crossed polarizers in the optical microscope. Figure 4.22 shows polarized optical microscopy images of CNC9 and CNC80 membranes prepared with the addition of NaCl.

CNC9-1 membrane showed a birefringent appearance under the optical microscope which can be interpreted as conservation of chiral-nematic assembly of CNCs. In other studies, using monovalent ions, improvement in the chirality of CNCs was observed at low concentrations of salts, and it was attributed to an increase in the aspect ratio of nanocrystals at low electrolyte concentration due to the slight compression of the EDL.[17] Based on Onsager's model, CNCs with larger aspect ratios enhance long-range order 50; thus, CNCs preserve cholesteric assembly at low shear rates and ionic strength. The significant increase in the deposit layer resistance after  $\text{AlCl}_3$  treatment for CNC9-1 membranes may also be associated with the improvement of the cholesteric ordering in the low sheared membrane, with the addition of the low amount of electrolyte to the feed suspension (Figure 4.21).

At high shear rates, the improvement of long-range order at low electrolyte concentrations may enhance the degree of shear alignment of CNCs. POM images of CNC80-1 membrane where the cholesteric assembly was disrupted with the applied high shear rate and gave bluish color at  $45^\circ$  to polarizers, which indicates a preferred alignment based on the Michel-Levy chart which illustrates the relationship between color and birefringence of a sample.[74] Shear-aligned structure of the CNC80-1 membrane can also be inferred from the SEM image in Figure 4.22 as revealed by the uniform horizontal roughness of the deposited layer. It is possible that in salty CNC suspensions, at concentrations lower than that of the deposited layer, nematic or cholesteric aggregates (or tactoids) form as a function of the local shear rate, CNC and salt concentration within the mass transfer boundary layer formed between the bulk and the membrane or CNC deposit surface.[17] The lower order appearance at deposition

formed with 5 mM NaCl concentration may be a result of the formation of the tactoids and their responses to shear in the presence of electrolytes.[65] As evidenced by the micrographs shown as insets of Figure 4.22, large tactoids appeared as large birefringence regions, which we reasoned to be broken with higher shear of the CNC80-5 conditions compared to CNC9-5 membranes.

At higher salinity, a uniform alignment of the CNC9-25 membranes was missing. On the other hand, for CNC80-25 membranes, strong birefringence was observed when the membrane was rotated in between crossed polarizers, indicative of a uniform alignment. These behaviors were also observed for higher salinity (50 mM) membranes fabricated at the same flow rates (CNC9-50 and CNC80-50, Figure 4.23). The reason behind the observation of uniform alignment for CNC80 membranes even with the high ionic strength may be that the higher shear rate ( $40\text{s}^{-1}$ ) is applied to CNCs during tangential flow, which promotes the breakup of collapsed CNC aggregates. Supporting this hypothesis, the micrographs of the deposit layers as insets revealed the presence of the large tactoids in CNC9-25 membranes. In contrast, their smaller counterparts were evident in CNC80-25, as indicated by the red arrows in the image insets. This observation supports that at high shear rates, the tactoids of CNCs were broken, and individual CNCs show nematic shear-aligned orientation in the shear direction (sketched in Figure 4.22c-d) as supported by rheology characterizations in the literature.[13] Consistently, for biphasic suspensions, the shear rate necessary to break tactoids was found to be more than  $10\text{s}^{-1}$  in past studies, consistent with our observations herein.[65]



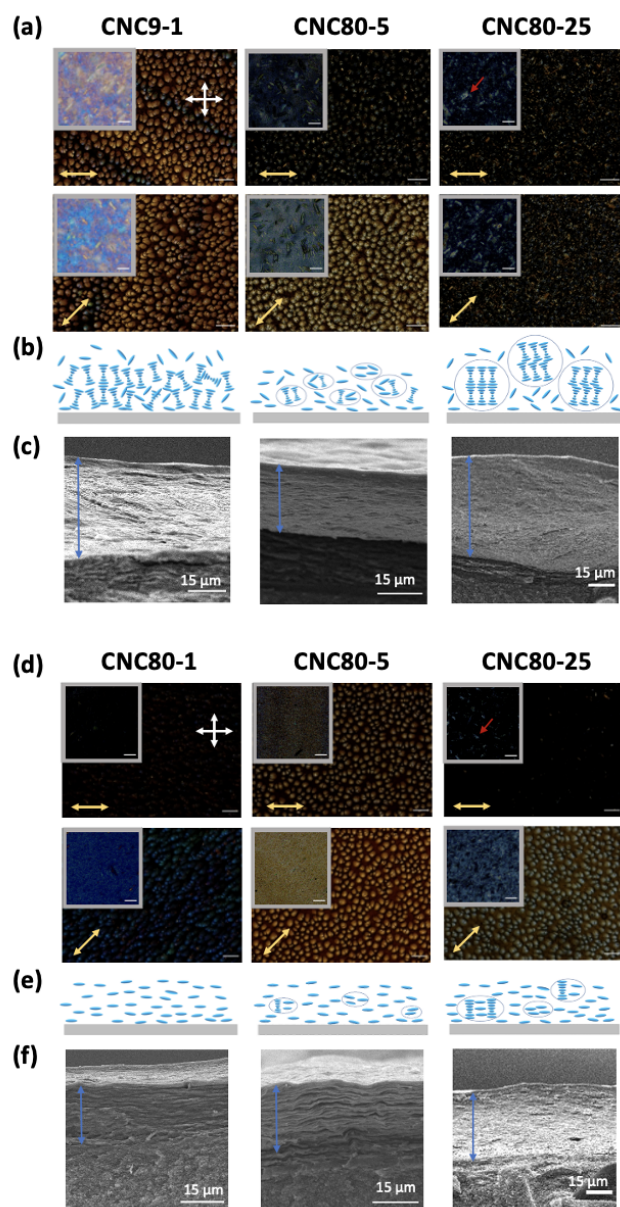


Figure 4.22: POM images of (a) CNC9 (d) CNC80 membranes with different NaCl concentrations at suspension pH value of 3. Insets show POM images of CNC deposits without a support layer obtained by dissolving the support in acetone. Red arrows in CNC9-25 and CNC80-25 show tactoids. Double-sided yellow arrows indicate the direction of flow during deposition. Illustrations below the polarized images represent CNC assembly in the corresponding CNC deposit layer (b,e). Scale bars:  $250 \mu\text{m}$  for POM,  $50 \mu\text{m}$  for inset images. The bottom panel shows the scanning electron micrographs of each membrane for the same column (c,f). Blue arrows indicate the cross-section of CNC deposit layers.

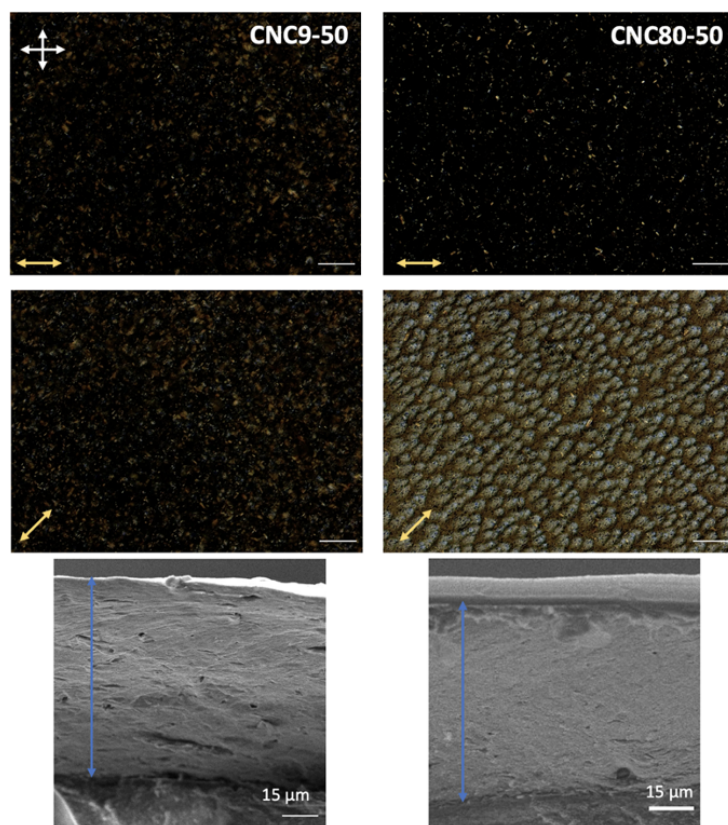


Figure 4.23: Polarized light optical images of CNC9-50 and CNC80-50 membranes. Double-sided yellow arrows indicate the direction of flow during deposition. Scale bars:  $250\ \mu\text{m}$  for POM images. The bottom panel shows the scanning electron images of each membrane for the same column. Blue arrows indicate the cross-section of CNC deposit layers.

The cross-sectional scanning electron microscopy images of CNC9-pH7 and CNC80-pH7 membranes are shown in Figure 4.24. The effect of suspension pH on the structure of resultant CNC layers was investigated by optical images. As shown in Figure 4.25a (left), polarized optical images of CNC80-pH7 revealed that there is a strong preferential alignment of CNCs to flow direction. The mean gray value profile of the membrane, which was placed in between cross-polarizers, being the same direction as the analyzer and tangential flow rate (analyzer  $0^\circ$ , polarizer  $90^\circ$ ) and rotated  $180^\circ$ , showed that the maximum bright color hue was observed at  $45^\circ$  multiples, while this value was minimum in the same direction with the analyzer and polarizer (Figure 4.25b). The higher degree of alignment of shear-aligned CNCs optical films fabri-

cated by neutral suspensions was observed in previous studies.[85] In our case, with the applied high shear ( $40s^{-1}$ ), CNCs form highly-ordered deposit layers.

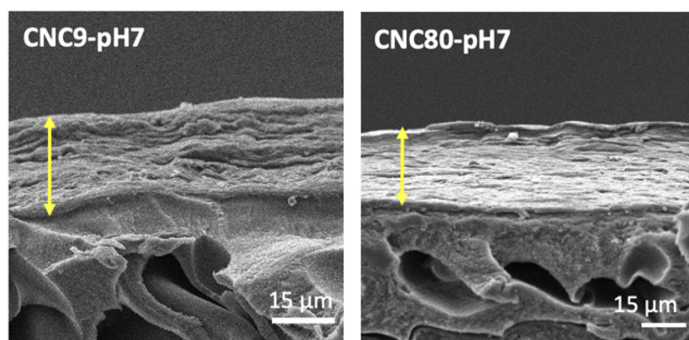


Figure 4.24: Scanning electron microscopy images of cross-section of CNC9-pH7 and CNC80-pH7 membranes. Double sided arrows indicate CNC layer deposit on support.

Surprisingly, at low shear rates, polarized light images and the mean gray value profile of CNC9-pH7 membranes revealed that CNCs aligned almost  $45^{\circ}$  to flow direction, giving the darkest color around  $50^{\circ}$  between the crossed polarizers (Figure 4.25a). For further investigation of the relative orientation of the CNC domains, a first-order-retardation plate was used with crossed polarizers. When the membrane was placed such that the flow direction during deposition was parallel to the polarizer, domains with red- and blue-hue were observed in the presence of retardation plate, which is evidence of alignment of CNCs at  $\pm 45^{\circ}$  to relative to flow direction. Rotating membrane  $90^{\circ}$  to the direction of flow rate resulted in a change of the colors from red to blue or blue to red appearing under a polarized optical microscope. Examples of such  $45^{\circ}$ -aligned regions in membranes with color changes after  $90^{\circ}$  rotation were indicated with dashed circles in Figure 4.25c. This interesting behavior of CNC9-pH7 membranes was further imaged by atomic force microscopy (Figure 4.25b), and the frequency of the angle of cellulose nanocrystals with respect to tangential flow direction was plotted. The reference plane was the direction of the flow, and two different orientation population was observed around  $50^{\circ}$  for CNCs in CNC9-pH7 membranes, which were also in agreement with optical polarized light images and image analyses.

Change in orientation patterns of shear-aligned CNC suspensions at different pH values was previously reported in the literature. It was shown that at high shear rates ( $>100\text{s}^{-1}$ ) applied on cellulose nanocrystals, the degree of alignment of CNCs was higher in neutral suspensions compared to that of acidic ones.[85, 86] However, the reason behind the orientation pattern of shear-aligned neutral CNCs remained unclear. One possible explanation of this behavior can be associated with kayaking-motion observed with non-spherical particles, at varying shear rates applied on particles.[86, 87]

It can be concluded that electrostatic interactions between cellulose nanocrystals can be tuned to control the membrane performances of cellulose nanocrystal membranes. The addition of inorganic salts to feed suspension or changing feed pH value affects the resultant membrane structure as well as its permeance and separation performance.

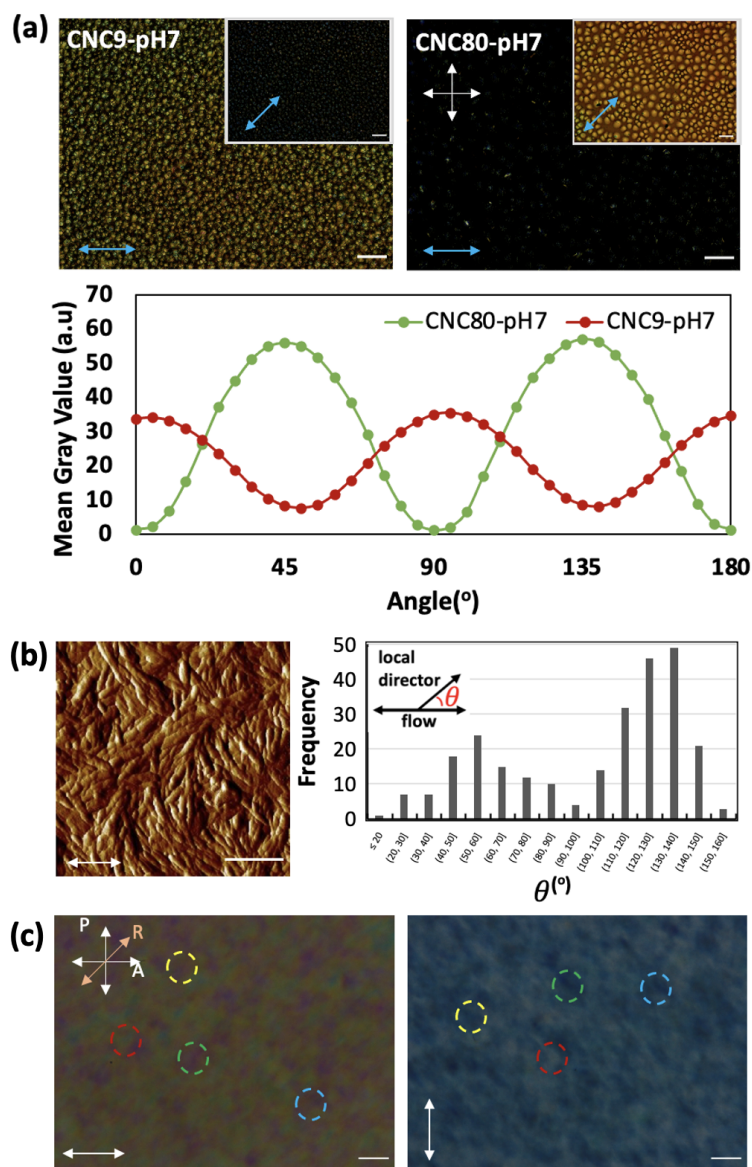


Figure 4.25: (a) Polarized light optical images of CNC9-pH7 and CNC80-pH7 membranes and mean gray value profile of these membranes with respect to angle of deposition direction relative to analyzer direction based on POM images. Double sided blue arrows in POM images represents the deposition direction. Crossed-white arrows represent the direction of analyzer and polarizer. Scale bars: 250  $\mu\text{m}$  for POM images (b) Atomic force microscopy image of top view of CNC9-pH7 membrane and angle frequency plot of the angles of nanocrystals based on AFM images. Angles represent the local direction relative to flow direction. Scale bar: 250 nm for AFM image (c) First-order-retardation plate images of CNC9-pH7 membranes at 0 and 90° of deposition direction relative to polarizer. Same colored circles show the same regions at two orientations. Additional orange double sided arrow represents the direction of retardation plate. Scale bars: 250  $\mu\text{m}$



## CHAPTER 5

### CONCLUSIONS

A new method of fabricating ultrafiltration membranes by deposition of shear-aligned CNCs from the aqueous suspension onto a porous support layer via tangential flow filtration of CNC suspensions through the support was demonstrated. During the membrane fabrication, tangential feed flow rate, feed suspension ionic strength, and pH of the feed were varied. Nanocrystals obtained from sulfuric acid hydrolysis of cotton linter used as the feed suspension were concentrated on the support surface due to the imbalance between permeate drag and back-diffusion, as is commonly observed in membrane fouling phenomena in the form of cake or gel deposition. With increasing shear rate, alignment of the nanocrystals in the flow direction was observed. At feed flow rates of 9, 30, and 80 mLmin<sup>-1</sup>, corresponding to 5, 15, and 40 s<sup>-1</sup> wall shear rates on the support surface, order parameters of 0.17, 0.48, and 0.7 were obtained in the CNC layers as seen in AFM. Increasing order parameters also resulted in increased probe molecule rejections. Addition of NaCl in the feed suspension used to form the CNC membranes decreased the electrostatic repulsion between the nanocrystals, thereby allowing them to pack tighter on the membrane. This increased probe molecule rejections and decreased the permeance of the membranes, although the pure water permeances were comparable to commercial membranes of similar MWCO. The same effect of ionic strength on membrane performance was observed both under high shear, where CNCs were observed to align in the shear direction (CNC80 series), as well as under low shear, where no shear alignment was observed without salt addition (CNC9 series). At high salinities, the difference between rejection values of low- and high-sheared membranes was compensated by strong electrostatic attractions between nanocrystals. Similarly, increasing the pH of the acidic CNC feed suspension to 7 yielded tighter membranes for low- and high-

sheared membranes. By manipulating the easy-to-adjust operation parameters, feed flow rate, and change in ionic strength and pH, the method provides comprehensive control of the structure of cellulose nanocrystals and hence the membranes' separation characteristics. The method enabled the manufacturing of ultrafiltration membranes with tunable rejection for macromolecules.



## REFERENCES

- [1] J. George and S. N. Sabapathi, "Cellulose Nanocrystals: Synthesis, Functional Properties, and Applications," *Nanotechnology, Science and Applications*, vol. 8, pp. 45–54, 2015.
- [2] Y. Habibi, L. A. Lucia, and O. J. Rojas, "Cellulose Nanocrystals: Chemistry, Self-Assembly, and Applications," *Chemical Reviews*, vol. 110, no. 6, pp. 3479–3500, 2010.
- [3] D. Trache, A. F. Tarchoun, M. Derradji, T. S. Hamidon, N. Masruchin, N. Brosse, and M. H. Hussin, "Nanocellulose: from fundamentals to advanced applications," *Frontiers in Chemistry*, vol. 8, p. 392, 2020.
- [4] E. Bukusoglu, M. Bedolla Pantoja, P. C. Mushenheim, X. Wang, and N. L. Abbott, "Design of Responsive and Active (Soft) Materials Using Liquid Crystals," *Annual Review of Chemical and Biomolecular Engineering*, vol. 7, no. 1, pp. 163–196, 2016.
- [5] J. P. Lagerwall, C. Schütz, M. Salajkova, J. Noh, J. H. Park, G. Scalia, and L. Bergström, "Cellulose Nanocrystal-Based Materials: From Liquid Crystal Self-Assembly and Glass Formation to Multifunctional Thin Films," *NPG Asia Materials*, vol. 6, no. 1, pp. 1–12, 2014.
- [6] L. Onsager, "The Effects of Shape on the Interaction of Colloidal Particles," *Annals of the New York Academy of Sciences*, vol. 51, no. 4, pp. 627–659, 1949.
- [7] M. J. Green, A. N. G. Parra-vasquez, N. Behabtu, M. Pasquali, M. J. Green, A. N. G. Parra-vasquez, and N. Behabtu, "Modeling the phase behavior of polydisperse rigid rods with attractive interactions with applications to single-walled carbon nanotubes in superacids Modeling the phase behavior of polydisperse rigid rods with attractive interactions with applications to single-walled carbon nanotubes in superacids," vol. 084901, 2009.

- [8] R. M. Parker, G. Guidetti, C. A. Williams, T. Zhao, A. Narkevicius, S. Vignolini, and B. Frka-Petesic, “The Self-Assembly of Cellulose Nanocrystals: Hierarchical Design of Visual Appearance,” *Advanced Materials*, vol. 30, no. 19, 2018.
- [9] S. Spirk and T. Nypel, “Cellulose Nanocrystal Liquid Crystal Phases: Progress and Challenges in Characterization Using Rheology Coupled to Optics, Scattering, and Spectroscopy,” *ACS Nano*, vol. 5, no. 5, pp. 7931–7945, 2021.
- [10] H. Oguzlu, C. Danumah, and Y. Boluk, “Colloidal Behavior of Aqueous Cellulose Nanocrystal Suspensions,” *Current Opinion in Colloid & Interface Science*, vol. 29, pp. 46–56, 2017.
- [11] C. Qiao, G. Chen, J. Zhang, and J. Yao, “Structure and Rheological Properties of Cellulose Nanocrystals Suspension,” *Food Hydrocolloids*, vol. 55, pp. 19–25, 2016.
- [12] Q. Wu, Y. Meng, S. Wang, Y. Li, S. Fu, L. Ma, and D. Harper, “Rheological behavior of cellulose nanocrystal suspension: Influence of concentration and aspect ratio,” *Journal of Applied Polymer Science*, vol. 131, no. 15, pp. 1–8, 2014.
- [13] M. Challamel, A. D. Geyer, M. Elchamaa, E. F. Semeraro, N. Hengl, B. Jean, J.-l. Putaux, E. Gicquel, J. Bras, S. Prevost, M. Sztucki, T. Narayanan, and H. Djeridi, “Breakdown and Buildup Mechanisms of Cellulose Nanocrystal Suspensions Under Shear and Upon Relaxation Probed by SAXS and SALS,” *Carbohydrate Polymers*, vol. 260, no. January, p. 117751, 2021.
- [14] F. Pignon, M. Challamel, A. De Geyer, M. Elchamaa, E. F. Semeraro, N. Hengl, B. Jean, J.-L. Putaux, E. Gicquel, J. Bras, *et al.*, “Breakdown and buildup mechanisms of cellulose nanocrystal suspensions under shear and upon relaxation probed by saxs and sals,” *Carbohydrate Polymers*, vol. 260, p. 117751, 2021.
- [15] J. M. Buffa, U. Casado, V. Mucci, and M. I. Aranguren, “Cellulose Nanocrystals in Aqueous Suspensions: Rheology of Lyotropic Chiral Liquid Crystals,” *Cellulose*, vol. 26, no. 4, pp. 2317–2332, 2019.
- [16] E. E. Ureña-Benavides, G. Ao, V. A. Davis, and C. L. Kitchens, “Rheology

- and phase behavior of lyotropic cellulose nanocrystal suspensions,” *Macromolecules*, vol. 44, no. 22, pp. 8990–8998, 2011.
- [17] S.-a. Jin, E. G. Facchine, S. A. Khan, O. J. Rojas, and R. J. Spontak, “Mesophase Characteristics of Cellulose Nanocrystal Films Prepared from Electrolyte Suspensions,” *Journal of Colloid And Interface Science*, vol. 599, pp. 207–218, 2021.
- [18] T. Phan-Xuan, A. Thuresson, M. Skepö, A. Labrador, R. Bordes, and A. Matic, “Aggregation Behavior of Aqueous Cellulose Nanocrystals: the Effect of Inorganic Salts,” *Cellulose*, vol. 23, no. 6, pp. 3653–3663, 2016.
- [19] J. Lyklema, “Coagulation by Multivalent Counterions and the Schulze – Hardy Rule,” *Journal of Colloid And Interface Science*, vol. 392, pp. 102–104, 2013.
- [20] R. W. Baker, *Membrane Technology and Applications*. John Wiley & Sons, 2012.
- [21] M. K. Selatile, S. S. Ray, V. Ojijo, and R. Sadiku, “Recent developments in polymeric electrospun nanofibrous membranes for seawater desalination,” *RSC advances*, vol. 8, no. 66, pp. 37915–37938, 2018.
- [22] I. Tsibranska and B. Tylkowski, “Concentration of ethanolic extracts from *Sideritis ssp. l.* by nanofiltration: Comparison of dead-end and cross-flow modes,” *Food and Bioproducts Processing*, vol. 91, no. 2, pp. 169–174, 2013.
- [23] V. Chen, A. G. Fane, S. Madaeni, and I. G. Wenten, “Particle deposition during membrane filtration of colloids: Transition between concentration polarization and cake formation,” *Journal of Membrane Science*, vol. 125, no. 1, pp. 109–122, 1997.
- [24] S. P. Nunes, P. Z. Culfaz-Emecen, G. Z. Ramon, T. Visser, G. H. Koops, W. Jin, and M. Ulbricht, “Thinking the Future of Membranes: Perspectives for Advanced and New Membrane Materials and Manufacturing Processes,” *Journal of Membrane Science*, vol. 598, p. 117761, 2020.
- [25] P. Van De Witte, P. Dijkstra, J. Van Den Berg, and J. Feijen, “Phase Separation Processes in Polymer Solutions in Relation to Membrane Formation,” *Journal of Membrane Science*, vol. 117, no. 1-2, 1996.

- [26] N. Peng, N. Widjojo, P. Sukitpaneenit, M. M. Teoh, G. G. Lipscomb, T.-S. Chung, and J.-Y. Lai, “Evolution of Polymeric Hollow Fibers as Sustainable Technologies: Past, Present, and Future,” 2012.
- [27] R. Hilke, N. Pradeep, A. R. Behzad, S. P. Nunes, and K.-V. Peinemann, “Block Copolymer/Homopolymer Dual-Layer Hollow Fiber Membranes,” 2014.
- [28] S. Rangou, K. Buhr, V. Filiz, J. I. Clodt, B. Lademann, J. Hahn, A. Jung, and V. Abetz, “Self-Organized Isoporous Membranes with Tailored Pore Sizes,” 2014.
- [29] H. Yu, X. Qiu, N. Moreno, Z. Ma, V. M. Calo, S. P. Nunes, and K.-V. Peinemann, “Self-Assembled Asymmetric Block Copolymer Membranes: Bridging the Gap from Ultra- to Nanofiltration,” 2015.
- [30] S. J. Louder and A. Asatekin, “Zwitterionic Ion-Selective Membranes with Tunable Subnanometer Pores and Excellent Fouling Resistance,” 2021.
- [31] S. J. Louder and A. Asatekin, “Interaction-Nased Ion Selectivity Exhibited by Self-Assembled, Cross-Linked Zwitterionic Copolymer Membranes,” 2021.
- [32] N. Joseph, P. Ahmadiannamini, R. Hoogenboom, and I. Vankelecom, “Layer-by-Layer Preparation of Polyelectrolyte Multilayer Membranes for Separation,” *Polymer Chemistry*, vol. 5, pp. 1817–1831, 2014.
- [33] R. M. Duchanois, R. Epsztein, J. A. Trivedi, and M. Elimelech, “Controlling Pore Structure of Polyelectrolyte Multilayer Nanofiltration Membranes by Tuning Polyelectrolyte-Salt Interactions,” *Journal of Membrane Science*, vol. 581, no. January, pp. 413–420, 2019.
- [34] D. M. Reurink, J. D. Willott, H. D. W. Roesink, and W. M. D. Vos, “Role of Polycation and Cross-Linking in Polyelectrolyte Multilayer Membranes,” *ACS Applied Polymer Materials*, vol. 2, no. 11, pp. 5278–5289, 2020.
- [35] Q. G. Zhang, C. Deng, F. Soyekwo, Q. L. Liu, and A. M. Zhu, “Sub-10 nm wide cellulose nanofibers for ultrathin nanoporous membranes with high organic permeation,” *Advanced Functional Materials*, vol. 26, no. 5, pp. 792–800, 2016.

- [36] S. Ling, K. Jin, D. L. Kaplan, and M. J. Buehler, “Ultrathin Free-Standing Bombyx mori Silk Nanofibril Membranes,” *Nano Letters*, vol. 16, no. 6, pp. 3795–3800, 2016.
- [37] P. Tyagi, A. Deratani, D. Bouyer, D. Cot, V. Gence, M. Barboiu, T. N. Phan, D. Bertin, D. Gigmes, and D. Quemener, “Dynamic Interactive Membranes with Pressure-Driven Tunable Porosity and Self-Healing Ability,” *Angewandte Chemie - International Edition*, vol. 51, no. 29, pp. 7166–7170, 2012.
- [38] P. Marchetti, M. Mechelhoff, and A. G. Livingston, “Tunable-Porosity Membranes from Discrete Nanoparticles,” *Scientific Reports*, vol. 5, pp. 1–14, 2015.
- [39] X. Peng, J. Jin, Y. Nakamura, T. Ohno, and I. Ichinose, “Ultrafast Permeation of Water Through Protein-based Membranes,” *Nature Nanotechnology*, vol. 4, no. 6, pp. 353–357, 2009.
- [40] R. K. Joshi, P. Carbone, F. C. Wang, V. G. Kravets, Y. Su, I. V. Grigorieva, H. A. Wu, A. K. Geim, and R. R. Nair, “Precise and Ultrafast Molecular Sieving Through Graphene Oxide Membranes,” *Science*, vol. 343, no. 6172, pp. 752–754, 2014.
- [41] L. Chen, G. Shi, J. Shen, B. Peng, B. Zhang, Y. Wang, F. Bian, J. Wang, D. Li, Z. Qian, G. Xu, G. Liu, J. Zeng, L. Zhang, Y. Yang, G. Zhou, M. Wu, W. Jin, J. Li, and H. Fang, “Ion Sieving in Graphene Oxide Membranes via Cationic Control of Interlayer Spacing,” 2017.
- [42] Q. Yang, Y. Su, C. Chi, C. Cherian, K. Huang, V. Kravets, F. Wang, J. Zhang, A. Pratt, A. Grigorenko, *et al.*, “Ultrathin graphene-based membrane with precise molecular sieving and ultrafast solvent permeation,” *Nature materials*, vol. 16, no. 12, pp. 1198–1202, 2017.
- [43] Z. Chen, J. Luo, Y. Wang, W. Cao, B. Qi, and Y. Wan, “A Novel Membrane-Based Integrated Process for Fractionation and Reclamation of Dairy Wastewater,” *Chemical Engineering Journal*, vol. 313, pp. 1061–1070, 2017.
- [44] The European Commission, “Commission Regulation (EU) 2018/588,” *Off. Journal Eur. Union*, pp. 99/3–99/6, 2018.

- [45] X. Dong, H. D. Shannon, C. Parker, S. De Jesus, and I. C. Escobar, "Comparison of two low-hazard organic solvents as individual and cosolvents for the fabrication of polysulfone membranes," *AIChE Journal*, vol. 66, no. 1, p. e16790, 2020.
- [46] H. H. Wang, J. T. Jung, J. F. Kim, S. Kim, E. Drioli, and Y. M. Lee, "A novel green solvent alternative for polymeric membrane preparation via nonsolvent-induced phase separation (nips)," *Journal of Membrane Science*, vol. 574, pp. 44–54, 2019.
- [47] K. Konca and P. Z. Çulfaz-Emecen, "Effect of Carboxylic Acid Crosslinking of Cellulose Membranes on Nanofiltration Performance in Ethanol and Dimethylsulfoxide," *Journal of Membrane Science*, vol. 587, no. June, p. 117175, 2019.
- [48] M. I. Baig, P. P. I. Sari, J. Li, J. D. Willott, and W. M. de Vos, "Sustainable aqueous phase separation membranes prepared through mild ph shift induced polyelectrolyte complexation of pss and pei," *Journal of Membrane Science*, vol. 625, p. 119114, 2021.
- [49] J. D. Willott, W. M. Nielen, and W. M. de Vos, "Stimuli-responsive membranes through sustainable aqueous phase separation," *ACS applied polymer materials*, vol. 2, no. 2, pp. 659–667, 2019.
- [50] E. N. Durmaz, M. I. Baig, J. D. Willott, and W. M. D. Vos, "Polyelectrolyte Complex Membranes via Salinity Change Induced Aqueous Phase Separation," 2020.
- [51] J. Kamp, S. Emonds, J. Borowec, M. A. R. Toro, and M. Wessling, "On the organic solvent free preparation of ultrafiltration and nanofiltration membranes using polyelectrolyte complexation in an all aqueous phase inversion process," *Journal of Membrane Science*, vol. 618, p. 118632, 2021.
- [52] M. I. Baig, E. N. Durmaz, J. D. Willott, and W. M. de Vos, "Sustainable membrane production through polyelectrolyte complexation induced aqueous phase separation," *Advanced functional materials*, vol. 30, no. 5, p. 1907344, 2020.
- [53] R. Prathapan, R. F. Tabor, G. Garnier, and J. Hu, "Recent Progress in Cellulose Nanocrystal Alignment and Its Applications," 2020.

- [54] Y. Habibi, T. Heim, and R. Douillard, "AC Electric Field-Assisted Assembly and Alignment of Cellulose Nanocrystals," *Journal of Polymer Science Part B: Polymer Physics*, 2008.
- [55] A. Barhoumi Meddeb, I. Chae, A. Han, S. H. Kim, and Z. Ounaies, "Magnetic Field Effects on Cellulose Nanocrystal Ordering in a Non-Aqueous Solvent," *Cellulose*, vol. 27, no. 14, pp. 7901–7910, 2020.
- [56] J. F. Revol, L. Godbout, X. M. Dong, D. G. Gray, H. Chanzy, and G. Maret, "Chiral Nematic Suspensions of Cellulose Crystallites; Phase Separation and Magnetic Field Orientation," *Liquid Crystals*, vol. 16, no. 1, pp. 127–134, 1994.
- [57] N. Yoshiharu, K. Shigenori, W. Masahisa, and O. Takeshi, "Cellulose Microcrystal Film of High Uniaxial Orientation," *Macromolecules*, vol. 30, no. 20, pp. 6395–6397, 1997.
- [58] I. Hoeger, O. J. Rojas, K. Efimenko, O. D. Velev, and S. S. Kelley, "Ultrathin Film Coatings of Aligned Cellulose Nanocrystals from a Convective-Shear Assembly System and Their Surface Mechanical Properties," *Soft Matter*, vol. 7, no. 5, pp. 1957–1967, 2011.
- [59] J. A. Diaz, X. Wu, A. Martini, J. P. Youngblood, and R. J. Moon, "Thermal Expansion of Self-Organized and Shear-Oriented Cellulose Nanocrystal Films," *Biomacromolecules*, vol. 14, no. 8, pp. 2900–2908, 2013.
- [60] A. D. Haywood and V. A. Davis, "Effects of Liquid Crystalline and Shear Alignment on the Optical Properties of Cellulose Nanocrystal Films," *Cellulose*, vol. 24, no. 2, pp. 705–716, 2017.
- [61] K. Kim, P. J. Kim, R. Ahmed, R. Kantharaj, A. Candadai, A. Marconnet, V. G. Pol, and J. P. Youngblood, "Structural Orientation Effect of Cellulose Nanocrystals ( CNC ) Films on Electrochemical Kinetics and Stability in Lithium-Ion Batteries," *Chemical Engineering Journal*, vol. 417, no. July 2020, p. 128128, 2021.
- [62] W. J. Orts, L. Godbout, R. H. Marchessault, and J. F. Revol, "Enhanced Ordering of Liquid Crystalline Suspensions of Cellulose Microfibrils: A Small Angle

- Neutron Scattering Study,” *Macromolecules*, vol. 31, no. 17, pp. 5717–5725, 1998.
- [63] R. A. Chowdhury, S. X. Peng, and J. Youngblood, “Improved order parameter (alignment) determination in cellulose nanocrystal (cnc) films by a simple optical birefringence method,” *Cellulose*, vol. 24, no. 5, pp. 1957–1970, 2017.
- [64] A. A. Moud, M. Arjmand, J. Liu, Y. Yang, A. Sanati-Nezhad, and S. H. Hejazi, “Cellulose nanocrystal structure in the presence of salts,” *Cellulose*, vol. 26, no. 18, pp. 9387–9401, 2019.
- [65] W. Y. Hamad and S. G. Hatzikiriakos, “Ionic strength effects on the microstructure and shear rheology of cellulose nanocrystal suspensions,” pp. 3347–3359, 2014.
- [66] P. Bertsch, S. Isabetini, and P. Fischer, “Ion-induced hydrogel formation and nematic ordering of nanocrystalline cellulose suspensions,” *Biomacromolecules*, vol. 18, no. 12, pp. 4060–4066, 2017.
- [67] Z. Wang, Y. Yuan, J. Hu, J. Yang, F. Feng, Y. Yu, P. Liu, Y. Men, and J. Zhang, “Origin of vacuum-assisted chiral self-assembly of cellulose nanocrystals,” *Carbohydrate Polymers*, vol. 245, p. 116459, 2020.
- [68] Q. Chen, P. Liu, C. Sheng, L. Zhou, Y. Duan, and J. Zhang, “Tunable self-assembly structure of graphene oxide/cellulose nanocrystal hybrid films fabricated by vacuum filtration technique,” *Rsc Advances*, vol. 4, no. 74, pp. 39301–39304, 2014.
- [69] E. Volkan, “Membrane fabrication using nanocrystalline cellulose,” Master’s thesis, Middle East Technical University, 2020.
- [70] A. Mautner, K. Y. Lee, T. Tammelin, A. P. Mathew, A. J. Nedoma, K. Li, and A. Bismarck, “Cellulose Nanopapers as Tight Aqueous Ultra-Filtration Membranes,” *Reactive and Functional Polymers*, vol. 86, pp. 209–214, 2015.
- [71] A. Mautner, K. Y. Lee, P. Lahtinen, M. Hakalahti, T. Tammelin, K. Li, and A. Bismarck, “Nanopapers for Organic Solvent Nanofiltration,” *Chemical Communications*, vol. 50, no. 43, pp. 5778–5781, 2014.



- [72] M. Bercea and P. Navard, “Shear Dynamics of Aqueous Suspensions of Cellulose Whiskers,” *Macromolecules*, vol. 33, no. 16, pp. 6011–6016, 2000.
- [73] S. Shafiei-Sabet, W. Y. Hamad, and S. G. Hatzikiriakos, “Rheology of Nanocrystalline Cellulose Aqueous Suspensions,” *Langmuir*, vol. 28, no. 49, pp. 17124–17133, 2012.
- [74] D. S. Miller, R. J. Carlton, P. C. Mushenheim, and N. L. Abbott, “Introduction to Optical Methods for Characterizing Liquid Crystals at Interfaces,” *Langmuir*, vol. 29, no. 10, pp. 3154–3169, 2013.
- [75] “COMSOL Multiphysics® v.5.2a..”
- [76] J. H. Park, J. Noh, C. Schütz, G. Salazar-Alvarez, G. Scalia, L. Bergström, and J. P. Lagerwall, “Macroscopic Control of Helix Orientation in Films Dried from Cholesteric Liquid-Crystalline Cellulose Nanocrystal Suspensions,” *ChemPhysChem*, vol. 15, no. 7, pp. 1477–1484, 2014.
- [77] J. De Gennes, P. G., Prost, *The Physics of Liquid Crystals (Vol.83)*. 1993.
- [78] Y. Boluk, L. Zhao, and V. Incani, “Dispersions of Nanocrystalline Cellulose in Aqueous Polymer Solutions : Structure Formation of Colloidal Rods,” *Langmuir*, vol. 28, no. 14, pp. 6114–6123, 2012.
- [79] H. Fukuzumi and R. Tanaka, “Dispersion Stability and Aggregation Behavior of TEMPO-Oxidized Cellulose Nanofibrils in Water as a Function of Salt Addition,” *Cellulose*, vol. 21, pp. 1553–1559, 2014.
- [80] J. Araki, “Electrostatic or Steric? – Preparations and Characterizations of Well-Dispersed Systems Containing Rod-like Nanowhiskers of Crystalline Polysaccharides,” *Soft Matter*, vol. 9, no. 16, pp. 4125–4141, 2013.
- [81] A. Aouni, C. Fersi, B. Cuartas-uribe, A. Bes-pía, M. I. Alcaina-miranda, and M. Dhahbi, “Reactive Dyes Rejection and Textile Effluent Treatment Study using Ultrafiltration and Nanofiltration Processes,” *Desalination*, vol. 297, no. 2012, pp. 87–96, 2020.
- [82] L. Xu, S. Shahid, J. Shen, E. Anna, C. Emanuelsson, and D. Alec, “A Wide Range and High Resolution One-filtration Molecular Weight Cut-off Method

- for Aqueous Based Nanofiltration and Ultrafiltration Membranes,” *Journal of Membrane Science*, vol. 525, no. November 2016, pp. 304–311, 2017.
- [83] V. Ippolitov, I. Anugwom, R. V. Deun, and M. Mänttari, “Cellulose Membranes in the Treatment of Spent Deep Eutectic Solvent Used in the Recovery of Lignin from Lignocellulosic Biomass,” *Membranes*, vol. 12, no. 1, p. 86, 2022.
- [84] C. Denis, A. Massé, J. Fleurence, and P. Jaouen, “Concentration and Pre-purification with Ultrafiltration of a R-phycoerythrin Solution Extracted from Macro-algae *Grateloupia turuturu* : Process Definition and Up-scaling,” *Separation and Purification Technology*, vol. 69, no. 1, pp. 37–42, 2009.
- [85] A. B. Reising, R. J. Moon, and J. P. Youngblood, “Effect of Particle Alignment on Mechanical Properties of Neat Cellulose Nanocrystal Films,” *Journal of Science & Technology for Forest Products and Processes*, vol. 2, no. 6, pp. 32–41, 2012.
- [86] M. Tatsumi and Y. Teramoto, “Different Orientation Patterns of Cellulose Nanocrystal Films Prepared from Aqueous Suspensions by Shearing Under Evaporation,” *Cellulose*, vol. 22, no. 5, pp. 2983–2992, 2015.
- [87] D. Z. Gunes, R. Scirocco, J. Mewis, and J. Vermant, “Flow-induced Orientation of Non-spherical Particles : Effect of Aspect Ratio and Medium Rheology,” *Journal of Non-Newtonian Fluid Mechanics*, vol. 155, pp. 39–50, 2008.

# Appendix A

## MICHEL-LEVY COLOR CHART

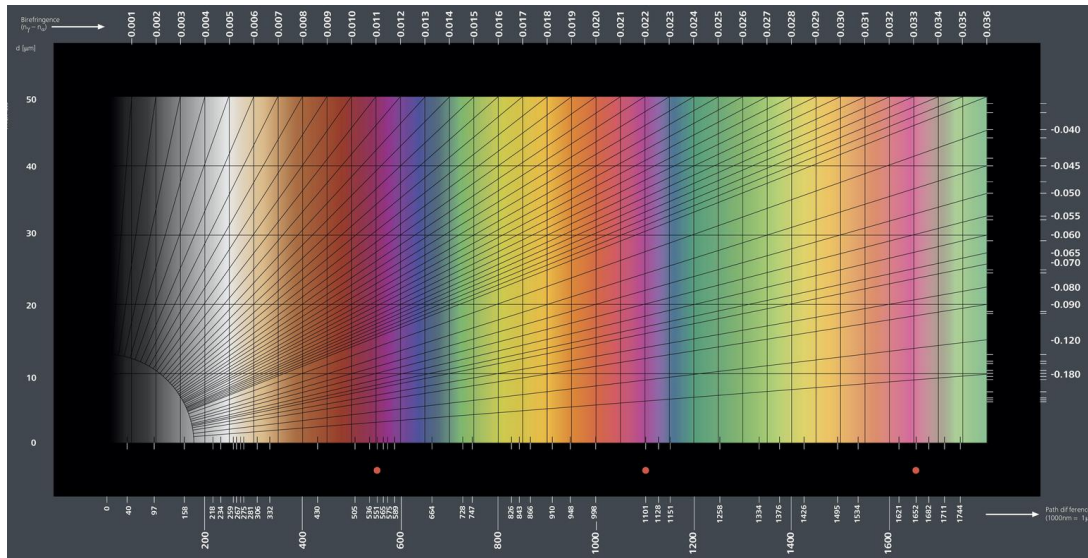


Figure A.1: Michel-Levy color chart



## Appendix B

### MEMBRANES AFTER FILTRATION TESTS AGAINST CHARGED MOLECULES

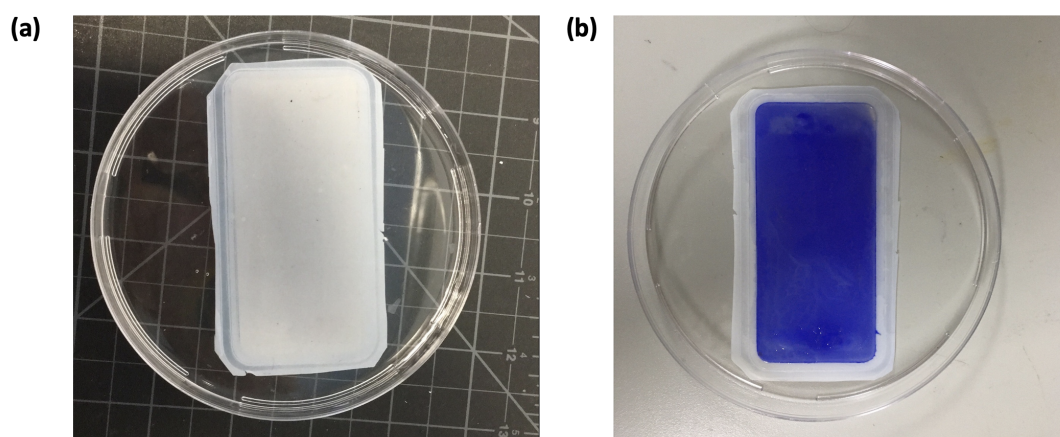


Figure B.1: Photographs of CNC80 membranes after rejection tests against (a) Rose Bengal (973 Da, negatively charged) (b) Crystal Violet (408 Da, positively charged)



## Appendix C

### ANALYTICAL MODELLING OF CAPILLARY FLOW OF CELLULOSE NANOCRYSTAL SUSPENSIONS

The representative sketch of capillary tube is shown in figure below. It was assumed that the flow is steady state, there is no gravity effect and flow is one dimensional.

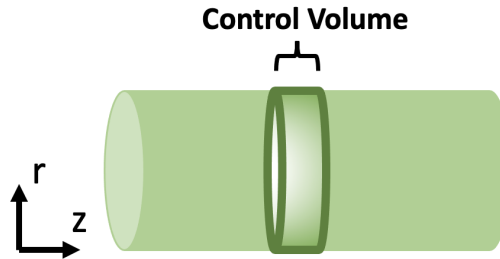


Figure C.1: Representation of control volume in a capillary tube

The force balance can be written around the control volume for a capillary tube with diameter  $D$ , as;

$$[P - (P + dP)] \frac{\pi D^2}{4} = \tau_w (\pi D dz) \quad (C.1)$$

$$\frac{dP}{dz} = \frac{4\tau_w}{D} \quad (C.2)$$

If the fluid element has the radius  $r$ , then the equation converts to ;

$$\frac{dP}{dz} = \frac{2\tau}{r} \quad (C.3)$$

For the power law fluids, the equation which relates the shear stress and shear rate as follow;

$$\tau_{rz} = k \left( \frac{dV_z}{dr} \right)^n \quad (C.4)$$

where k is the flow consistency index and n is the flow behavior index. Thus, the pressure drop over distance z can be written as;

$$\frac{dP}{dz} = \frac{2k}{r} \left( \frac{dV_z}{dr} \right)^n \quad (C.5)$$

Solving for velocity gives;

$$dV_z = \left( \frac{1}{2k} \frac{dP}{dz} \right)^{1/n} r^{1/n} dr \quad (C.6)$$

By integrating this function from 0 to R, where R is the radius of the capillary and  $V_z=0$  at the wall of the capillary ( $r=R$ );

$$V_z = \left( \frac{1}{2k} \frac{dP}{dz} \right)^{1/n} \left( \frac{n}{n+1} \right) R^{(1+1/n)} \left[ 1 - \left( \frac{r}{R} \right)^{n+1/n} \right] \quad (C.7)$$

The volumetric flow rate of CNC suspensions, Q, can be expressed by;

$$Q = V_z * \int A \quad (C.8)$$

where A is the cross-sectional area of the capillary tube.

$$Q = 2\pi \int V_z r dr = \left( \frac{1}{2k} \frac{dP}{dz} \right)^{1/n} \left( \frac{\pi n}{3n+1} \right) R^{3n+1} \quad (C.9)$$

The average velocity in the capillary tube  $V_{avg}$  is;

$$V_{avg} = \frac{Q}{A} = \left( \frac{1}{2k} \frac{dP}{dz} \right)^{1/n} \left( \frac{n}{3n+1} \right) * R^{1+(1/n)} \quad (C.10)$$

Thus, the velocity expression can be written as;

$$V_z = \frac{3n+1}{n+1} \left[ 1 - \left( \frac{r}{R} \right)^{(n+1)/n} \right] V_{avg} \quad (C.11)$$



Derivative of  $V_z$  function with respect to 'r' gives the shear rate expression as;

$$\frac{dV_z}{dr} = - \left( \frac{1}{R^{n+1/n}} \right) V_{\text{avg}} \left( \frac{3n+1}{n} \right) r^{1/n} \quad (\text{C.12})$$